# COMPARISON OF PLASTICS USED IN TISSUE EQUIVALENT PROPORTIONAL COUNTERS (TEPC) AND DEVELOPMENT OF A BALLOON BORNE TEPC

By

TYLER L. COLLUMS

Bachelor of Science in Physics
Pittsburg State University
Pittsburg, Kansas
2006

Master of Science in Physics
Pittsburg State University
Pittsburg, Kansas
2008

Submitted to the Faculty of the
Graduate College of the
Oklahoma State University
in partial fulfillment of
the requirements for
the Degree of
DOCTOR OF PHILOSOPHY
December, 2012

COMPARISON OF PLASTICS USED IN TISSUE

EQUIVALENT PROPORTIONAL COUNTERS (TEPC)

AND DEVELOPMENT OF A BALLOON BORNE TEPC

Dissertation Approved:

Eric R. Benton

Dissertation Adviser

Eduardo Yukihara

David Peakheart

Andy S. Arena

# ACKNOWLEDGEMENTS

There are many people I wish to thank for their assistance with this research project, but there are many more people I wish to thank for their guidance and influence throughout the course of my life that has led me to this point. God has continued to bless me by providing me with opportunity and surrounding me with people who have provided the instruction, guidance, or love that has allowed me to have any success in life. So it is to Him that I give all credit. May He be acknowledged in all the accomplishments of my life.

I would like to thank my advisor, Eric Benton, for his continued guidance throughout the course of this project and also for his dedication and passion for science which has caused my time in research here at OSU to be both challenging and fun. Special thanks is also given to Art Lucas whose experience and ingenuity proved invaluable to the success of this project. I would also like to thank the current and former members of the E. V. Benton Radiation Physics Laboratory: Carl Johnson, Joel Dewitt, Rafiq Islam, Nathan Lindy, Aaron Ruse, Jon Monson, and Robert Honeyman. Their assistance on this project as well their camaraderie during my time in this group was very important to me. I would especially like to thank Rafiq for the Monte Carlo simulation work which he did for this project.

I would like to thank Yuanshui Zheng at ProCure for providing us with very valuable beam time. I am also very appreciative of the help and beam time provided by the scientists at HIMAC: Yukio Uchihori, Nakahiro Yasuda, Hisashi Kitamura, and Satoshi Kodaira.

One cannot overestimate the influence that my parents played in the molding of a young boy into the man I am today. My father's expectations always pushed me to do my best, and his belief in me always convinced me that I could. By his own example he showed me that true success comes through hard work and honesty. My mother was a constant source of encouragement and love in my life. As a teacher she was the single largest influence on my early academic career. It was she who stayed up nights with me and forced me to finish my jr. high math homework when I was ready to give up, and it was she who proof read every paper I ever wrote in high school. There are not words to describe my appreciation and gratitude I have for my parents. To them I owe a debt which can never be repaid. Thank you Mom and Dad.

Finally, the person I wish to thank the most is my wife, Joni. She has been by my side every step of the way. Her love inspires me to be my best, and her honesty keeps me well grounded. She has invested just as much time and energy into the pursuit of my degree as I have. Every accomplishment of mine should be equally acknowledged as hers. I could not have accomplished what I have without her. Joni, I love you very much.

Name: Tyler L. Collums

Date of Degree: December, 2012

Title of Study: COMPARISON OF PLASTICS USED IN TISSUE EQUIVALENT PROPORTIONAL COUNTERS (TEPC) AND DEVELOPMENT OF A BALLOON BORNE TEPC

Major Field: Physics

This study investigates alternatives to A-150 tissue equivalent plastic for use in the construction of tissue equivalent gas-filled detectors for the measurement of dosimetric quantities. This study looks at four different alternative plastics: acrylic, Nylon, polyethylene, and polystyrene. These alternative materials are more readily available and easier to machine than A-150 tissue equivalent plastic. In this study they are compared to A-150 tissue equivalent plastic to determine how they compare in the measurement of lineal energy spectra from energetic protons and heavy ions as found in the space radiation environment, as well as at relevant clinical energies used in proton and heavy ion therapy. In experiments carried out at the ProCure proton therapy center in Oklahoma City, five proportional counters possessing ionization cavities constructed of five different materials (A-150 tissue equivalent plastic, acrylic, Nylon, polyethylene, and polystyrene) were used to measure the lineal energy spectra of energetic proton beams of 87 MeV, 162 MeV, and 222 MeV. Exposures to energetic heavy ions were carried out at HIMAC in Japan using beams of 143 MeV/amu He, 265 MeV/amu C, 440 MeV/amu Si, 430 MeV/amu Ar, and 421 MeV/amu Fe. Monte Carlo simulations using FLUKA were also done for each detector for each proton beam and each heavy ion beam. Comparison of the measured data obtained at ProCure and HIMAC, as well as simulation results using the Monte Carlo code FLUKA, indicate that the responses of the four alternative plastics tested are very similar to the response of A-150 tissue equivalent plastic. FLUKA simulations done for a detector made of ICRU muscle are also shown to have a response similar to that of all five plastics. A flight version of the TEPCs has also been developed for a high altitude flight on a balloon or other vehicle.

TABLE OF CONTENTS

Chapter Page

LIST OF TABLES

Table Page

LIST OF FIGURES

Figure Page

# CHAPTER I

# INTRODUCTION

The use of tissue equivalent plastic in dosimetric instrumentation such as ionization chambers and proportional counters has been common practice since Rossi, Failla, and Shonka began to develop muscle equivalent materials circa 1960. A-150 tissue equivalent plastic for use in x-ray beams and neutron fields was first introduced by Shonka in 1958 (Shonka et al., 1958). The elemental composition of A-150 was based on that of muscle from the 1956 Report of the International Committee on Radiation Units and Measurements. Theoretically, the accuracy of measured absorbed dose by such instruments depends on how closely the plastic used in the walls of the detector mimics the radiation response of actual tissue. Proportional counters have traditionally been used in microdosimetry to study the spatial and temporal distribution of absorbed energy in matter (Rossi and Zaider, 1996). While they started as microdosimeters, they are often times utilized more for their ability to measure macroscopic quantities such as absorbed dose and dose equivalent. Proportional counters are used today for charged particle and neutron dosimetry (Braby and Badhwar, 2001) in space (Shinn et al., 1998), as well as aboard aircraft (Kyllonen and Samuelson, 2001). They have also found applications in medical physics, particularly in cancer radiotherapy using protons (De Nardo, 2004) or

other heavy ions such as carbon. Like other gas-filled detectors, proportional counters operate by collecting and measuring the charge created by ionizing radiation that passes through the sensitive volume of the detector. The ionization of the gas can be caused by the primary radiation, by secondary electrons generated in the wall of the detector, or by charged particles produced in nuclear reactions (Rossi and Zaider, 1996). The quantity and energy of the secondary particles created in the wall of the detector is affected by values such as the stopping power, mass attenuation coefficient, and the neutron cross section of the material used in the ionization cavity wall. Proportional counters made of different materials may have different responses to ionizing radiation. This was the reasoning behind the development of tissue equivalent materials like A-150 plastic. A plastic having a similar atomic composition and density to living tissue will also possess a similar response to ionizing radiation. Thus, detectors made from such a tissue equivalent material will measure the absorbed dose and dose equivalent similar to that deposited in tissue. A-150, however, is not a commercially common material due to its specialized use. This inevitably makes bulk A-150 plastic difficult to find and expensive to purchase. An alternative is to make A-150 from scratch by mixing the constituents of the plastic (polyethylene, Nylon, carbon black, and calcium fluoride) (Smathers et al., 1977) together and then heating and melting the constituents in a mold of the desired shape. This approach is difficult and impractical due to the different melting points of nylon and polyethylene (Braby et al., 1995). Another problem with A-150 is that it is difficult to machine and does not possess the structural integrity of other more commonly available plastics due to the carbon black added to make the plastic conductive (Shonka et al., 1958).

This study looks at experimental and simulated data from five different proportional counters that each uses a different plastic for the ionization wall of the detector. The plastics used for this study are 1) A-150 tissue equivalent plastic, 2) polyethylene, 3) polystyrene, 4) nylon, and 5) acrylic (PMMA). Lineal energy spectra were measured using these detectors for energetic proton beams at three different energies and for five different heavy ion beams. The lineal energy spectra were also simulated for each detector using the FLUKA Monte Carlo radiation transport code (Fasso et al., 2003). The spectra for each detector from experiment and simulation are directly compared to investigate any differences in response due to the type of plastic used.

# CHAPTER II

## GAS-FILLED DETECTORS

Gas-filled detectors operate by collecting and measuring the charge created by ionizing radiation that passes through the sensitive volume of the detector. These detectors typically consist of two electrodes separated by some distance with the space between the electrodes filled with a gas. The two electrodes may have many forms and configurations including simple plate electrodes or spherical and thin wire electrodes. The detector may be vacuum sealed to allow for the use of a specific gas or it may be open to the atmosphere to simply use air as the gas between the electrodes. A large potential difference is applied to the electrodes using a high voltage power source to create an electric field in the region that the gas occupies. When ionizing radiation passes through this region of the gas it ionizes the gas and liberates electrons from the gas atoms. This results in free electrons and positive ions. Because these electron-ion pairs are charged they are affected by the electric field created by the electrodes. The electrons flow toward the higher voltage electrode and the positive ions toward the lower voltage one as shown in Figure 1.

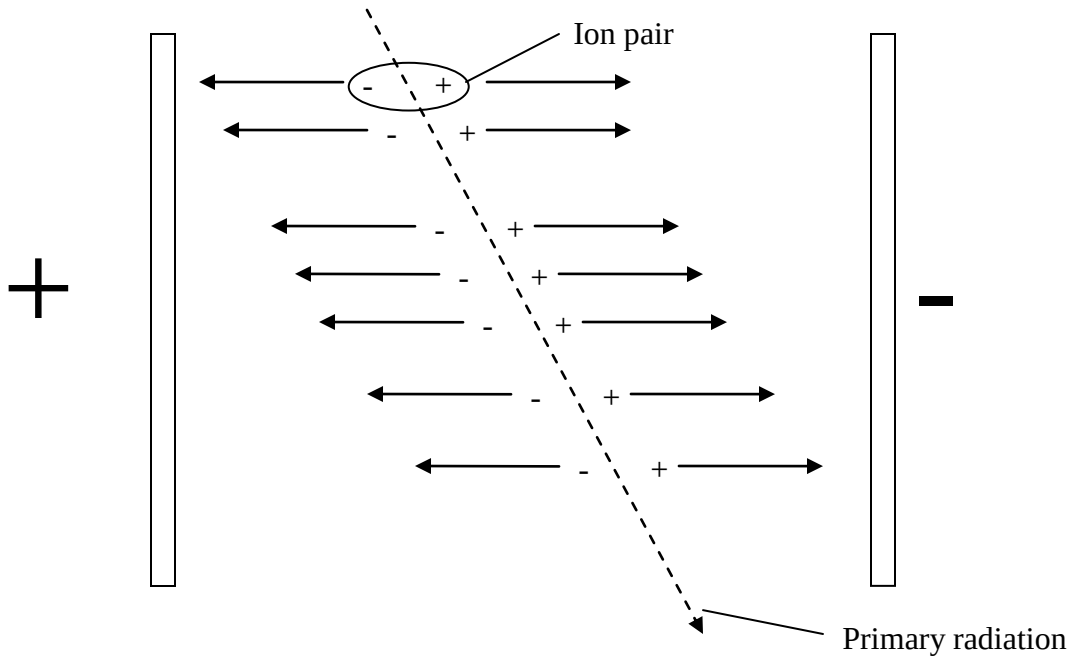


**Figure 1.** Ion pairs are created in the gas between the electrodes as ionizing radiation passes through the detector.

This movement of charge induces a current on the electrodes which may be directly measured or, by capacitively coupling to the electrode, the pulses from individual particles can be measured. The movement of the electrons and ions depends greatly on the size of the potential difference between the electrodes. The electron-ion pairs are accelerated by the force of the electric field, F = qE, where the charge is simply the charge of a single electron. The acceleration is then equal to this force divided by the mass of either the electron or the ion, a = qE/m. The acceleration is much larger for the electron due to its smaller mass. If the potential difference is not large enough between the electrodes then the electron-ion pairs may recombine and no charge will be collected. At larger voltages the ionized electrons may be accelerated enough to cause secondary

ionization in the gas. The production of more electrons in the gas creates an amplification of the original signal. Gas-filled detectors are classified, depending on the voltage they are operated at, into three categories: ionization chambers, proportional counters, and Geiger-Muller (GM) counters.

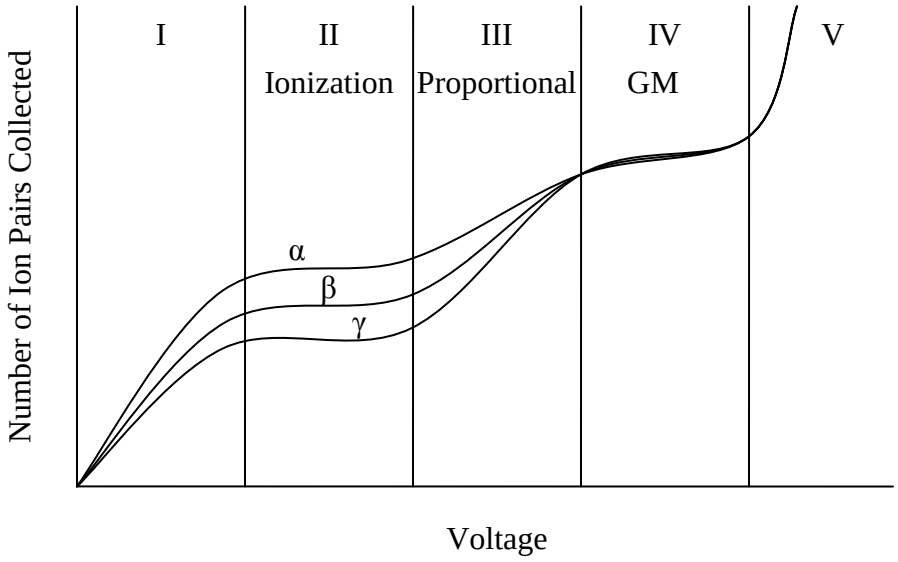


**Figure 2.** The voltage regions that a gas filled detector may fall into.

Figure 2 shows the number of ion pairs collected in a gas-filled detector for three different types of radiation as a function of the applied voltage. In region I of the graph, recombination occurs but decreases as the voltage is increased. The number of collected ion pairs goes up as recombination goes down. In region II the voltage is now high enough that recombination no longer occurs. The ion pairs are also not accelerated enough in this region to create secondary ionization so the number of collected ions stays constant as the voltage is increased. Region II is known as the ionization region and corresponds to the voltage range that ionization chambers are operated in. Secondary

ionization starts to occur in region III. The secondary ionization increases with voltage and increases the amount of collected ion pairs. This gas amplification is dependent on the voltage but is independent of the ionizing radiation. If two different types of primary ionizing radiation pass through the same detector in this region then the energy deposited by each will be multiplied by the same gas multiplication factor. The outputs from the detector for each of the primary particles will therefore remain proportional to one another. For this reason, region III is known as the proportional region and is the region that proportional counters operate in. To call region III the proportional region is somewhat misleading because the ionization region also exhibits this proportionality. The only difference between the ionization region and the proportional region is that gas multiplication takes place in the proportional region due to secondary ionization. The proportionality between the energy deposited in the detector and the output signal of the detector does not exist in region IV. In this region the output of the detector becomes independent of the primary radiation. At these voltages, a single ionization event is enough to initiate an avalanche of secondary ionizations. This chain reaction occurs regardless of the type of primary radiation or the energy that it deposited in the sensitive volume of the detector. In this region it is no longer possible to identify the primary radiation or determine the amount of energy deposited. This region is known as the Geiger-Muller region. In region V any single ionizing event will again cause a cascade of secondary ionizations, but in this region the cascade will be continuous. The detector will no longer be able to detect individual particles and the electrodes will continue to discharge through the gas until the voltage is lowered. No gas-filled detectors operate in this region.

# CHAPTER III

# MICRODOSIMETRY

## 3.0 Dosimetric Quantities

The purpose of any radiation detector is to quantify the amount of radiation in the measurement environment. The particle fluence, $\Phi$, is defined as the number of particles, *N*, that pass through a volume divided by the cross-sectional area, *A*, of the volume.

$$\Phi = \frac{N}{A} \qquad (1)$$

While particle fluence can be used to quantify a radiation field, it gives no information about the amount of energy being transferred to the medium in the field. Two different radiation fields with the same fluence may interact with the medium in drastically different ways. In many cases the most relevant information is not the fluence of the radiation field but how much energy is transferred to the medium particularly when that medium is human tissue. A more significant quantity to measure is that of absorbed dose. Absorbed dose, *D*, is defined as the energy, *E*, imparted to a volume of matter by ionizing radiation divided by the mass, *m*, of that volume of matter,

$$D = \frac{E}{m}. \qquad (2)$$

Ionizing charged particle radiation will deposit energy locally according to the Linear Energy Transfer (LET) of the particle in the medium. The LET, *L*, is defined as the amount of energy absorbed by the medium from a single particle per unit path length of the ionizing radiation,

$$L = \frac{dE}{dx}. \qquad (3)$$

The absorbed dose is related to the LET and the fluence through the relationship

$$D = \frac{\Phi L}{\rho}. \qquad (4)$$

A gas-filled detector cannot directly measure dose or LET. Instead it measures the current induced in the electrodes (ionization chamber) or it individually measures the voltage pulses created by electrons or ions hitting the anode (proportional counter). For an ionization chamber the measured current is proportional to the energy deposition rate in the chamber so that a calibration constant can be found to convert from current to dose. For a proportional counter the size of a pulse is proportional to the energy deposited by the particle that created the pulse. If the distance the particle traversed the gas region of the detector is known, then the pulse height may be converted to LET using a calibration constant. This would be true for a parallel plate proportional counter in which the ionizing radiation is unidirectional. For a spherical proportional counter in an isotropic field the chord length traversed by each particle is not known. In this case the pulse height created by a particle cannot be converted directly to LET because the size of the pulse also depends on the chord length traveled by the particle. For this reason proportional counter spectra are often expressed in terms of lineal energy instead of LET.

Lineal energy is defined as the amount of energy absorbed by the medium from a single particle divided by the average chord length of the medium,

$$y = \frac{E}{\bar{l}} \qquad (5)$$

where $\bar{l}$ is the average chord length of the gas-filled volume of the detector. For a spherical chamber the average chord length is

$$\bar{l} = \frac{2}{3} d \, . \qquad (6)$$

where $d$ is the diameter of the sphere. By using lineal energy instead of LET we can now state that the pulse height is proportional to the lineal energy of the particle whereas it is not proportional to LET.

### 3.1. Simulating Microscopic Volumes

One advantage of a proportional counter is the ability to simulate microscopic tissue volumes. This is accomplished by simulating a sphere of water with a diameter on the order of microns. By choosing the correct diameter and pressure of our tissue equivalent proportional counter we may construct a detector that receives the same amount of absorbed dose as a micron size sphere of water. In order to find the correct values for the diameter and pressure to be used in the detector we start with the condition that the dose to this sphere of water, $D_{water}$, should be the same as the dose to the sphere of gas inside the TEPC, $D_{gas}$, under an identical isotropic radiation field.

$$D_{gas} = D_{water} \qquad (7)$$

Energy is transmitted to the volume in two main ways. Primary particles can traverse the sphere, ionizing a path in the medium itself, or the primary particle can ionize material surrounding the volume which creates secondary electrons or neutrons which can penetrate into the volume and release energy. For a spherical tissue equivalent proportional counter, secondary electrons are created inside the plastic sphere surrounding the tissue equivalent gas. For a spherical volume inside a human, the secondary electrons are created in surrounding tissue. The energy can then be expressed in two terms so that the dose to the gas becomes

$$D_{gas} = \frac{N_{gas}\,\overline{E}_{primaries} + N_{\text{secondaries}}\,\overline{E}_{\text{secondaries}}}{m} \qquad \textbf{( 8)}$$

where $N_{gas}$ and $N_{secondaries}$ are the number of primary particles and secondary electrons, respectively, that traverse the volume. $\overline{E}_{primaries}$ and $\overline{E}_{\text{secondaries}}$ are the average amounts of energy deposited by each of these particles. The energy deposited by a single primary particle can be expressed as the product of the mass stopping power, $S_{mass}$, the density of the gas, $\rho_{gas}$, and the chord length traversed by the particle. For the average energy, the mean chord length, $\bar{l}$, through the sphere may be used,

$$\overline{E}_{primaries} = S_{mass}\,\rho_{gas}\,\bar{l}_{gas}. \qquad \textbf{( 9 )}$$

Plugging ( 9 ) into ( 8 ) gives

$$D_{gas} = \frac{N_{gas}\,S_{mass}\,\rho_{gas}\,\bar{l}_{gas} + N_{\text{secondaries}}\,\overline{E}_{\text{secondaries}}}{\rho_{gas}\,V_{gas}}. \qquad \textbf{( 10)}$$

The mass has been expressed in terms of the density and volume, $V_{gas}$. The mean chord length of a sphere is given as

$$\bar{l}_{gas} = \frac{2}{3} d_{gas} . \quad \textbf{( 11)}$$

The number of primaries entering the volume can be solved for using the equation for the flux, *F*, of the radiation field:

$$F = \frac{N_{gas}}{A_{gas}\, t} \quad \textbf{( 12)}$$

or

$$N_{gas} = F\, A_{gas}\, t \quad \textbf{( 13)}$$

where $A_{gas}$ is the cross sectional area of the sphere and *t* is the time of exposure. The number of secondaries generated in the surrounding material and entering the volume will be proportional to the surface area of the surrounding wall, 4 $A_{gas,}$ so that

$$N_{secondaries} \propto A_{gas} . \quad \textbf{( 14)}$$

Plugging ( 11), ( 13), and ( 14) into ( 10) gives

$$D_{gas} \propto \frac{F\, A_{gas}\, t\, S_{mass}\, \rho_{gas} \frac{2}{3} d_{gas} + A_{gas}\, \bar{E}_{secondaries}}{\rho_{gas}\, V_{gas}} \quad \textbf{( 15)}$$

where the equality has been changed to a proportionality. Separating the two terms and expressing the cross sectional area and volume of the gas in terms of the diameter of the sphere allows for simplification.

$$D_{gas} \propto \frac{F\,\pi\left(d_{gas}/2\right)^2\, t\, S_{mass}\, \rho_{gas}\, \frac{2}{3} d_{gas}}{\rho_{gas}\, \frac{4}{3}\pi\left(d_{gas}/2\right)^3} + \frac{\pi\left(d_{gas}/2\right)^2\, \overline{E}_{secondaries}}{\rho_{gas}\, \frac{4}{3}\pi\left(d_{gas}/2\right)^3} \qquad \textbf{( 16)}$$

Canceling terms in ( 16) gives

$$D_{gas} \propto F\, t\, S_{mass} + \frac{3}{2}\frac{\overline{E}_{secondaries}}{\rho_{gas}\, d_{gas}}, \qquad \textbf{( 17)}$$

or in terms of fluence, $\Phi = F\ t$ , the dose to the gas is expressed as

$$D_{gas} \propto \Phi\, S_{mass} + \frac{3}{2}\frac{\overline{E}_{secondaries}}{\rho_{gas}\, d_{gas}}. \qquad \textbf{( 18)}$$

The first term of this proportionality is exactly equal to the contribution from the primary particles and depends entirely on the radiation field fluence, $\Phi$ , and the stopping power of the beam. The size and density of the spherical volume has no effect on the first term. The same proportionality can be written for the dose to a microscopic volume of water.

$$D_{water} \propto \Phi\, S_{mass} + \frac{3}{2}\frac{\overline{E}_{secondaries}}{\rho_{water}\, d_{water}} \qquad \textbf{( 19)}$$

Assuming that the stopping power of the primaries is very similar in tissue or water to the stopping power in the tissue equivalent gas then the first terms of ( 18 ) and( 19 ) are identical. The second term is inversely proportional to the density and diameter of the sphere. Going back to the original condition of the absorbed dose being equal in both cases, ( 7),

$$D_{gas} = D_{water}, \tag{20}$$

we may now plug in ( 18 ) and ( 19 ) to get

$$F\,t\,S_{mass} + \frac{3}{2}\frac{\overline{E}_{secondaries}}{\rho_{gas}\,d_{gas}} = F\,t\,S_{mass} + \frac{3}{2}\frac{\overline{E}_{secondaries}}{\rho_{water}\,d_{water}}. \tag{21}$$

It is assumed that the proportionality constants in ( 18 ) and ( 19 ) were equal which allows ( 21 ) to be written as an equality. If we assume that the average energy deposited by the secondaries in both cases is the same then the equation simplifies to

$$\frac{1}{\rho_{gas}\,d_{gas}} = \frac{1}{\rho_{water}\,d_{water}} \tag{22}$$

or simply

$$\rho_{gas}\,d_{gas} = \rho_{water}\,d_{water}. \tag{23}$$

By using equation ( 23 ) we can simulate microscopic volumes by using larger volumes of gas at very low densities and pressures. For this study a tissue size of 10 μm was simulated. Given that the inner diameter of the detectors was 4.43 cm, then a gas density of $2.31 \times 10^{-4}$ g/cm$^3$ was needed to be used to simulate a 10 μm diameter sphere of tissue.

### 3.2. Pressure Calculation

To achieve the correct density in the detector, the corresponding pressure had to be found. We assume that the tissue equivalent gas acts as an ideal gas. The pressure is then given by the ideal gas law,

$$P = \frac{nRT}{V} \qquad \textbf{( 24 )}$$

where $P$ is the pressure, $n$ is the number of moles of gas, $R$ is the ideal gas constant, $T$ is the temperature, and $V$ is the volume. The density of the gas can simply be defined as the mass over the volume,

$$\rho = \frac{m}{V}. \qquad \textbf{( 25 )}$$

The mass of the gas can be expressed in terms of the number of moles of gas times the molar mass. The tissue equivalent methane-base gas used in this study was composed of three different gasses: nitrogen, carbon dioxide, and methane. The mass would then be the sum of the individual masses of each component. The density could then be expressed as

$$\rho = \frac{n_1 A_1 + n_2 A_2 + n_3 A_3}{V} \qquad \textbf{( 26 )}$$

Where $n_1$, $n_2$ and $n_3$ are the numbers of moles of each component and $A_1$, $A_2$, and $A_3$ are the molar masses of each component. Combing equations ( 24 ) and ( 26 ) by eliminating the volume gives

$$P = \frac{nRT\rho}{n_1 A_1 + n_2 A_2 + n_3 A_3} \qquad \textbf{( 27 )}$$

or

$$P = \frac{RT\rho}{\frac{n_1}{n} A_1 + \frac{n_2}{n} A_2 + \frac{n_3}{n} A_3}. \qquad \textbf{( 28 )}$$

The fractions in the denominator become the molar percentages or volume percentages for each component of the gas which are known. The volume percentages of the tissue equivalent gas were 29.99%, 2.751% and 67.26% for carbon dioxide, nitrogen, and methane, respectively. The molar masses for each are 44.01 g/mol, 14.01 g/mol, and 16.04 g/mol, respectively. Using these values, the required density from above, and a room temperature of 293.15 K, the needed pressure is calculated to be 173 Torr.

### 3.3. Calibration

The TEPCS have been calibrated using a removable ~1 μCi $^{241}$Am alpha particle source. The Americium is placed on the surface of the ionization chamber. A small hole of about 1mm in diameter in the ionization cavity wall allows alpha particles from the source to enter the sensitive volume of the gas and traverse the diameter of the sphere. The emitted alpha particles have an energy of 5.486 MeV which corresponds to an LET of 82.8 keV/μm in water. Due to a small metal collimator on the Americium source, as well as the small size of the hole in the sphere, most of the alpha particle trajectories will be along the full diameter of the sphere. This creates a sharp peak in the pulse height spectrum. This pulse height, or equivocally the channel number on the multichannel analyzer, can be used to calibrate the TEPC spectrum. A conversion factor, $x$, is needed to convert the pulse height spectrum into a lineal energy spectrum such that

$$y = x\,h \qquad \textbf{(29)}$$

where $h$ is the pulse height and $y$ is the lineal energy. The lineal energy is again defined as

$$y = \frac{E}{\bar{l}} \qquad \textbf{( 30 )}$$

where E is the energy deposited by a primary particle traversing a chord of the sphere and $\bar{l}$ is the mean chord length of the sphere. The energy deposited by a primary particle traversing the diameter is again given as

$$E = S_{mass}\, \rho_{gas}\, d_{gas}\,. \qquad \textbf{( 31)}$$

Due to the proportionality exhibited by a proportional counter, we may set the ratio of an unknown lineal energy, *y*, measured in the detector and the lineal energy of the calibrating source, $y_c$, to be equal to the ratio of the measured pulse height of the unknown lineal energy, *h*, and the pulse height obtained from the calibration source, $h_c$,

$$\frac{y}{y_c} = \frac{h}{h_c} \qquad \textbf{( 32)}$$

or

$$y = y_c \frac{h}{h_c}\,. \qquad \textbf{( 33)}$$

The pulse height from the calibration source, $h_c$, is obtained from the peak position of the spectrum taken with the TEPC. Plugging in ( 30 ) gives

$$y = \frac{E_c}{\bar{l}} \frac{h}{h_c} \qquad \textbf{( 34)}$$

The lineal energy of the calibration source can be determined by using stopping power tables to determine the amount of energy deposited, $E_c$ across the diameter of the sphere

Plugging in ( 31 ) into ( 34) and expressing the average chord length in terms of the diameter gives

$$y = \frac{3}{2}\frac{S_{mass}\rho_{water}d_{water}}{d_{water}}\frac{h}{h_c}. \quad \textbf{( 35 )}$$

Notice that the average chord length and the energy deposited in this case are for the simulated sphere of water. This is done because we want the detector calibrated in terms of energy deposition to tissue. Canceling the diameter from the numerator and denominator leads to

$$y = \frac{3}{2}\frac{S_{mass}\rho_{water}}{h_c}h. \quad \textbf{( 36)}$$

If the density of water is taken to be unity and the mass stopping power is given in MeV($cm^2$/g) then the equation may be further simplified to

$$y = \frac{3}{20}\frac{S_{mass}}{h_c}h \quad \textbf{( 37 )}$$

where *y* will be given in units of keV/μm. After calibration the $^{241}$Am is removed from the detector.

# CHAPTER IV

# SPECTRA

## 4.0 Chord Length Distribution

An LET spectrum may not be directly measured in a spherical proportional counter because the chord length traversed by each particle is unknown. In a parallel plate or cylindrical proportional counter an LET spectrum may be obtained if the counter is irradiated from a single direction so that the chord length is the same for each primary particle that enters the detector. For a spherical proportional counter it is theoretically possible to construct an LET spectrum from a lineal energy spectrum measured in an isotropic field if the chord length distribution is known. To determine the chord length distribution, consider a sphere of radius $r$ that is uniformly irradiated by an isotropic field. We can separate the isotropic field into many unidirectional fields as shown in Figure 3. Due to the symmetry of the sphere, the chord length distribution for each unidirectional field would be identical. Therefore, we only need to consider the simpler case of a sphere being irradiated by a single uniform unidirectional field.

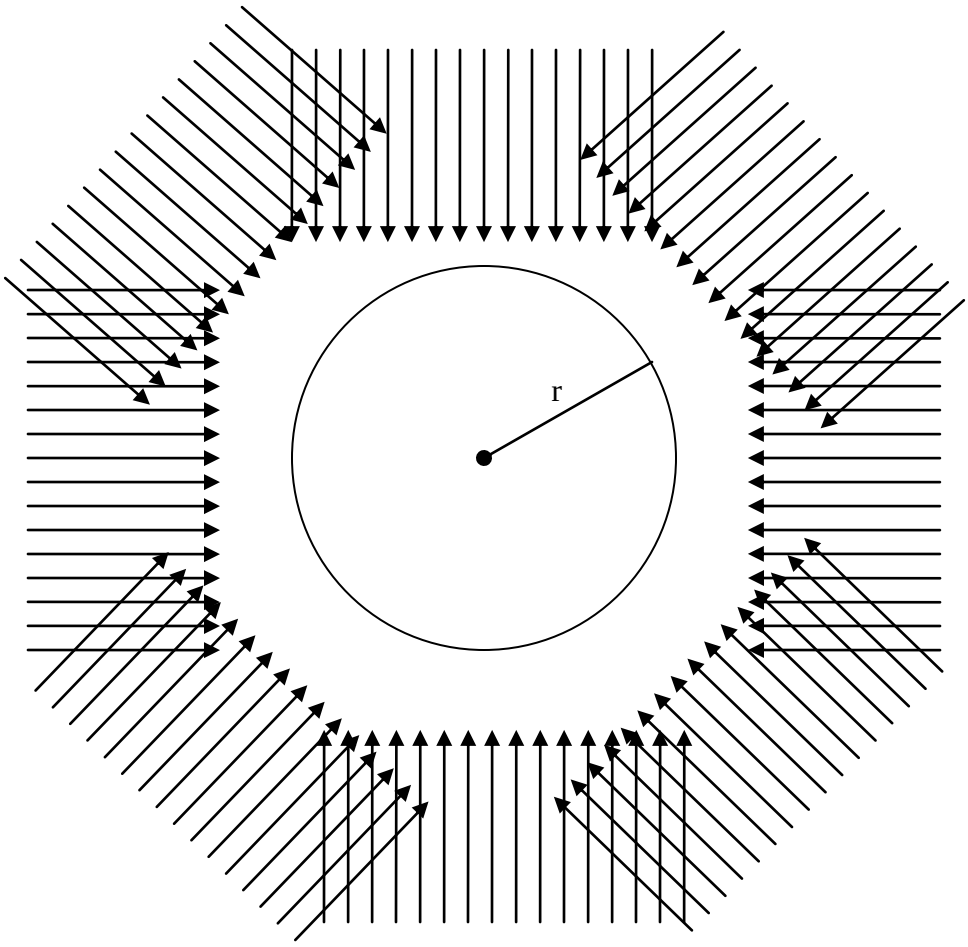


**Figure 3.** Approximating an isotropic field as many evenly space unidirectional field.

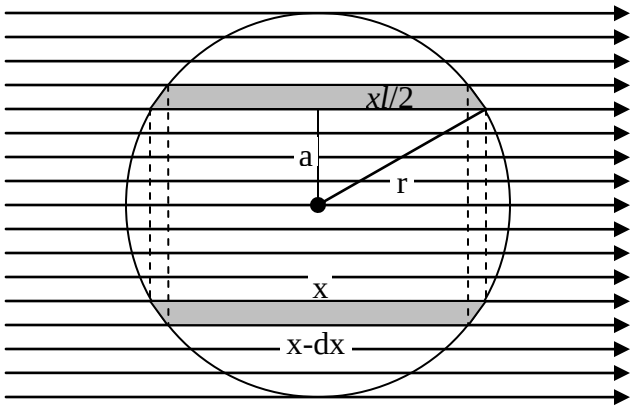


**Figure 4.** The chord length distribution for particles traversing a sphere due to an isotropic field may be derived from the case of a sphere in a single unidirectional field

The probability, *P(a)da*, that a particle will pass through the sphere with an impact parameter *a* will be equal to the number of particles passing through an annulus of radius *a*, shown in Figure 4, and width *da* divided by the number of particles that pass through the entire sphere,

$$P(a)\,da = \frac{2\pi a\,da\,\Phi}{\pi r^2\,\Phi}. \qquad \textbf{( 38 )}$$

The impact parameter is a function of the chord length and can be expressed as

$$a^2 = r^2 - \left(\frac{x}{2}\right)^2 \qquad \textbf{( 39 )}$$

where *x* is the chord length that the particle crosses. Differentiating ( 39 ) gives

$$da = -\frac{x\,dx}{4\sqrt{r^2 - \left(\frac{x}{2}\right)^2}}. \qquad \textbf{( 40 )}$$

Plugging in ( 39 ) and ( 40 ) into ( 38 ) gives the impact parameter distribution as

$$P(a)\,da = -\frac{2\sqrt{r^2 - \left(\frac{x}{2}\right)^2}\,x\,dx}{4r^2\sqrt{r^2 - \left(\frac{x}{2}\right)^2}} \qquad \textbf{( 41 )}$$

or

$$P(a)\,da = -\frac{x\,dx}{2r^2}. \qquad \textbf{( 42 )}$$

The probability that a particle passes between $a$ and $a + da$ is the same probability that the particle crosses with a chord length between $x$ and $x - dx$ or in other words

$$P(a)\,da = -P(x)\,dx. \qquad \textbf{( 43 )}$$

The chord length distribution then becomes

$$P(x) = \frac{x}{2r^2} \qquad \textbf{( 44 )}$$

or in terms of the diameter, $d$, of the sphere

$$P(x) = \frac{2x}{d^2}. \qquad \textbf{( 45 )}$$

This distribution is simply linear with respect to chord length. The most probable chord length for any one particle is therefore the full diameter of the sphere. Given this chord length distribution, the average chord length can be calculated as the expected value of *x*,

$$\bar{l} = \langle x \rangle = \int_0^d P(x)\, x\, dx . \qquad \textbf{( 46 )}$$

Differentiating yields the result that the average chord length is two thirds the length of diameter of the sphere,

$$\bar{l} = \int_0^d \frac{2x^2}{d^2} dx = \frac{2}{3} d . \qquad \textbf{( 47 )}$$

4.1. Lineal Energy Spectra

The energy deposited by these particles crossing the sphere is a function of the chord length. Expressing the energy deposited in terms of the chord length gives the following equation for lineal energy:

$$y = \frac{S_{mass}\, \rho_{gas}\, x}{\frac{2}{3} d} . \qquad \textbf{( 48 )}$$

From ( 48 ) we can see that the lineal energy distribution will also be the same as the chord length distribution since $S_{mass}$, $\rho_{gas}$, and $d$ are constants. In an ideal case the lineal energy distribution will therefore be a simple triangle when the sphere is irradiated isotropically with particles of the same LET, *L*, as shown in Figure 5.

.

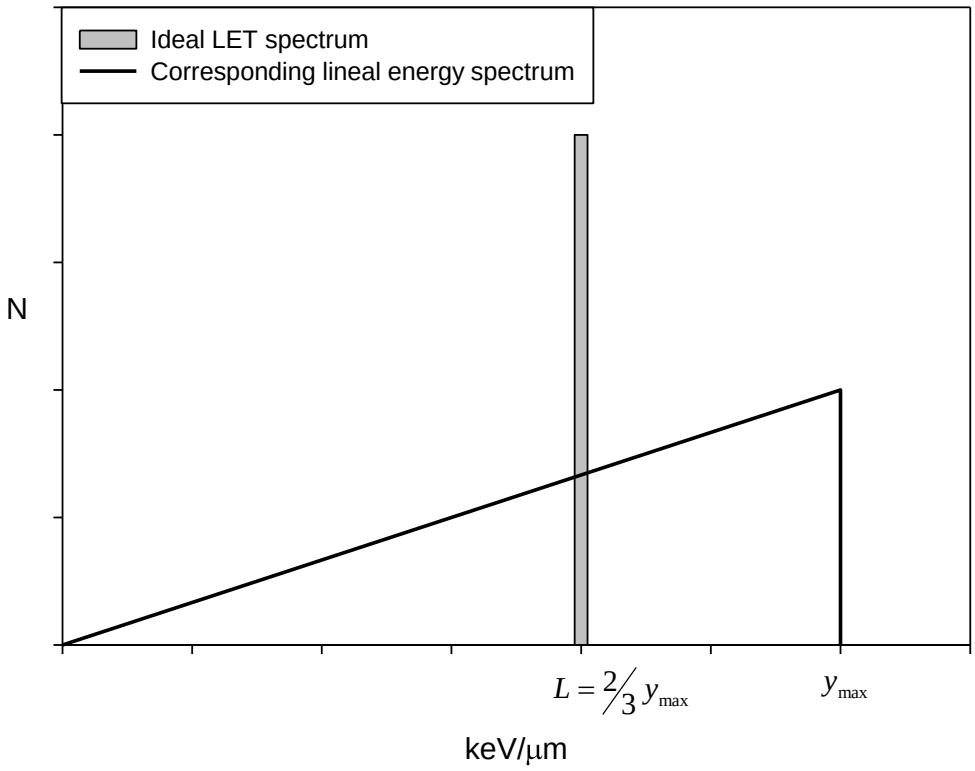


**Figure 5.** The ideal lineal energy spectrum that would be measured in a spherical proportional counter due to an isotropic field that has the LET spectrum shown.

The peak of the triangle at $y_{max}$ corresponds to particles that cross the full diameter of the sphere. $y_{max}$ will be equal to $\frac{3}{2} L$.

4.2. Plotting Lineal Energy Spectra

One difficulty in measuring lineal energy spectra is that, when the spectra are plotted normally on a linear scale, the plot is often not useful as a visual representation of the data. Figure 6 shows a typical lineal energy spectra measured for energetic protons by a

TEPC. The spectrum is a superposition of the primary proton peak and lower lineal energy events caused by secondaries created in the wall of the detector.

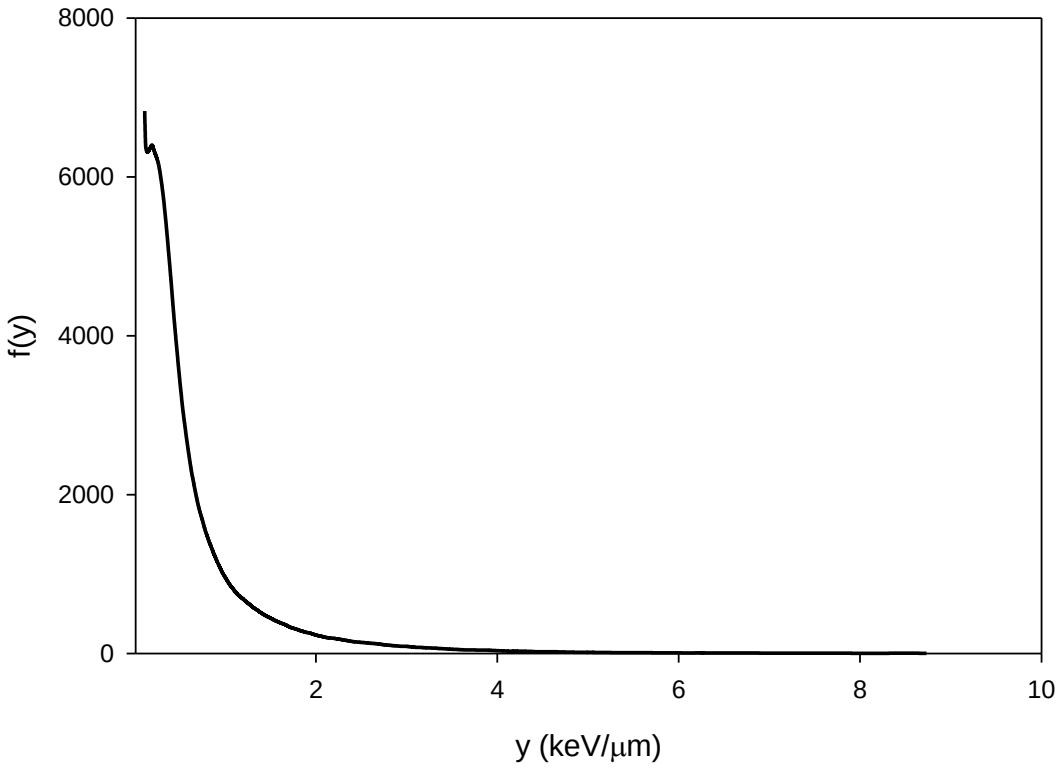


**Figure 6.** A lineal energy spectrum measured by the acrylic TEPC for 222 MeV protons. The ordinate is simply the frequency of particles or events and the abscissa is in a linear scale.

.

In this representation the proton peak can barely be seen. It is more useful if the abscissa were put into a log scale to give more resolution at lower lineal energies as shown in Figure 7. This is especially true for spectra taken of low LET particles or of spectra spanning a large range of lineal energies.

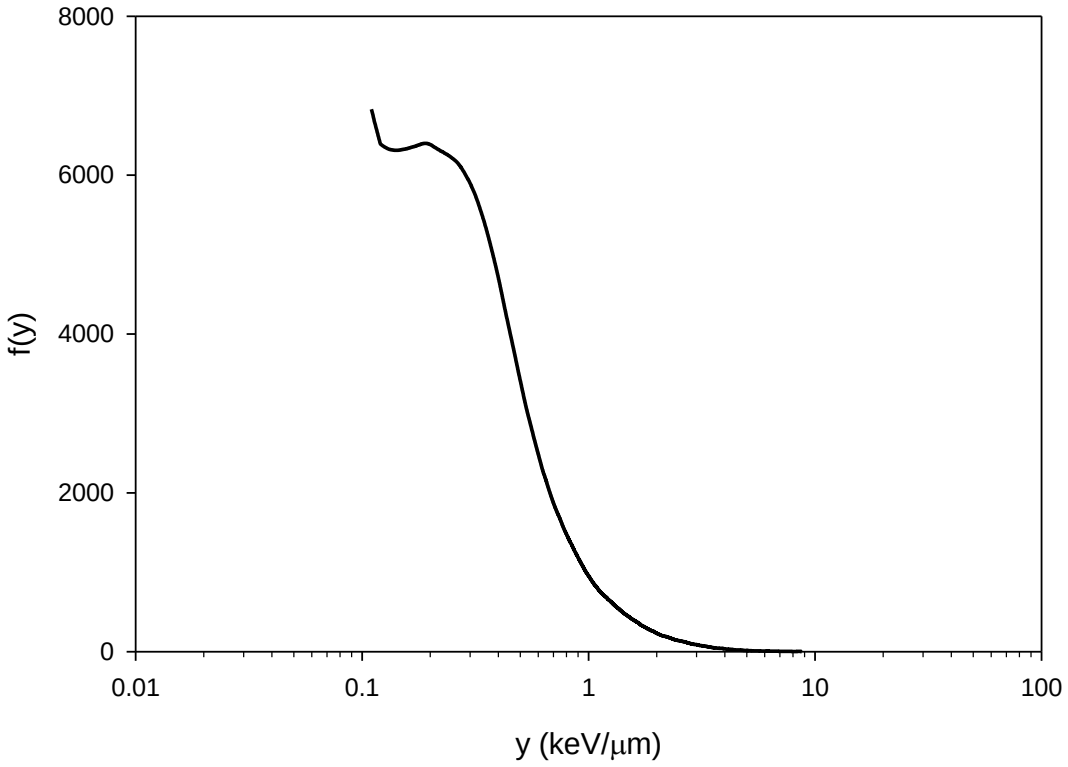


**Figure 7.** The same spectra shown in Figure 6 except that the abscissa is shown in a log scale to give more resolution at lower lineal energy.

By putting the abscissa on a log scale the spectrum has better resolution at lower lineal energies but has now become distorted. The area under the curve between any two lineal energies is no longer proportional to the amount of particles measured in that range. To preserve the proportionality the following fact may be used:

$$\int_{y_1}^{y_2} f(y)\,dy = \int_{y_1}^{y_2} y\, f(y)\,d\log(y). \qquad \textbf{(49)}$$

So by multiplying the frequency of particles with their lineal energy values and displaying the abscissa in a log scale we can create a plot where the area under the curve

is an accurate representation of the distribution of particles as shown in Figure 8. The peak in Figure 8 is now clearly distinguishable.

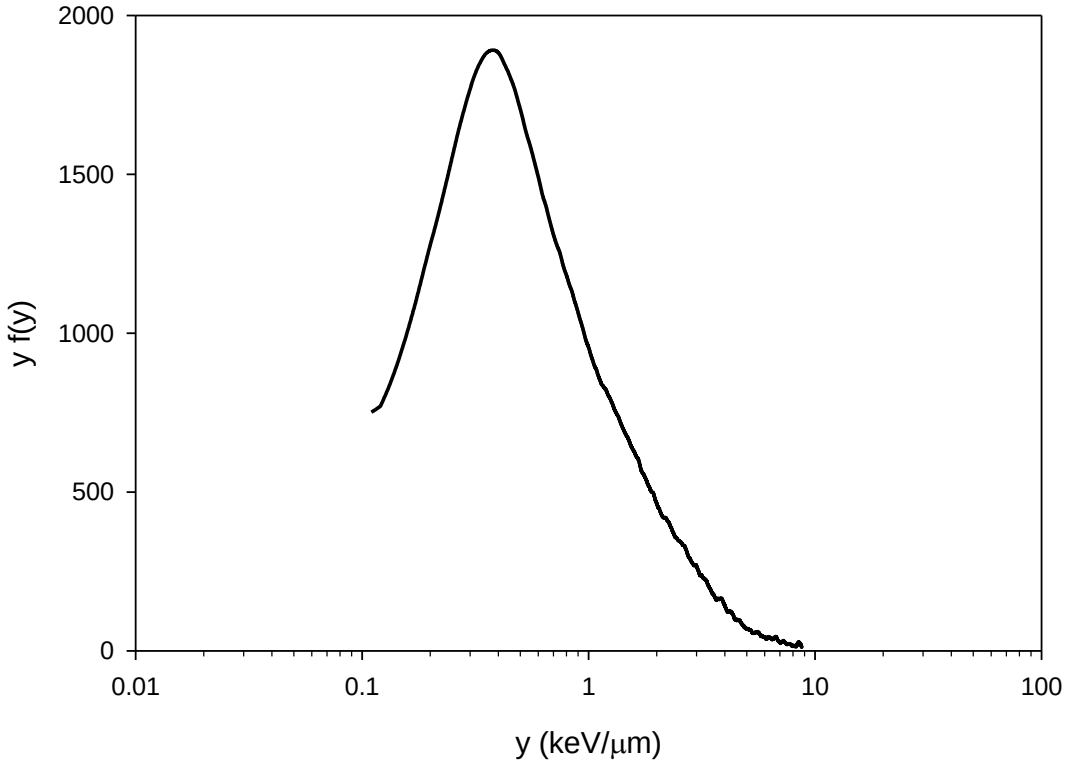


**Figure 8.** The same spectra shown in Figure 6 and Figure 7 except that the ordinate has been multiplied by *y*. This is the most common way of plotting a lineal energy spectrum when trying to display the frequency of events.

Often times one is more interested in the dose distribution rather than the frequency distribution of particles. Particles or events of higher lineal energy deposit more energy in the sensitive volume of the detector than low lineal energy events and therefore have more impact on the dose distribution. Using the same plotting technique shown above we may now multiply the ordinate by *y* again to give us a dose distribution since

$$D(y) = y\, f(y), \qquad \textbf{( 50 )}$$

as shown in Figure 9.

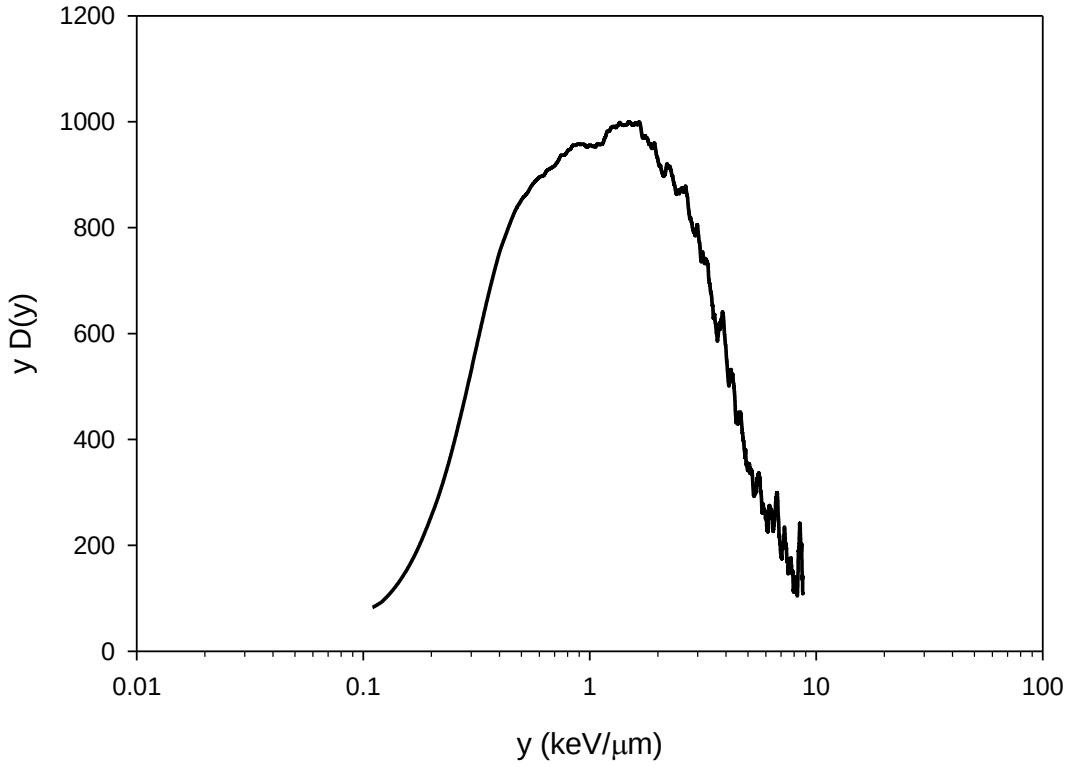


**Figure 9.** The dose distribution for the same data shown in the three previous figures. The ordinate has been multiplied by *y* again and the abscissa is shown in a log scale.

We can see from Figure 8 that the majority of the measured particles were found to have a lineal energy between 0.2 keV/μm and 0.8 keV/μm, but from Figure 9 we see that the majority of the dose was delivered by particles of higher lineal energy in a range from about 0.6 keV/μm all the way up to about 2 or 3 keV/μm.

4.3. Average Lineal Energy

It is often times useful to quantify a spectrum by calculating the average lineal energy of the spectrum. This can be done by taking the first and second moments of the frequency distribution referred to the frequency-averaged lineal energy and the dose-averaged lineal energy, respectively. The frequency-averaged lineal energy and the dose-averaged lineal energy are defined as

$$\bar{y}_f = \frac{\int_0^\infty y\, f(y) dy}{\int_0^\infty f(y) dy} \quad (51)$$

and

$$\bar{y}_D = \frac{\int_0^\infty y^2\, f(y) dy}{\int_0^\infty y\, f(y) dy}, \quad (52)$$

respectively (Rossi and Zaider, 1996). The frequency distribution is, by convention, usually defined to be normalized to one energy deposition event so that

$$\int_0^\infty f(y) dy = 1 \quad (53)$$

which reduces (51) and (52) to

$$\bar{y}_F = \int_0^\infty y\, f(y) dy \quad (54)$$

and

$$\bar{y}_D = \frac{1}{\bar{y}_F} \int_0^\infty y^2 \, f(y) dy , \qquad (55)$$

respectively. For an ideal spectrum of a uniform field passing through a sphere of gas, the frequency-averaged lineal energy is exactly equal to the LET of the monoenergetic charged particle beam being measured. This can be shown from the frequency averaged lineal energy definition and the ideal triangular frequency distribution derived in the previous sections. By plugging in a frequency distribution of a straight line,

$$\boldsymbol{f(y) = C\, y} , \qquad (56)$$

where *C* is simply the slope of the line, into ( 51 ) we get

$$\boldsymbol{\bar{y}_f = \frac{\int_0^{y_{max}} C\, y^2 \, dy}{\int_0^{y_{max}} C\, y \, dy}} \qquad (57)$$

for the frequency-averaged lineal energy of an ideal spectrum. Integrating the numerator and the denominator leads to

$$\boldsymbol{\bar{y}_f = \frac{2}{3} y_{max}} , \qquad (58)$$

but $y_{max}$ is equal to $^3/_2\, L$ so that

$$\boldsymbol{\bar{y}_f = L} . \qquad (59)$$

The dose-averaged lineal energy of the line distribution is similarly related to the LET of the ionizing charged particle radiation. Plugging in the same distribution into ( 52 ) gives

$$\bar{y}_D = \frac{\int_0^{y_{max}} C\, y^3\, dy}{\int_0^{y_{max}} C\, y^2\, dy}. \quad (60)$$

Solving the integrals gives

$$\bar{y}_D = \frac{3}{4} y_{max}, \quad (61)$$

or in terms of LET,

$$\bar{y}_D = \frac{9}{8} L \quad (62)$$

for an ideal spectrum of a sphere of gas in a uniform field. In a realistic spectrum, the frequency-averaged lineal energy is affected by any energy spread in the beam, as well as by secondary electrons created in the ionization cavity wall (Borak et al., 2004). Lower energy particles in the beam, having higher LET, increase the frequency-averaged lineal energy.

The frequency-averaged lineal energy is a good metric for comparing the ionization cavity wall materials because it is directly proportional to the dose measured in the detector. This can be shown by considering the equation for the frequency averaged lineal energy. From equation ( 51 ) we see that the frequency averaged lineal energy is

equal to the summation of the products of each measured lineal energy and the frequency of those events and then divided by the total number of events or counts. The lineal energy of each event is simply the energy deposited by each event, *E*, divided by the average chord length of the sphere, $\bar{l}$, which is a constant. The frequency averaged lineal energy may then be expressed as

$$\bar{y}_f = \frac{\int_0^\infty E/\bar{l}\, f(E)dE}{\int_0^\infty f(y)dy}. \quad (63)$$

If we also insert the mass, *m*, of the gas we may express the equation in terms of dose:

$$\bar{y}_f = \frac{m}{\bar{l}} \frac{\int_0^\infty E/m\, f(E)dE}{\int_0^\infty f(y)dy}. \quad (64)$$

The energy deposited divided by the mass is simply the deposited dose so that the summation in the numerator would become the total dose. The summation in the denominator is equal to the total number of measured counts, *N*. Equation ( 64 ) then becomes

$$\bar{y}_F = \frac{m}{\bar{l}} \frac{D_{total}}{N} \quad (65)$$

where $D_{total}$ is the total absorbed dose. We see then that the frequency averaged lineal energy is proportional to the absorbed dose over the total number of counts. The differences between the frequency averaged lineal energies between the different detectors will then give a measure of the differences in measured absorbed dose for an identical radiation field when the same number of events are measured.

4.4. Converting to LET

It is possible to convert the triangular lineal energy spectrum, $N_{y,}$ measured by a TEPC into an LET spectrum, $N_L$, as shown in Figure 5. For the ideal case where only a single LET radiation field is used, the LET spectrum will have only a single value at $L$. So by finding the total number of particles measured, the LET spectrum can easily be found. The lineal energy spectrum $N_y$ is the distribution of the number of particles per unit lineal energy, so by integrating over all possible lineal energies the total number of particles is obtained.

$$N_{total} = \int_0^{y_{\max}} N_y(y)\,dy = N_L(L) \qquad \textbf{( 66 )}$$

However, since the distribution of $N_y$ is just a line, the integral is equal to the area of the triangle.

$$\int_0^{y_{\max}} N_y(y)\,dy = \frac{1}{2}\, y_{\max}\ N_y(y_{\max}) = N_L(L) \qquad \textbf{( 67 )}$$

Now let us consider a more realistic case where the radiation field is made up of particles with multiple LETs. The lineal energy spectrum becomes a superposition of many triangles.

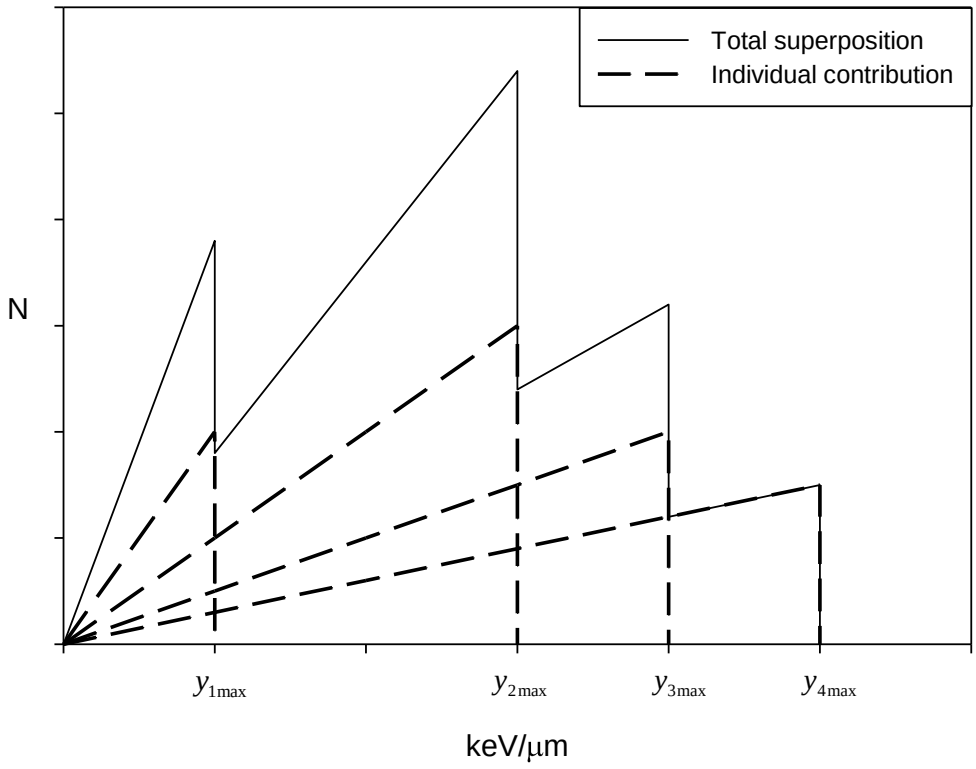


**Figure 10.** A lineal energy spectrum is a superposition of many individual triangles.

Each triangle corresponds to a different LET value. In Figure 10 the corresponding LET spectrum would be composed of four discrete values. To determine the magnitude of those four LET quantities one must find the area of each of the four individual triangles. However, the individual contributions are unknown and only the superposition of the triangles is measured. The area of these triangles can be determined from the superposition curve. To find the area of the first two individual triangles we must find the area of the shaded region in Figure 11.

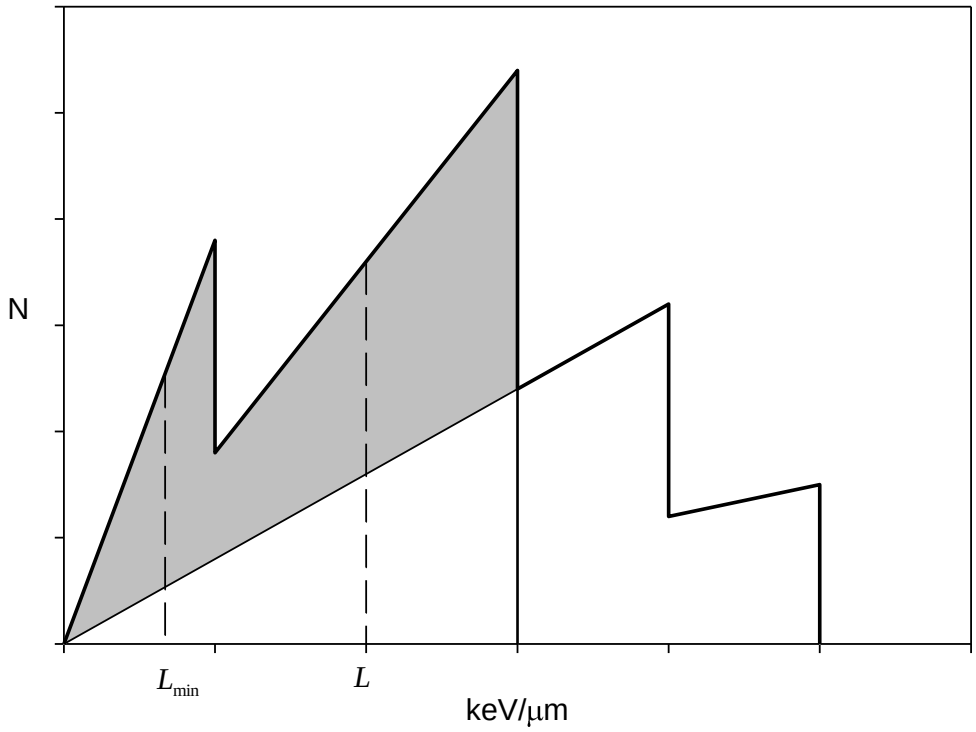


**Figure 11.** The shaded area is equal to the total number of counts from the two lowest discrete LET values.

The shaded region is equal to the combined area of the first two triangles and would also be equal to the total number of particles with LET between the smallest measured LET, $L_{min,}$ and the second LET value, $L$. This concept can be extended to the more realistic case where the LET spectrum is continuous and may be expressed as

$$\int_{L\min}^{L} N_L \, dy = \int_{0}^{y_0} N_y \, dy - \frac{1}{2} y_0 \; N_y(y_0) \qquad \textbf{( 68 )}$$

where $y_0$ is equal to $\frac{3}{2}L$. The first term of the right side of ( 68 ) is the entire area under the curve up to $y_0$. The second term subtracts the bottom triangular area that is present due to particles of higher LET. Using ( 68 ) we may now derive a general expression for

the LET spectrum $N_L$ in terms of the lineal energy spectrum, $N_y$. Plugging in for $y_0$ in terms of $L$ gives

$$\int_{L\min}^{L} N_L \, dy = \int_{0}^{3/2\,L} N_y \, dy - \frac{3}{4} L \, N_y(3/2\,L) \qquad \textbf{( 69 )}$$

To eliminate the integrals we may differentiate each side with respect to $L$.

$$\frac{d}{dL}\int_{L\min}^{L} N_L \, dy = \frac{d}{dL}\int_{0}^{3/2\,L} N_y \, dy - \frac{d}{dL}\left(\frac{3}{4} L \, N_y\left(3/2\,L\right)\right) \qquad \textbf{( 70 )}$$

$$N_L(L) = \frac{3}{2} N_y\left(3/2\,L\right) - \frac{3}{4}\left( N_y(3/2\,L) + L\frac{3}{2}\frac{dN_y(3/2\,L)}{dL}\right) \qquad \textbf{( 71 )}$$

We now have a term for the LET spectrum as a function of the lineal energy spectrum for any given value of $L$. Simplifying further give us

$$N_L(L) = \frac{3}{4}\left( N_y(3/2\,L) - L\frac{3}{2}\frac{dN_y(3/2\,L)}{dL}\right). \qquad \textbf{( 72 )}$$

So any value of the LET spectrum at any point with $L$ may be calculated from the count value and slope at the position $3/2\,L$ on the lineal energy spectrum. This method is rarely used since determining the slope of a measured spectrum is difficult and often requires much smoothing of the data. It is more common to use the frequency-averaged and dose-

averaged lineal energies of a spectrum as a relative measurement of the LET of the incident beam.

# CHAPTER V

# MATERIALS

## 5.0 Detector Design

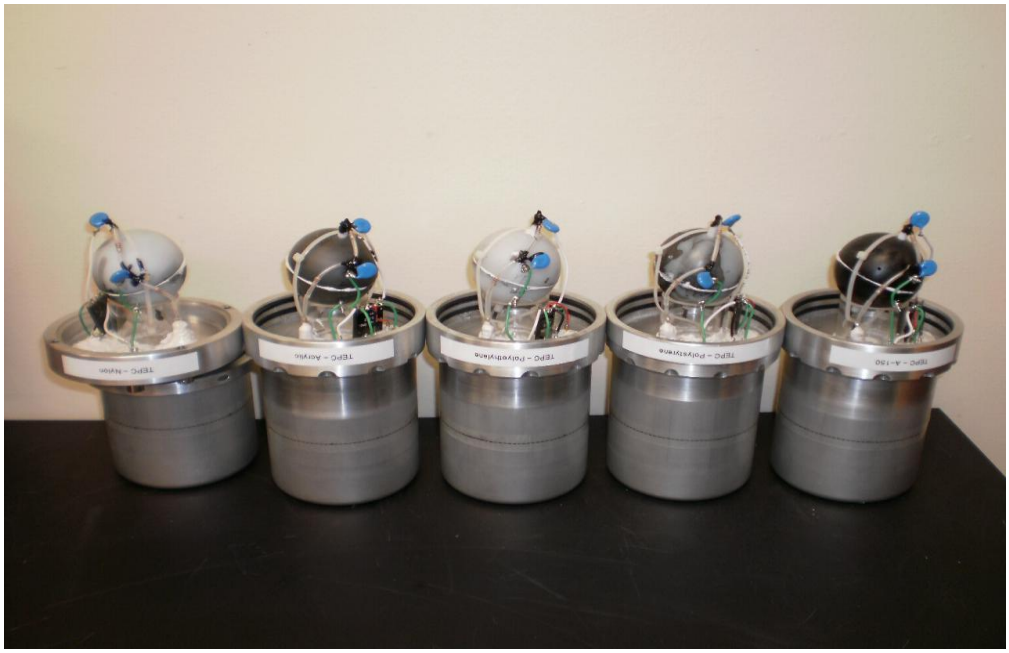

**Figure 12.** The five proportional counters fabricated for this study. From left to right: Nylon, acrylic, polyethylene, polystyrene and A-150 tissue equivalent plastic.

The proportional counters used in this study, shown in Figure 12, were designed and fabricated at the Radiation Physics Laboratory at Oklahoma State University and follow the Benjamin design (Benjamin et al., 1968). The TEPC design is illustrated in Figure

13. Each detector contains a spherical plastic ionization cavity with a 2” outer diameter. The cavities are hollow and have a wall thickness of 3 mm. A single stainless steel anode wire (0.05 mm diameter) runs vertically through the center of each cavity and is held at a positive high voltage.

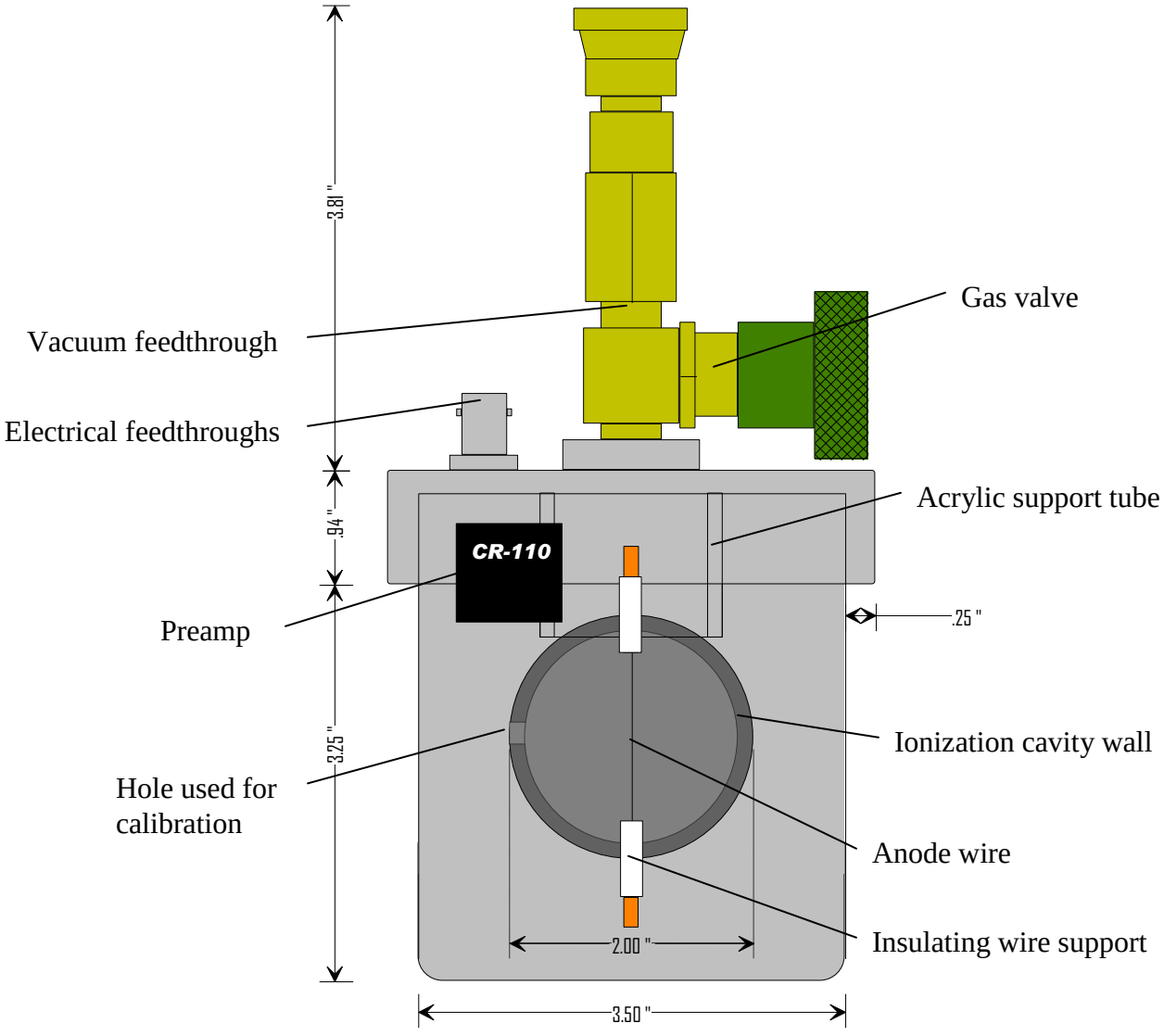


**Figure 13.** Diagram of the TEPC design.

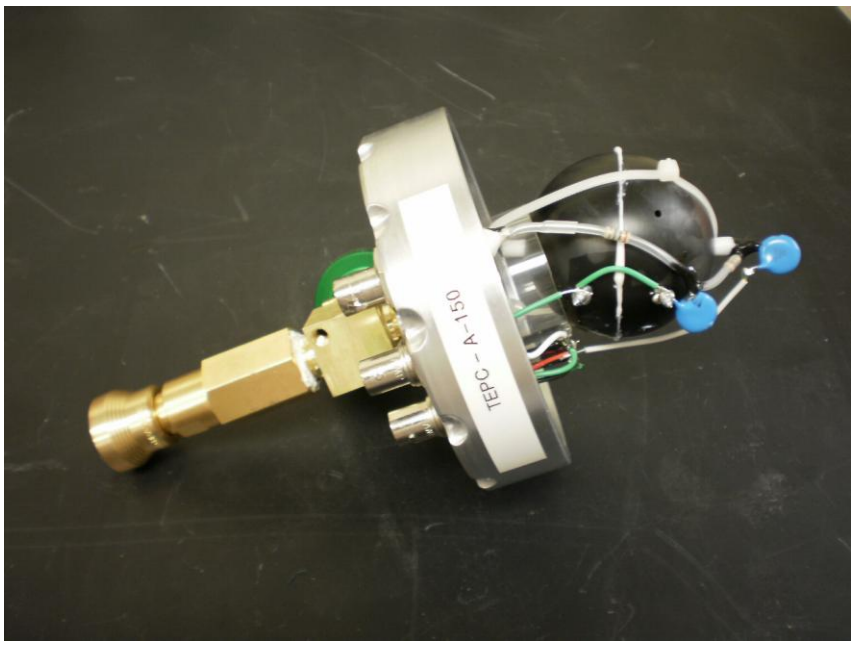


**Figure 14.** The lid and ionization chamber of the A-150 TEPC.

The inside of the spherical plastic cavities are coated with colloidal graphite (Aerodag G) to create a conductive surface. The thickness of the graphite is estimated to be only a few microns. The interior of the plastic spherical shell is held at ground. The plastic chamber is contained in a 3½" diameter cylindrical aluminum canister. The canisters (Zero mfg.) are open on one end and are 4" tall and 1 mm thick. An aluminum lid was fabricated for each canister, shown in Figure 14, which creates an air tight seal on the open end of the canister and also provides electrical and vacuum feedthroughs as shown in Figure 15. The spherical ionization cavities are attached to the lids using a 1½" diameter acrylic tube with a thickness of 5 mm which acts as a support.

**Figure 15.** One of the TEPCs fit onto the sealed canisters.

The canisters and cavities are filled with a methane-based tissue equivalent gas to a pressure of 173 Torr. The percentages by volume of the gas composition were 2.751% nitrogen gas, 29.99% carbon dioxide, and 67.26% methane which match closely with the methane-based gas originally used by Rossi (Rossi and Failla, 1956). The proportional counters are operated at a voltage of +1400 V which is within the proportional region typical for a detector of this volume and pressure (Korff, 1942).

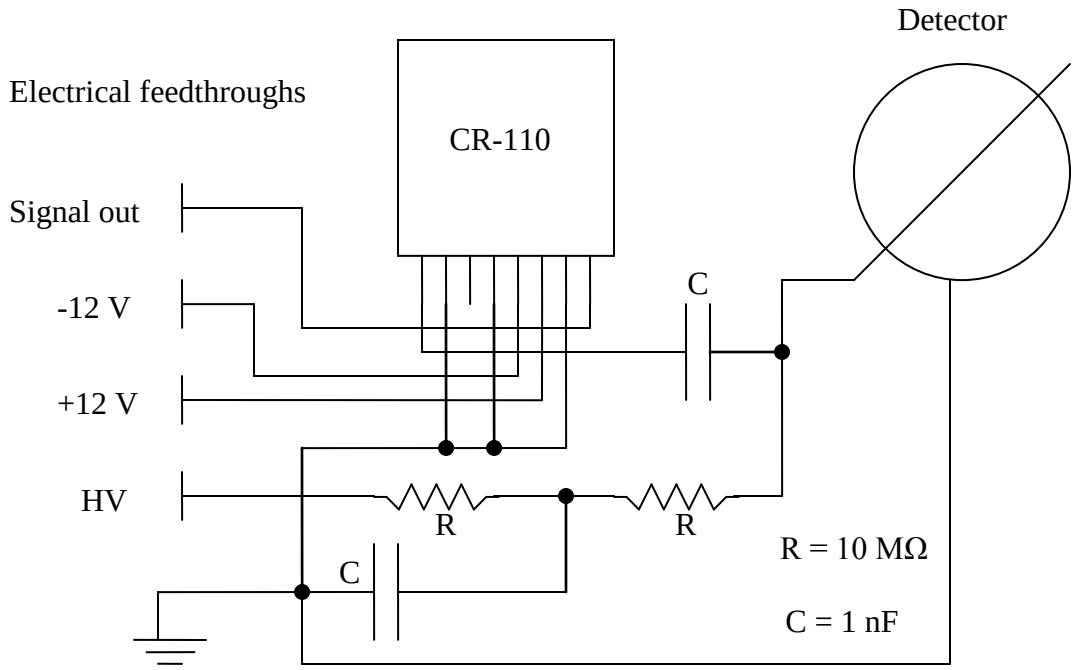


**Figure 16.** The TEPC circuit diagram.

A Cremat CR-110 preamplifier is also mounted inside the canister which receives and amplifies the pulses from the anode wire via capacitive coupling. The circuit diagram for the TEPCs is shown in Figure 16. The amplified pulse is transmitted through the electrical feedthroughs of the lid to a Canberra model 2020 spectroscopy amplifier. The amplified signal is then sent to an Amptek 8000A pocket MCA and the spectrum is read out and recorded on a laptop using the Amptek ADMCA software. The detector was designed to be easily opened and resealed.

Prior to the irradiations with protons or heavy ions, each of the five detectors was calibrated using a removable ~1 μCi $^{241}$Am alpha particle source placed on the exterior of

the plastic ionization cavity (Dietze et al., 1984; Schrewe et al., 1988). The $^{241}$Am source is attached to the ionization cavity over the location of a small hole in the ionization cavity wall. This allows alpha particles emitted from the $^{241}$Am to pass into the sensitive volume of the detector and cross the full diameter of the cavity. The emitted alpha particles have an energy of 5.486 MeV which corresponds to an LET of 82.8 keV/μm in water. The pulse created on the anode wire by the alpha particles as they pass through the detector is used to calibrate the channel number of the multichannel analyzer in units of lineal energy (Gerdung et al., 1995). After calibration and before the TEPC was irradiated, the $^{241}$Am is removed from the detector.

## 5.1. Gas Gain

It was found after repeated calibration measurements that the primary peak of the $^{241}$Am source would shift to lower lineal energies when multiple measurements were taken in succession. It was discovered that this effect was more prominent when calibrations were done directly following the gas filling of the detector. The relative gas gain of the detector was measured periodically following the gas filling of the detector to two different pressures. The data is shown in Figure 17.

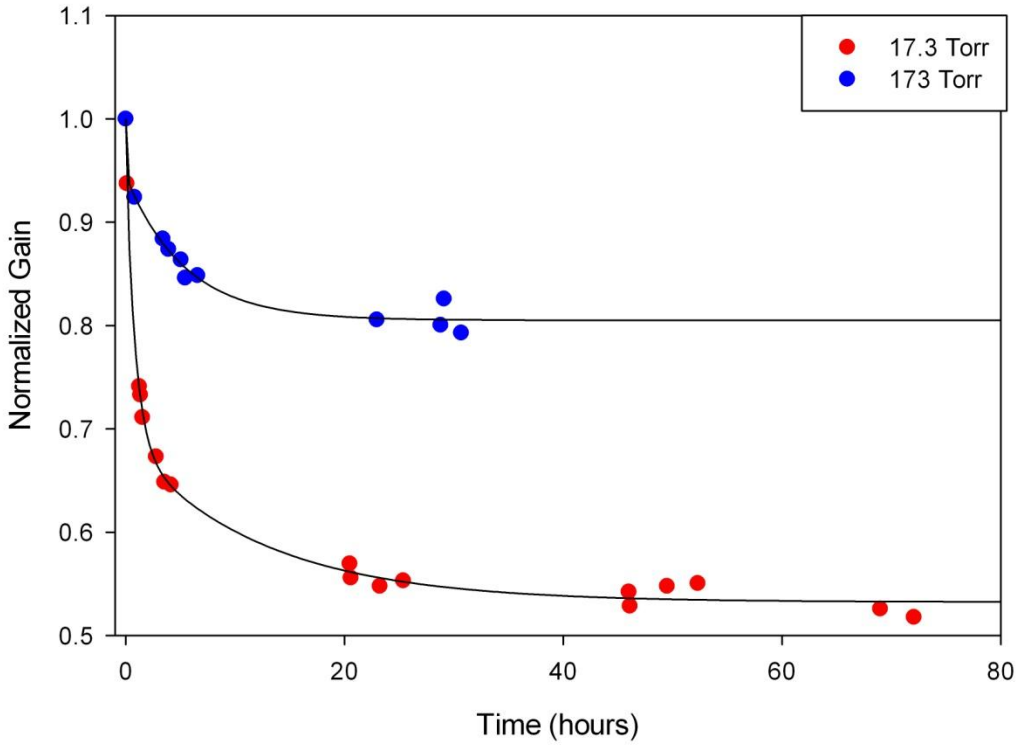


**Figure 17.** The gas gain of the same TEPC as a function of time immediately following the filling of the detector with tissue equivalent gas to two different pressures.

The change in gas gain is due to the outgassing of the materials used in the detector which affect the composition of the gas. Outgassing was shown to have less of an effect on the gas gain of the detector when the detector was filled to higher pressures. This is because less outgassing occurs due to the higher pressure environment that the materials are in, but the effect on gas gain is also decreased because the amount of tissue equivalent gas in the detector is also larger at higher pressures. The effect gas composition has on gas gain was observed by Rossi (Rossi and Failla, 1956), although the change in their gas composition was due primarily to the evaporation of a gel used in their detector and not

the outgassing of other solids. It was decided to use the higher pressure of 173 Torr to avoid larger changes in gas gain. For each experiment and calibration the detectors were allowed to outgas for at least 24 hours before any measurements were made. An added benefit of using a higher pressure is that the detector can then be operated at a higher voltage. Pulses generated due to ionizing radiation are larger due to the increased voltage. This allows the linear amplifier gain to be decreased which in turn lowers the noise level of the detector.

## 5.2. Ionization Cavity Wall Materials

The elemental composition of each of the five plastics used for the ionization cavities is shown in Table 1 and Figure 18, along with the ICRU definition of muscle tissue (ICRU 1983).

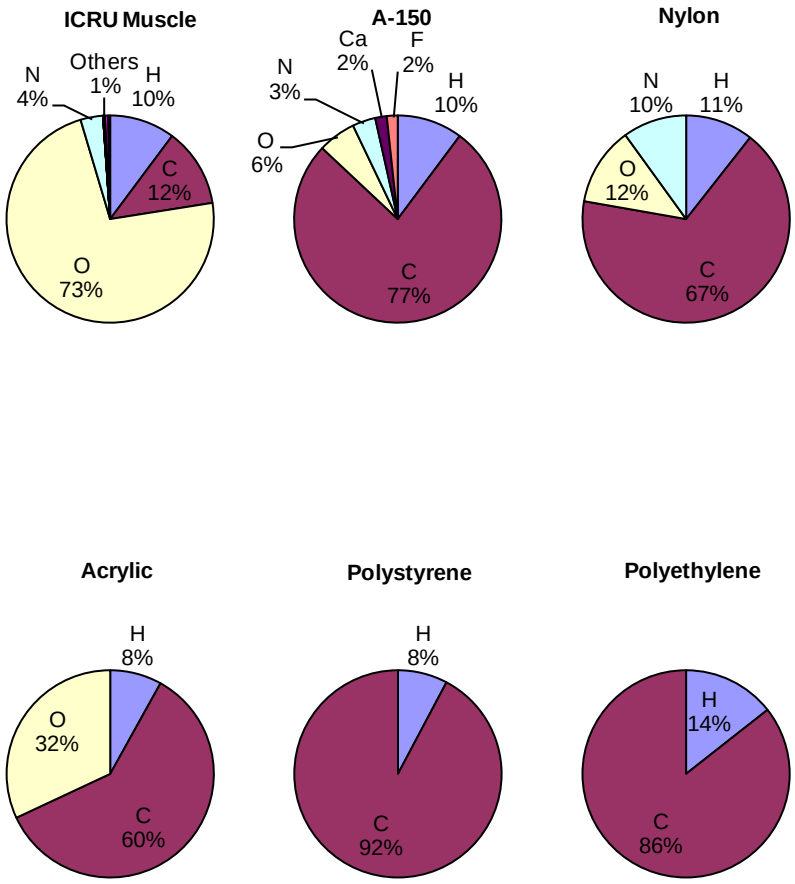


**Figure 18.** The elemental compositions by mass of the materials used in this study and of ICRU muscle.

**Table 1.** The mass percentages corresponding to Figure 18.

| | ICRU Muscle | A-150 | Nylon | Acrylic | Polystyrene | Polyethylene |
|---|---|---|---|---|---|---|
| **H** | **10.2** | **10.2** | **10.6** | **8.1** | **7.8** | **14.4** |
| **C** | **12.3** | **76.8** | **67.2** | **60.0** | **92.2** | **85.6** |
| **O** | **72.9** | **5.9** | **12.3** | **32.0** | | |
| **N** | **3.5** | **3.6** | **10.0** | | | |
| **Ca** | **0.007** | **1.8** | | | | |
| **F** | | **1.7** | | | | |
| **Na** | **0.08** | | | | | |
| **Mg** | **0.02** | | | | | |
| **P** | **0.2** | | | | | |
| **S** | **0.5** | | | | | |
| **K** | **0.3** | | | | | |

The concentrations of hydrogen and nitrogen in A-150 match quite closely with that of ICRU muscle. However, the concentrations of carbon and oxygen are nearly reversed. A-150 also contains fluorine in the form of $CaF_2$, as well as a much higher concentration of the heavier element Ca than does ICRU muscle. All five plastics have concentrations of hydrogen that are relatively close to that of ICRU muscle. Nylon has the next closest hydrogen concentration behind A-150 and also has a comparable nitrogen concentration. Acrylic has a much larger concentration of oxygen than any of the other plastics and also has the closest concentration of carbon compared to ICRU muscle of the five materials. There are several elements in the ICRU definition of muscle tissue that are not present in any of the plastics. The mass percentages shown in Figure 18 are usually the way in which the compositions of these materials are described. However, it may be more useful to consider the atomic percentages for these materials shown in Figure 19 and Table 2. The atomic percentages become more relevant when considering factors like neutron cross sections where the number of atoms in the materials is more important than the

mass of the atoms. By looking at the atomic percentages we can see that each of the materials is predominately made up of hydrogen. Polystyrene has the least amount of hydrogen at 50%, and polyethylene has the largest hydrogen content at 67%.

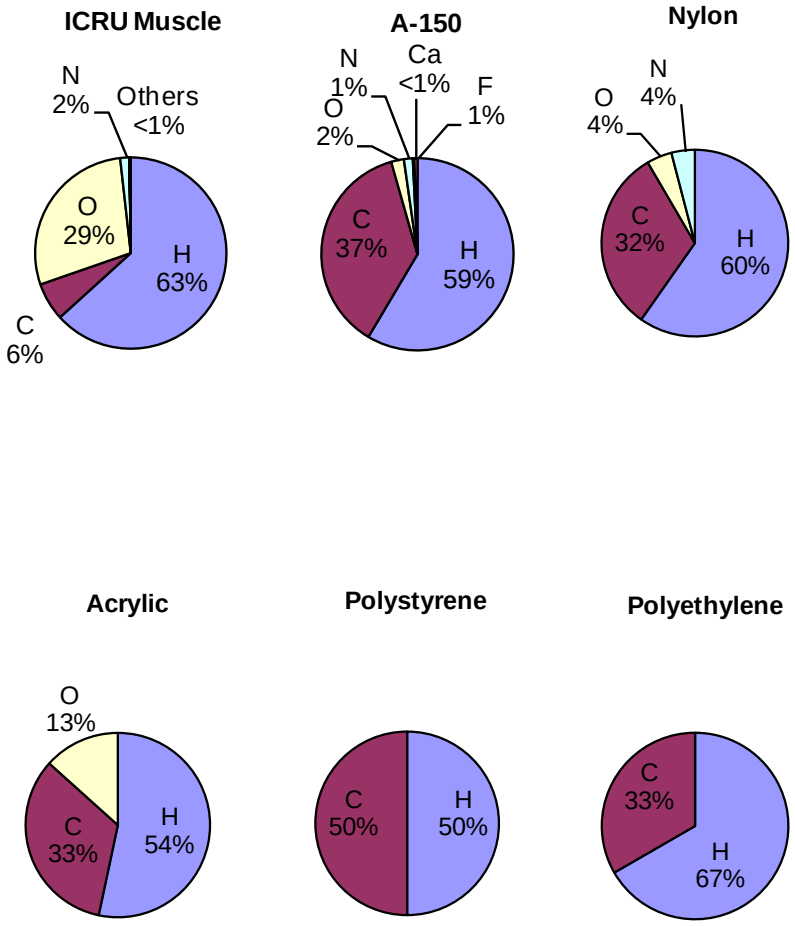


**Figure 19.** The atomic compositions of the materials used in this study and of ICRU muscle.

**Table 2.** The atomic percentages corresponding to Figure 19.

| | ICRU Muscle | A-150 | Nylon | Acrylic | Polystyrene | Polyethylene |
|---|---|---|---|---|---|---|
| **H** | **63.3** | **58.5** | **59.7** | **53.3** | **50** | **66.7** |
| **C** | **6.4** | **37.1** | **31.8** | **33.3** | **50** | **33.3** |
| **O** | **28.5** | **2.1** | **4.4** | **13.3** | | |
| **N** | **1.56** | **1.5** | **4.1** | | | |
| **Ca** | **0.001** | **0.3** | | | | |
| **F** | | **0.5** | | | | |
| **Na** | **0.02** | | | | | |
| **Mg** | **0.01** | | | | | |
| **P** | **0.04** | | | | | |
| **S** | **0.10** | | | | | |
| **K** | **0.05** | | | | | |

The composition of these materials will affect the way in which ionizing radiation interacts with them. Shonka originally developed A-150 tissue equivalent plastic for use in x-ray and neutron fields. Figure 20 shows mass attenuation coefficients for all five material used in this study as well as that of ICRU muscle. The plots have been multiplied by factors of ten in Figure 21 for clarity.

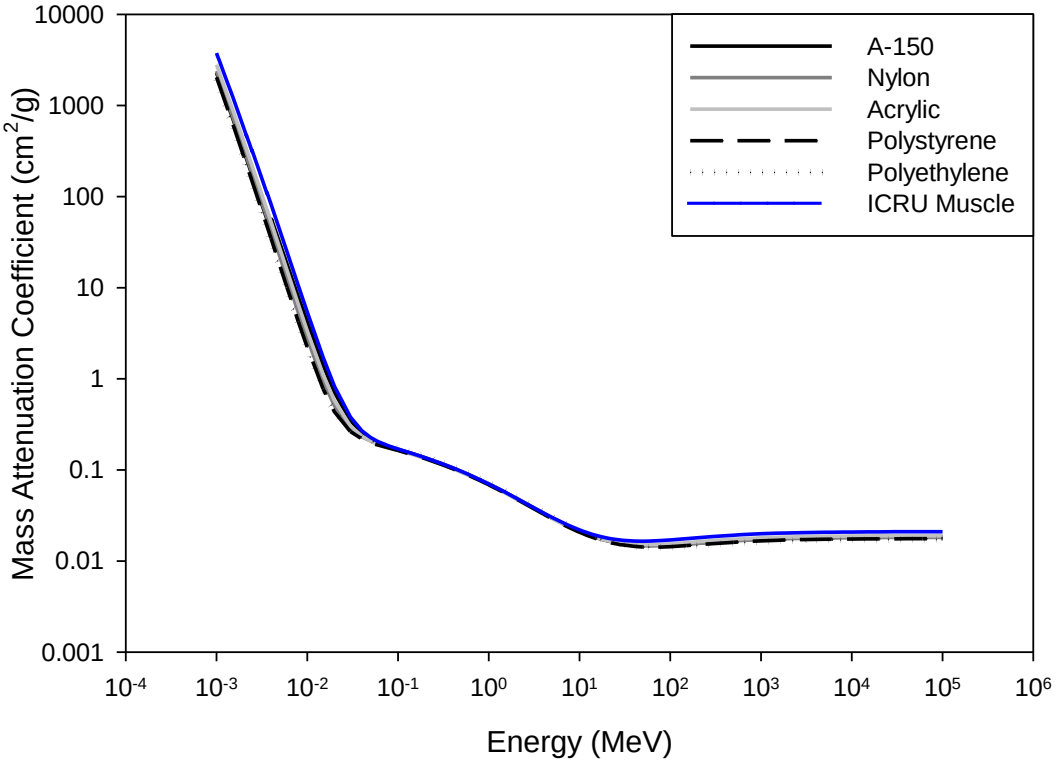


**Figure 20.** Mass attenuation coefficients for each ionization cavity wall material and ICRU muscle (NIST).

The mass attenuation coefficients for A-150 tissue equivalent plastic and ICRU muscle are nearly identical. However, the values for the other four materials match just as closely to ICRU muscle as A-150 tissue equivalent plastic does. In fact, a K-edge can be seen in A-150 due to its calcium content that is not seen in the other four materials or in ICRU muscle.

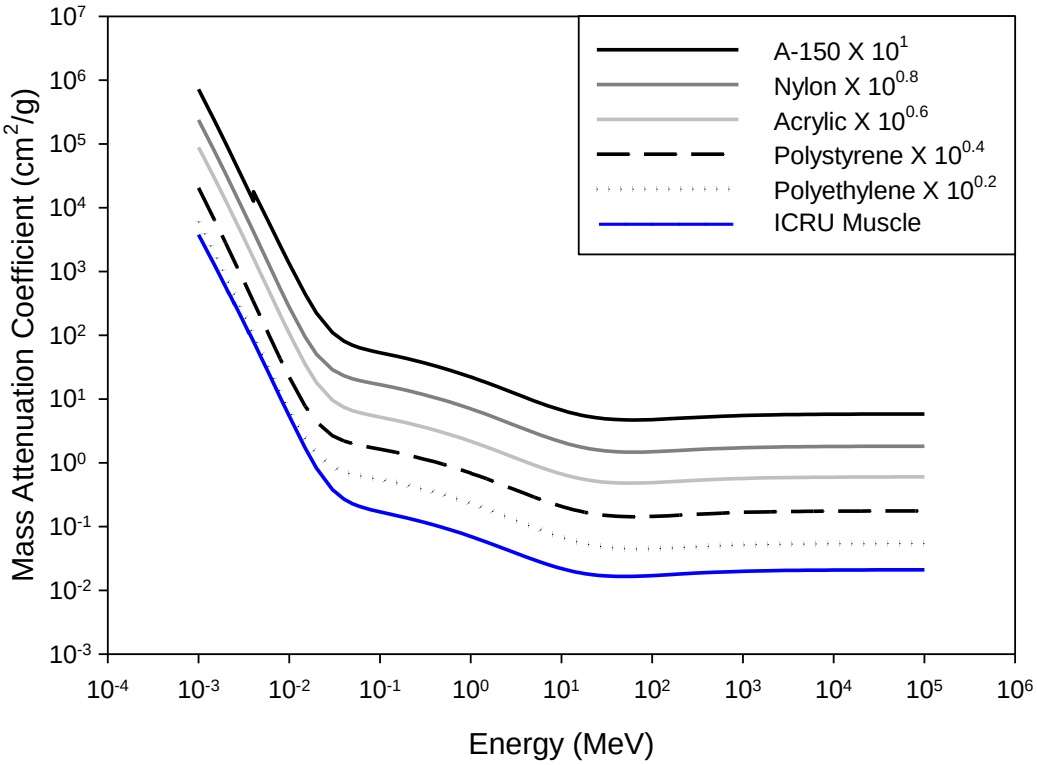


**Figure 21.** Mass attenuation coefficients for each ionization cavity wall material and ICRU muscle (NIST). The plots have been multiplied by factors of 10 for clarity.

For proton beams the amount of energy deposited in the materials is determined by the stopping powers shown in Figure 22. The proton stopping powers are also very similar for each material and only start to vary at very low proton energies. Acrylic matches more closely with ICRU muscle than the other four materials though no one material is significantly different from the rest.

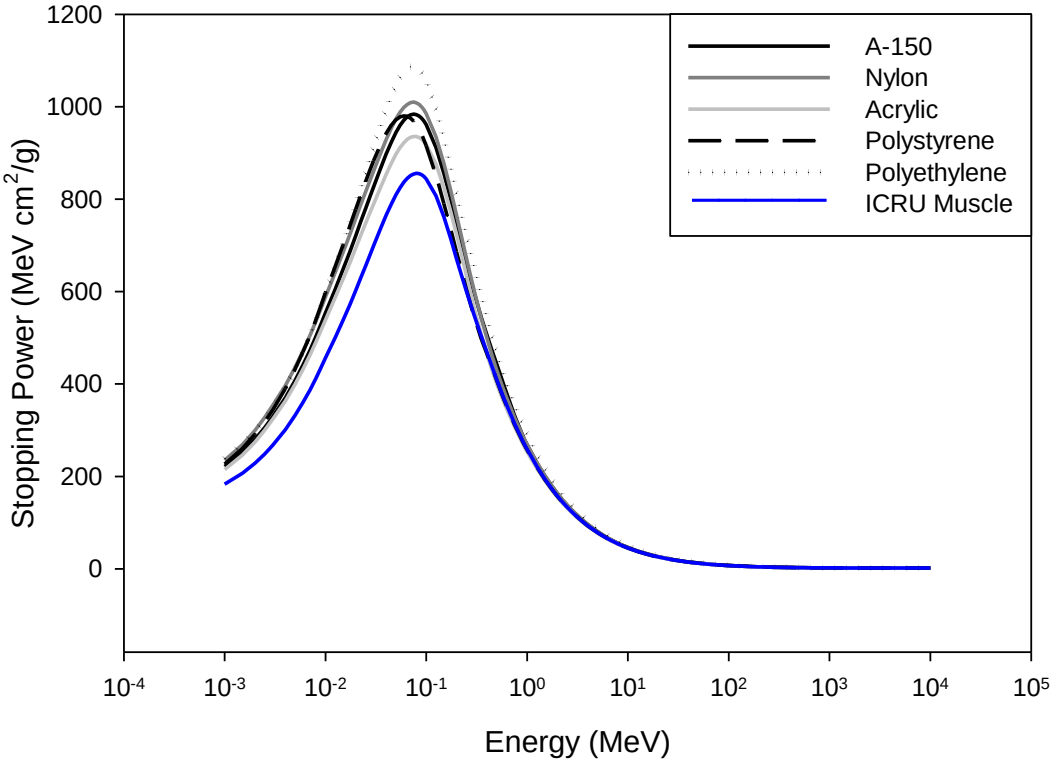


**Figure 22.** Proton stopping powers for the five ionization cavity wall materials and ICRU muscle (NIST).

The same can be said for the stopping powers of the five heavy ions used in this study. The stopping powers for helium, carbon, silicon, argon, and iron taken from SRIM are shown in Figures 23-27, respectively (Ziegler et al., 2008). In each case acrylic matches well with ICRU muscle. Polystyrene also matches quite well particularly for the three heavy ions. As was the case for protons, all of the stopping powers converge at higher energies. Polyethylene always has the highest stopping power for each ion at lower energies, but no one material is drastically different from the others.

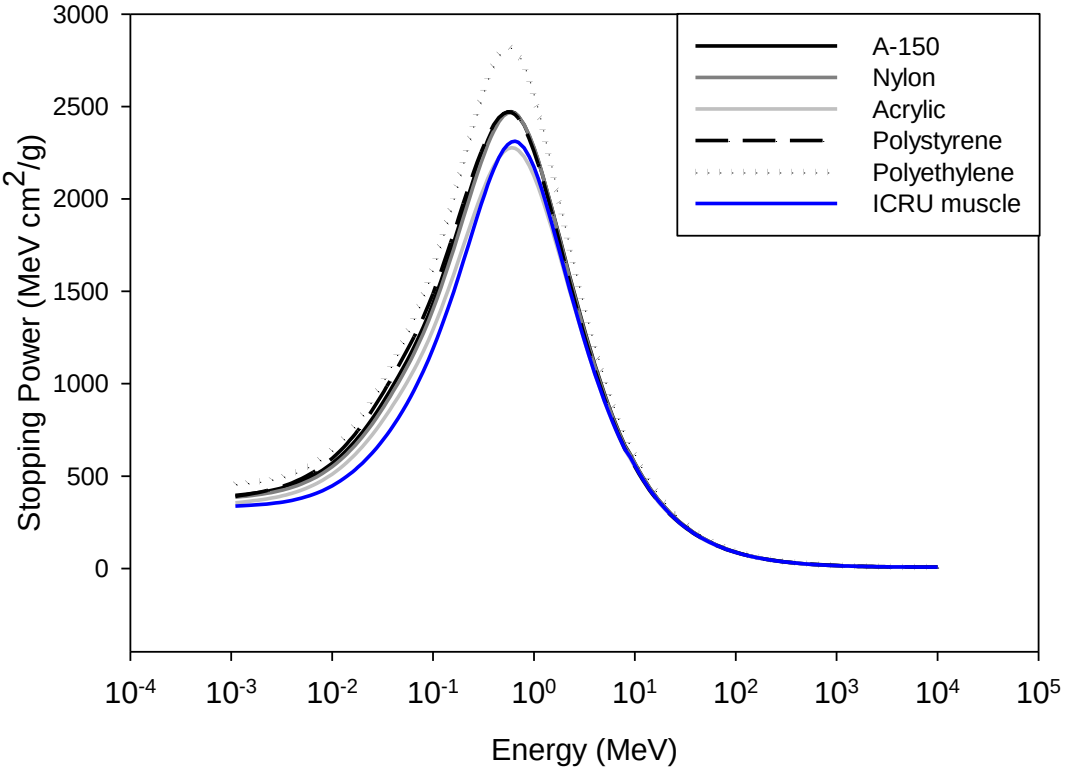


**Figure 23.** Helium stopping powers for the five ionization cavity wall materials and ICRU muscle (SRIM).

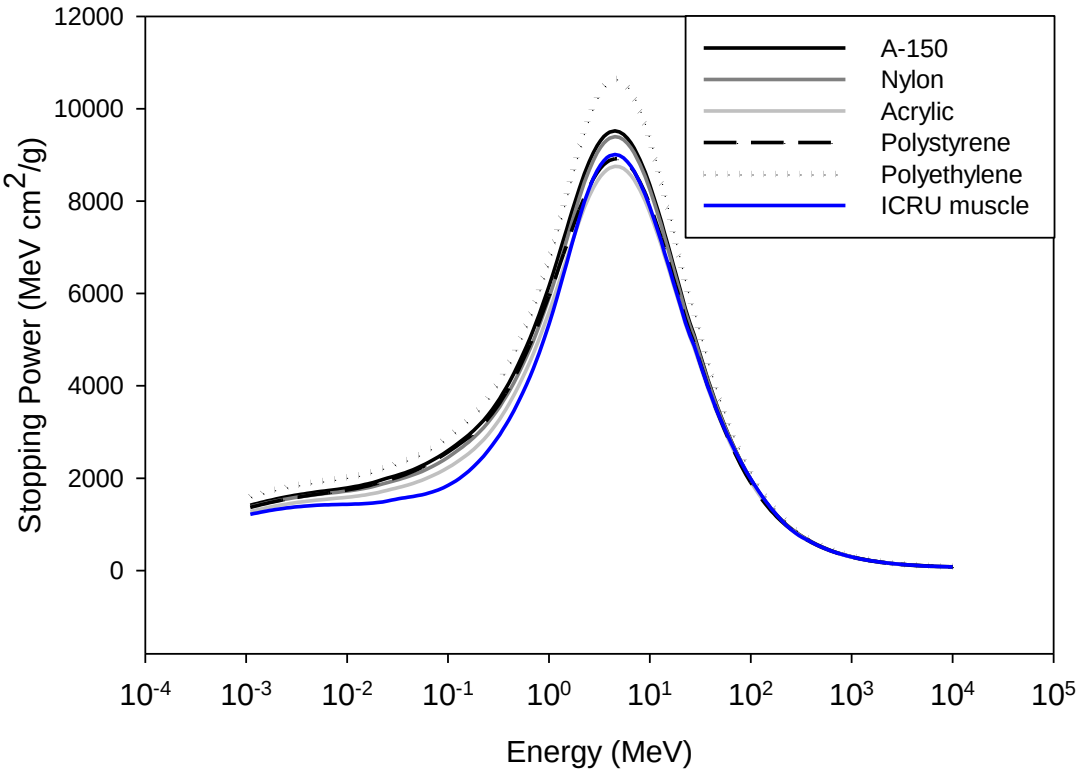


**Figure 24.** Carbon stopping powers for the five ionization cavity wall materials and ICRU muscle (SRIM).

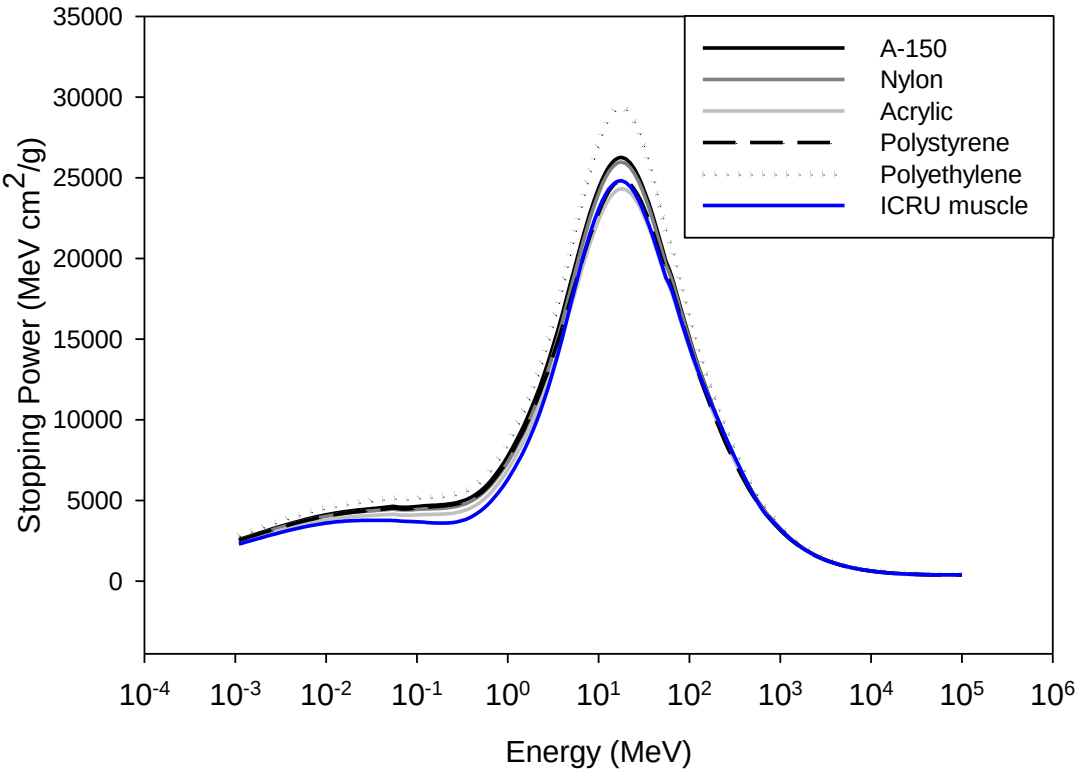


**Figure 25.** Silicon stopping powers for the five ionization cavity wall materials and ICRU muscle (SRIM).

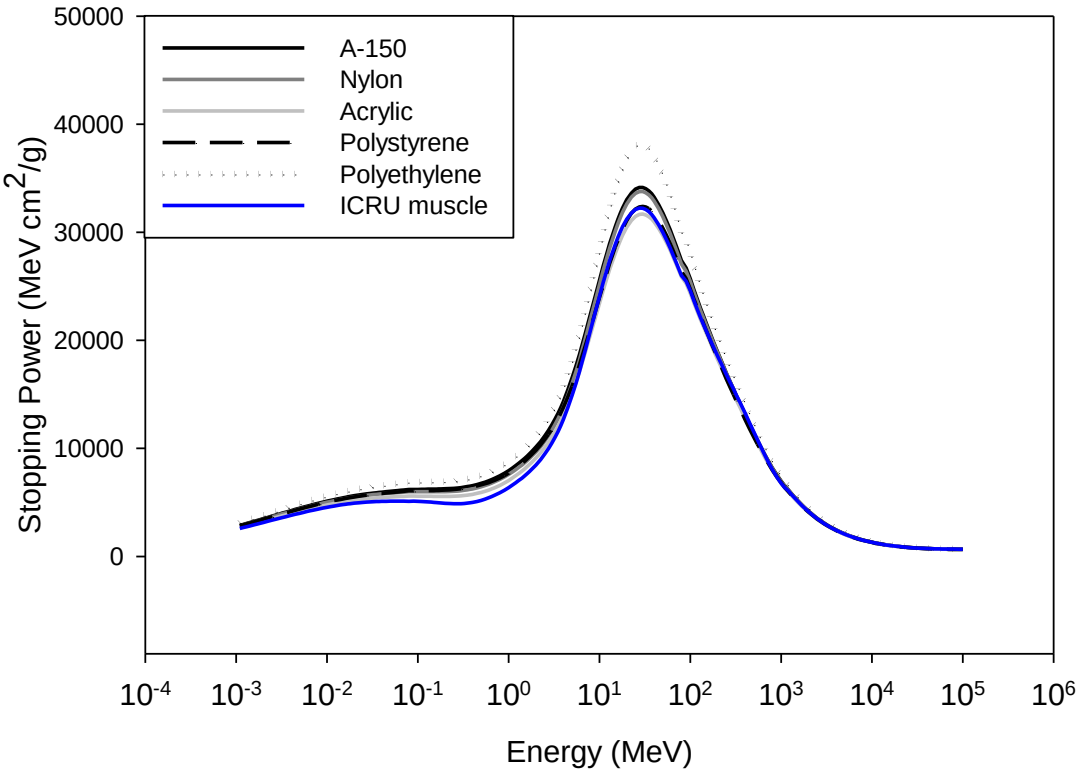


**Figure 26.** Argon stopping powers for the five ionization cavity wall materials and ICRU muscle (SRIM).

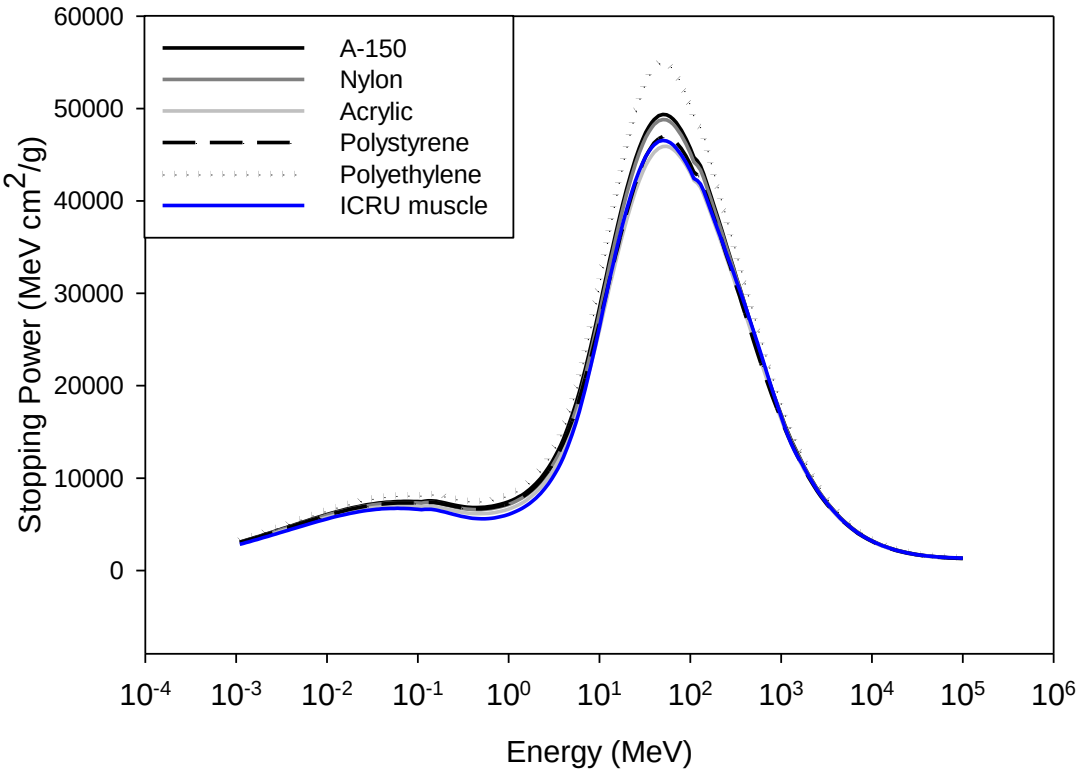


**Figure 27.** Iron stopping powers for the five ionization cavity wall materials and ICRU muscle (SRIM).

Neutron interactions with these materials are also of concern due to the presence of neutrons in space environments as well as the creation of secondary neutrons in radiation therapy beams.

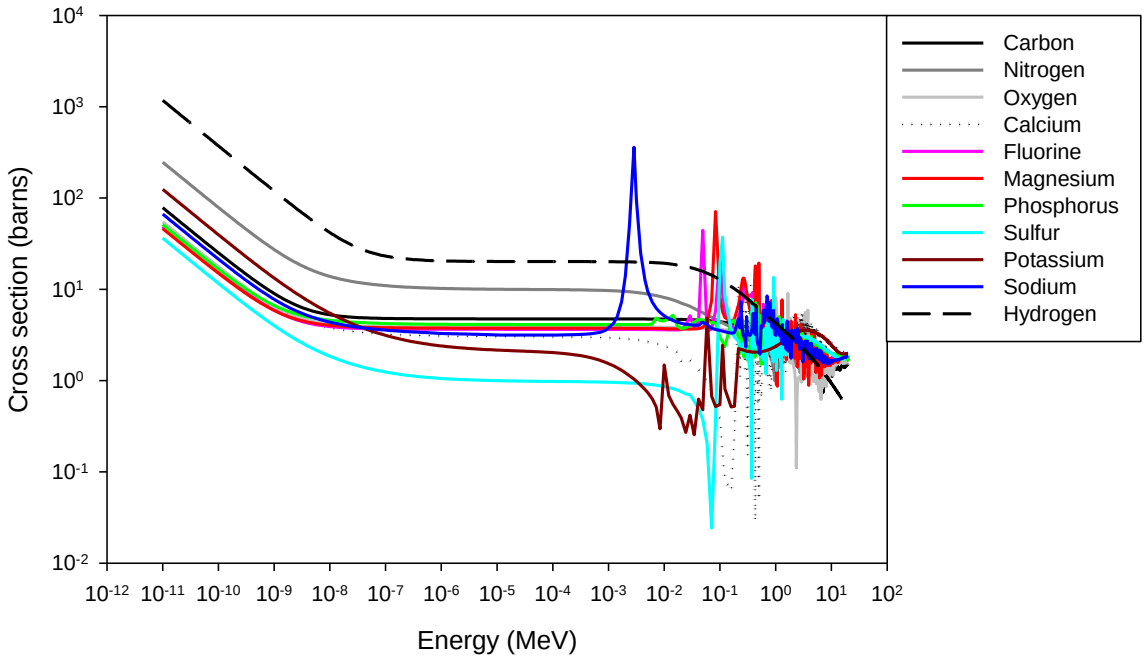


**Figure 28.** The total neutron cross section of each element found in the ionization cavity wall material or ICRU muscle (NNDC).

Figure 28 shows the total neutron cross sections for each of the elements that are found in any of the ionization chamber wall materials or in ICRU muscle (NNDC). Hydrogen has a total neutron cross section that is nearly an order of magnitude larger than any of the other elements shown. The hydrogen content of each material will then have the most effect on the neutron response of the material. By using the atomic percentages for each material from Table 2 and the neutron cross sections shown in Figure 28, we can calculate an average total neutron cross section for each ionization cavity wall material and ICRU muscle as shown in Figure 29. In Figure 30, the same values have again been multiplied by factors of ten in order to distinguish the individual plots. The cross sections are very similar for all materials. This similarity is caused by the similar hydrogen content across all the materials including ICRU muscle. While the mass percentage of

hydrogen in these materials is only about 10%, the atomic percentage is 50% or higher for all of these materials. For this reason, the hydrogen neutron cross section dominates the overall neutron cross section for each material.

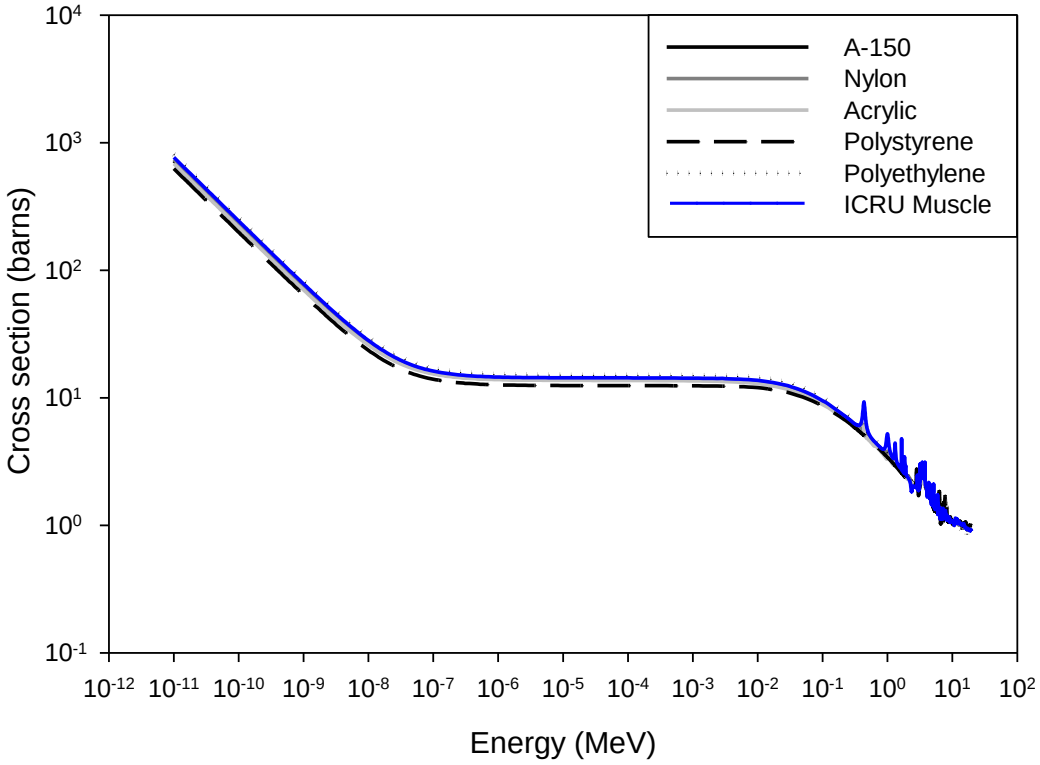


**Figure 29.** The average total neutron cross section for each of the ionization chamber wall materials and ICRU muscle.

Polyethylene has the highest average total neutron cross section due to the fact that it also has the highest concentration of hydrogen. Likewise, polystyrene has the lowest average total neutron section because it has the lowest concentration of hydrogen. The other plastics and ICRU muscle fall in between polyethylene and polystyrene.

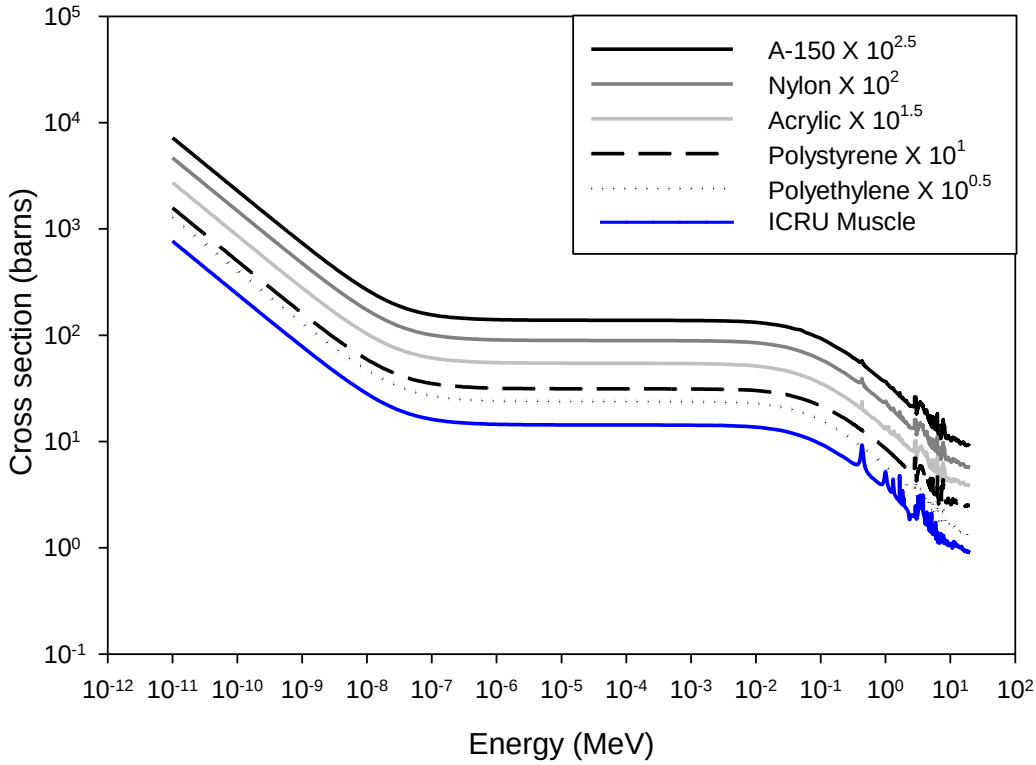


**Figure 30.** The average total neutron cross section for each of the ionization chamber wall materials and ICRU muscle. The plots have been multiplied by factors of 10 for clarity.

Based on the previously shown values, there should not be a significant difference between the materials in response to photon, proton, heavy ion, or neutron fields.

# CHAPTER VI

# METHODS

## 6.0 Proton Experiment

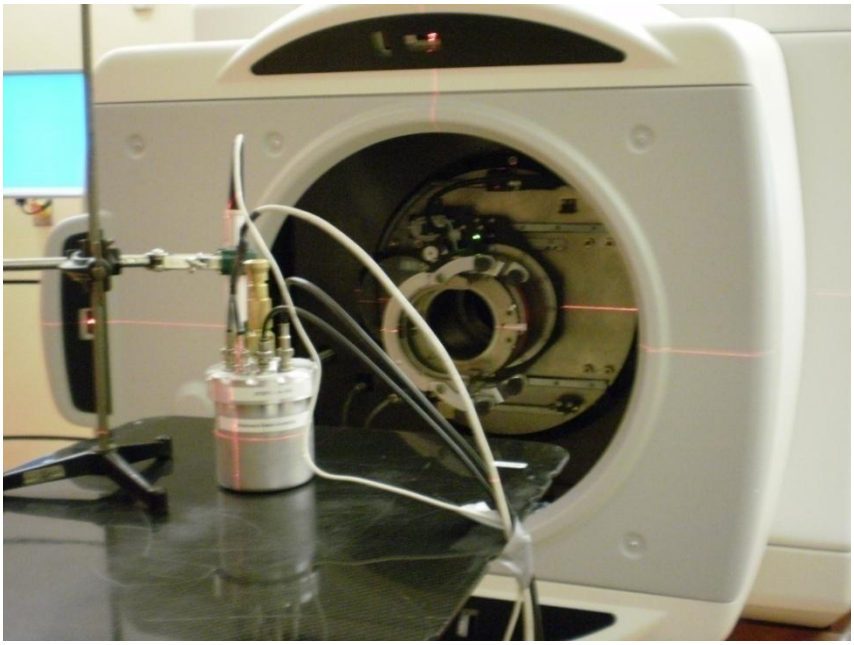

**Figure 31.** A TEPC on the treatment table and in front of the snout in one of the treatment rooms at the ProCure proton therapy center.

Exposures of the five TEPCs were carried out using proton beams at the ProCure proton therapy center in Oklahoma City. Three different proton energies—87 MeV, 162 MeV, and 222 MeV—were used from a 230 MeV IBA cyclotron. The beam energies, ranges in water, and LETs are shown in Table 3. The gain used on the linear amplifier is also

given in the table. The same gain of 300 was used for each beam due to small difference in LET of the beams.

**Table 3.** The three proton beams used at ProCure from the 230 MeV cyclotron. The range in water is given as well as the gain used on the linear amplifier to measure the lineal energy spectrum of each beam.

| Beam | Energy (MeV/amu) | Range (cm) | LET (keV/µm) | Linear Amp. Gain |
|---|---|---|---|---|
| H | 222 | 31 | 0.42 | 300 |
| H | 162 | 18 | 0.52 | 300 |
| H | 87 | 6 | 0.81 | 300 |

The beam energy was modulated far upstream of the patient treatment (exposure) room using a modulator wheel (Zheng et al., 2011). Exposure area was controlled by magnetically scanning the beam over a brass collimator in the patient room. For this experiment a circular collimator with an aperture diameter of 1.7 cm was used.

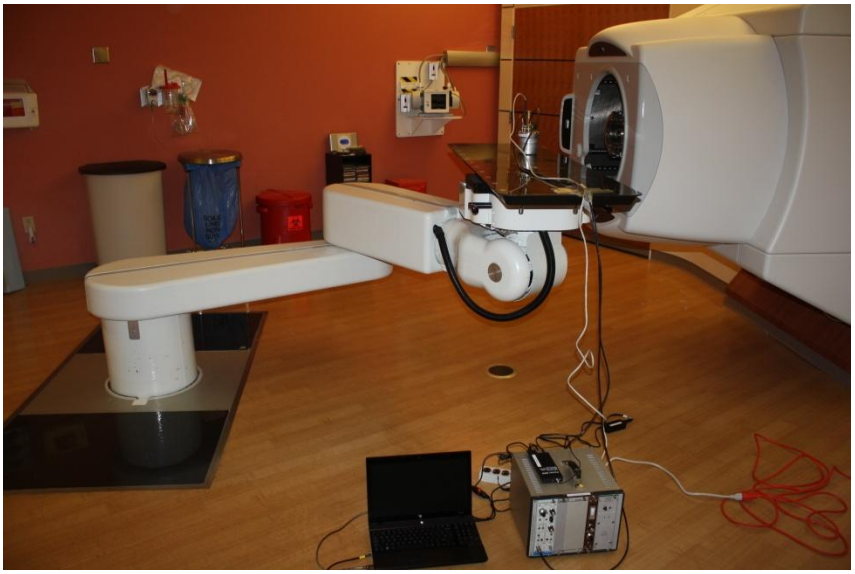

**Figure 32.** The experimental setup used in the proton beam experiment at the ProCure proton treatment center.

The proportional counters were exposed individually and were each positioned upright on the patient table at an isocenter distance of 100 cm from the beam snout as shown in Figure 31. The proportional counters were oriented vertically with respect to the horizontal proton beam so that the anode wire was perpendicular to the direction of the incident beam. The output of the TEPCs were connected to the Canberra model 2020 spectroscopy amplifier in a NIM bin on the floor of the treatment room. The NIM bin also contained the high voltage power supply. The output from the amplifier was directly connected to the Amptek 8000A pocket MCA. The experimental setup is shown in Figure 32 and Figure 33.

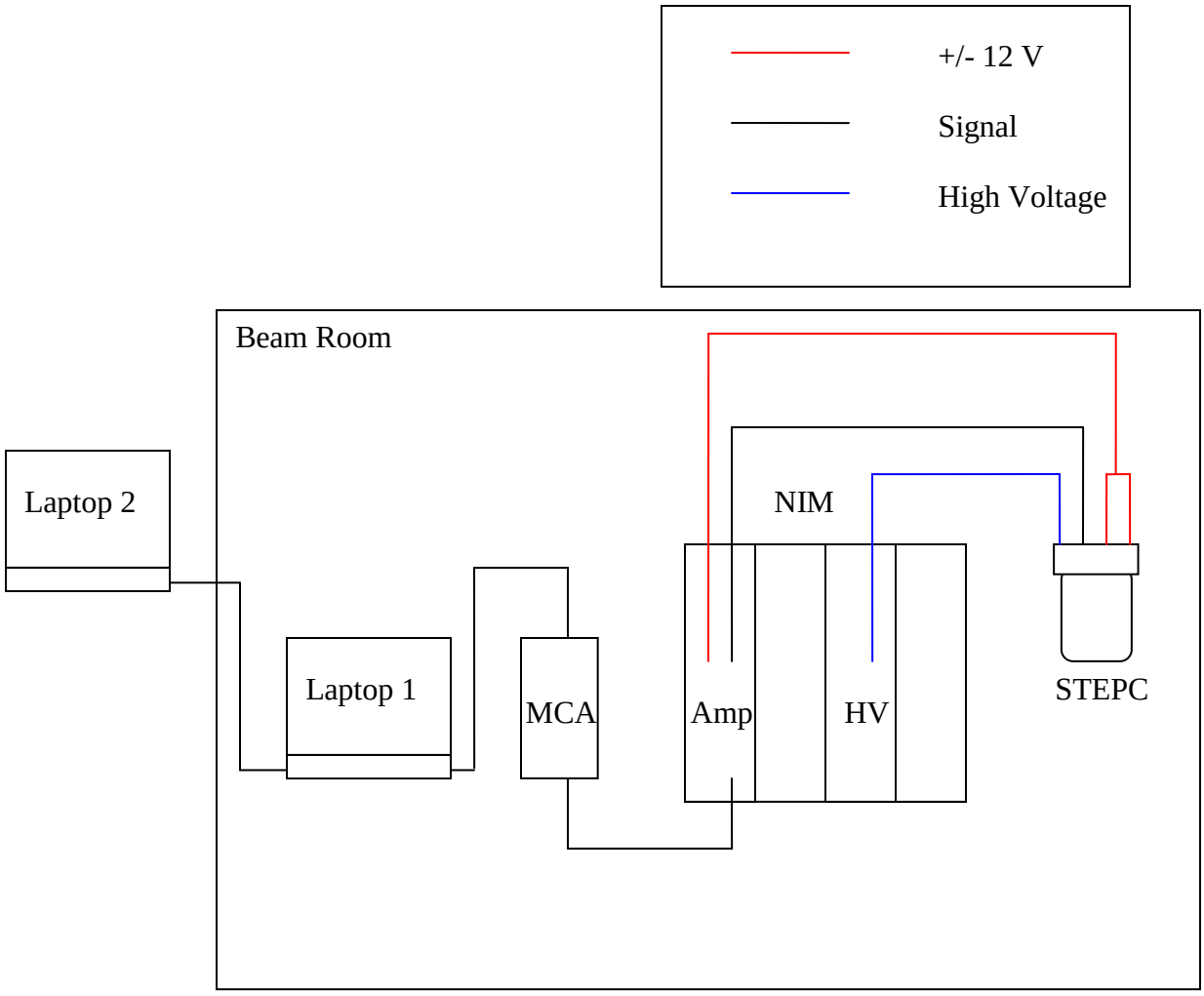


**Figure 33.** A diagram of the experimental setup used in the proton experiment.

Lineal energy spectra were measured with all five detectors for each of the three proton beam energies. A low flux beam (~450 particles $cm^{-2}$ $s^{-1}$) was used so as not to saturate the detectors. Each irradiation was to approximately the same number of machine units (MU) from the cyclotron and was on average 10.9 MU, resulting in ~500,000 proton counts per irradiation as measured by the TEPC. One MU for this machine is calibrated to deliver 1 cGy of dose to the center of the spread out Bragg peak (SOBP) using a beam

with a 16 cm range, 10 cm modulation beam width, and using a 10 cm aperture. Delivery of 10.9 MU, for the beam energies and parameters used, and based on the $^{241}$Am alpha particle calibration, resulted in average absorbed doses measured by the proportional counters of 48.9 cGy, 19.1 cGy, and 8.9 cGy with proton beams of 87 MeV, 162 MeV, and 222 MeV

## 6.1. Heavy Ion Experiment

Exposures of the five TEPCs were carried out using heavy ion beams produced by the Heavy Ion Medical Accelerator in Chiba (HIMAC) at the National Institute of Radiological Sciences (NIRS) in Japan. Five different heavy ions beams were used: 143 MeV/amu He, 265 MeV/amu C, 440 MeV/amu Si, 430 MeV/amu Ar, and 421 MeV/amu Fe. Exposures were done using a 10x10 cm$^2$ field. The beam energies, ranges in water, and LETs are shown in Table 4. The gain used on the linear amplifier is also given in the table. The gain was adjusted for each beam due to the large differences between the LETs of the beams.

**Table 4.** The five heavy ion beams used from the synchrotron at HIMAC. The range in water is given as well as the gain used on the linear amplifier to measure the lineal energy spectrum of each beam.

| Beam | Energy (MeV/amu) | Range (cm) | LET (keV/µm) | Linear Amp. Gain |
|---|---|---|---|---|
| He | 143 | 14.5 | 2.3 | 195 |
| C | 265 | 13.9 | 13.7 | 45 |
| Si | 440 | 13.5 | 57.4 | 10 |
| Ar | 430 | 11.3 | 96.0 | 10 |
| Fe | 421 | 7.3 | 203.9 | 5 |

In some exposures the proportional counters were exposed individually and were each oriented vertically on the exposure table as shown in Figure 34 and Figure 35.

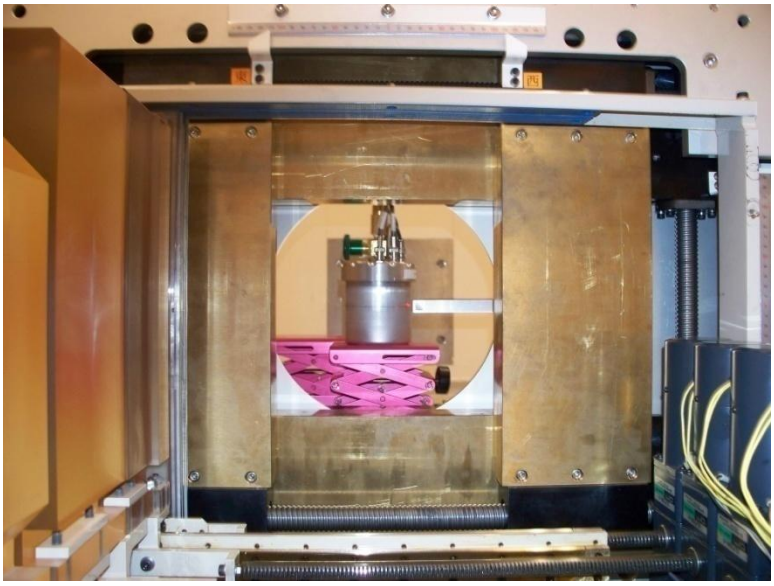

**Figure 34.** One of the TEPCs setup for irradiation in the exposure room at HIMAC

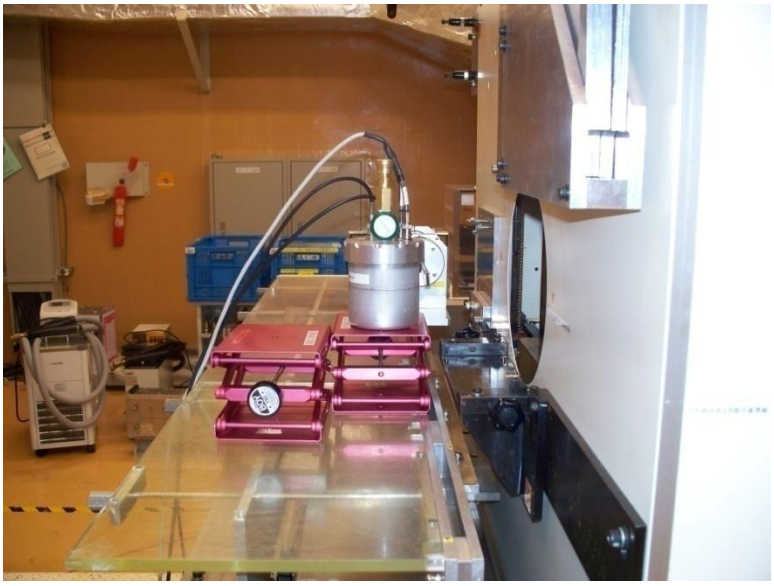

**Figure 35.** Side view of one of the TEPCs setup for irradiation at HIMAC.

Other exposures were done with multiple other detectors in the field since beam time was being shared with another research group. In these cases the proportional counters were

oriented horizontally to ensure that all detectors would fit within the beam field as shown in Figure 36.

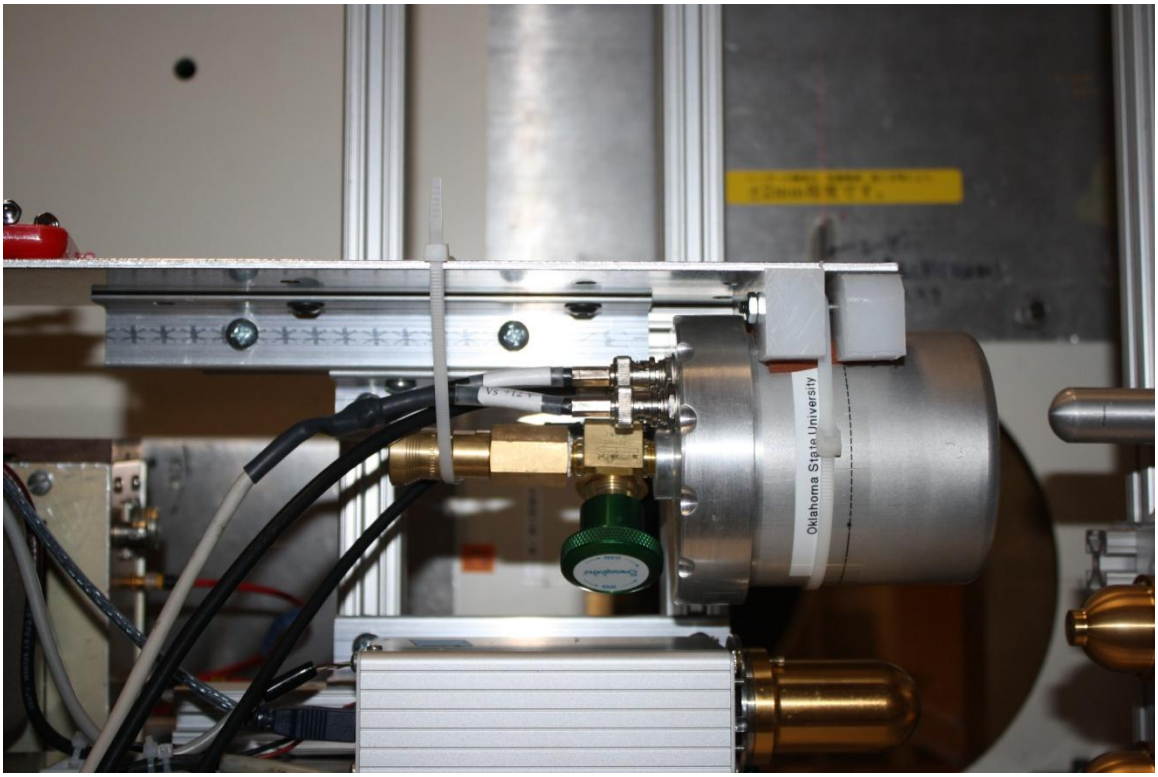


**Figure 36.** One of the TEPCs oriented horizontally for one of the HIMAC experiments.

In all exposures the anode wire was perpendicular to the direction of the incident beam. The same linear amplifier, high voltage power supply, and MCA were used as before in the proton experiments. However, the MCA and laptop was placed outside the exposure room as shown Figure 37. Lineal energy spectra were measured with all five detectors for each of the heavy ion beams. A low flux beam (~1000 particles $cm^{-2}$ $s^{-1}$) was used so as not to saturate the detectors. Each detector was exposed for at least five minutes and each measured spectrum consisted of approximately one million heavy ion counts.

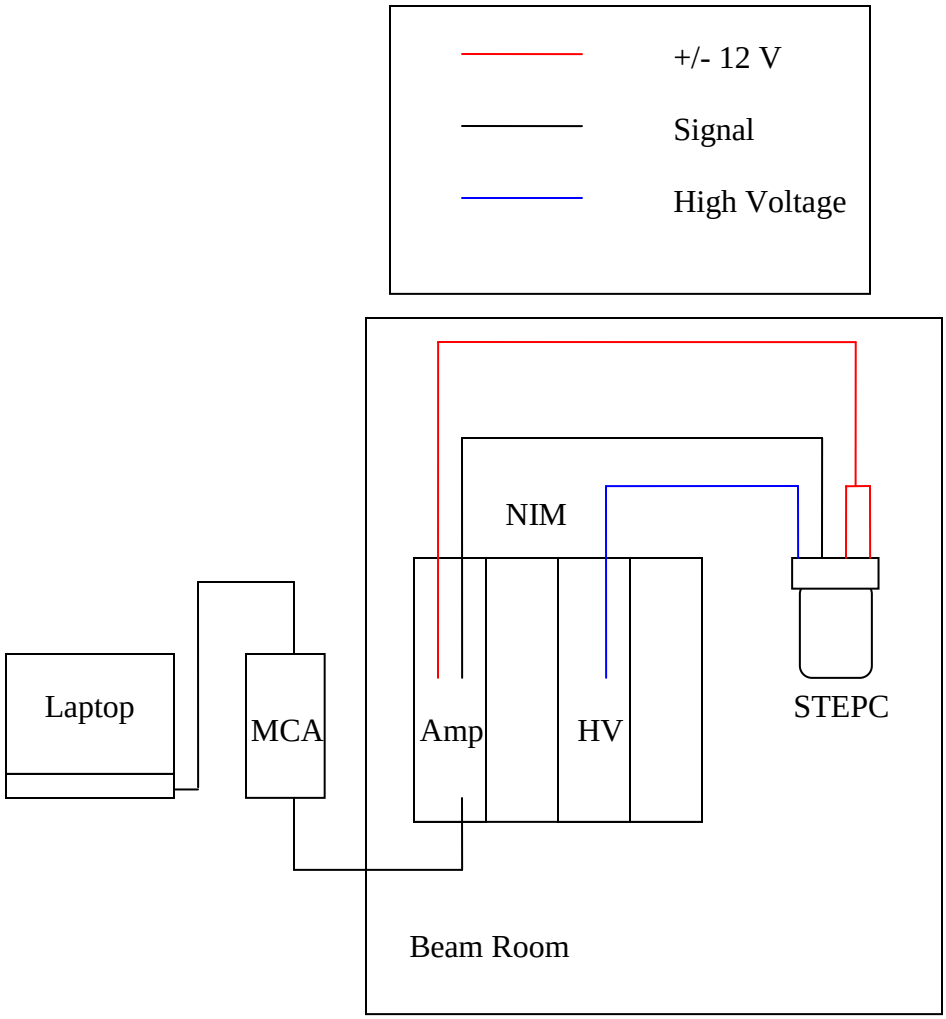


**Figure 37.** A diagram of the experimental setup used in the heavy ion experiment.

## 6.2. Simulation

Irradiations of the five TEPCs with the three proton beams and five heavy ion beams were simulated using the FLUKA Monte Carlo code (version 0.9-6, 2012). FLUKA is a useful code for studying the transport of different types of particles and their interaction with matter for an extensive range of energies from 1 keV to thousands of TeV (Fasso et al., 2003a, 2003b, 2005). In this study the geometry of the detector was modeled using

the FLUKA Combinatorial Geometry package where the inner gas region was surrounded by the five different types of plastic. The gas pressure inside the detector was kept at 173 Torr to simulate a tissue diameter of about 10 μm. The energy for electron and photon transport was set to 10 keV (Rollet et al., 2004, 2010). Delta ray production was switched on everywhere inside the gas region and in the ionization cavity wall material with a threshold of 10 keV. The deposited energy inside the gas region was scored on an event by event basis to acquire an energy distribution. Since the pressure of the gas inside the detector was low, 10 million primaries were used for reasonable statistical accuracy. Under these simulation conditions, the uncertainty of the absorbed dose in the gas region was estimated to be 1%.

# CHAPTER VII

# RESULTS

## 7.0 Protons – Experiment

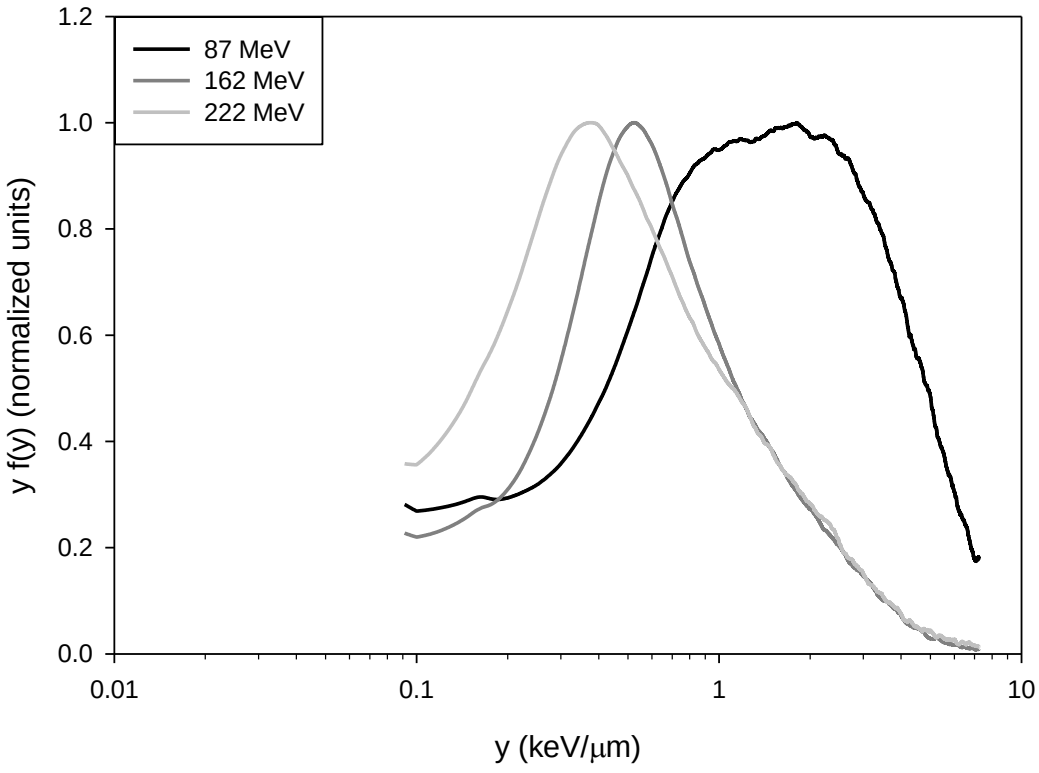


**Figure 38.** The lineal energy spectra from the A-150 TEPC for each proton beam. The ordinate axis is given as y f(y) so that the area under the each curve is proportional to the frequency of particles.

Figure 38 shows the lineal energy spectra measured in the A-150 TEPC for each proton energy. The primary ionization peak of the 87 MeV data is shifted to the right with respect to the others due to the higher LET of low energy protons. The peaks for the other two energies are largely coincident, which is not surprising given that the difference in LET between 222 MeV protons and 162 MeV protons in water is only about 0.1 keV/μm. The difference between the peak positions can still very easily be distinguished even given this small difference in LET.

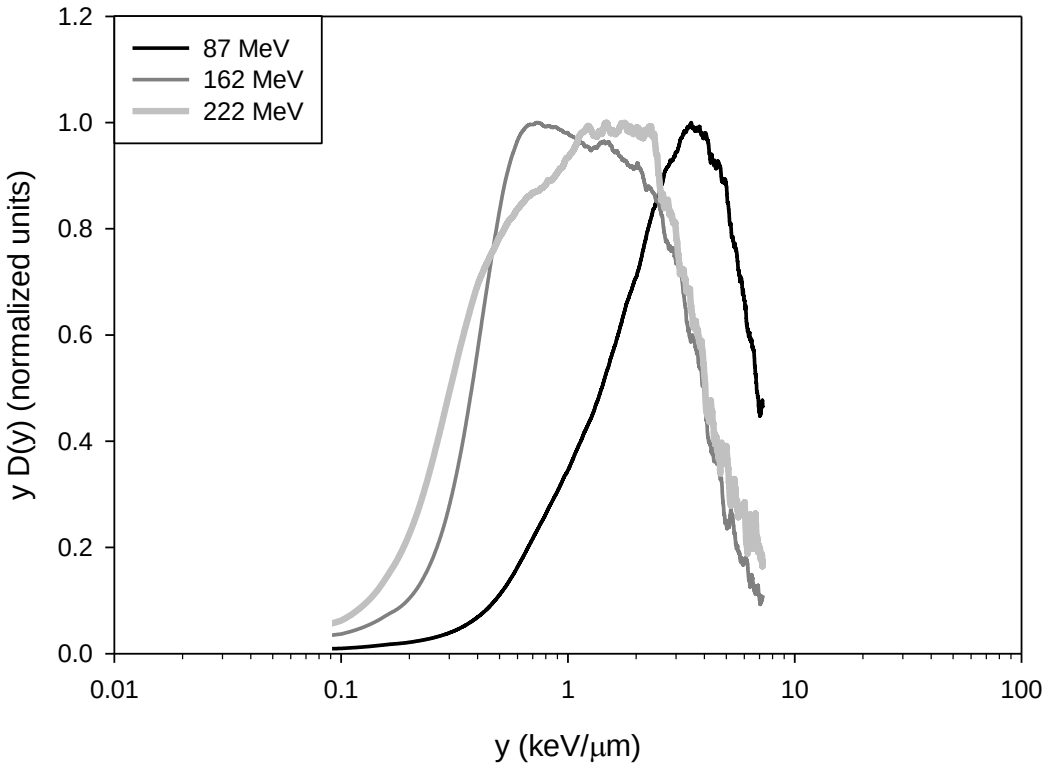


**Figure 39.** The lineal energy spectra from the A-150 TEPC for each proton beam. These are the same spectra shown in Figure 38 but the ordinate axis is given in terms of y D(y) so that the area under the each curve is proportional to dose.

Figure 39 shows the same spectra except that the ordinate axis is in terms of yD(y) so that the area under each curve is proportional to dose. The difference between the 222 MeV

and 162 MeV is much smaller when comparing their dose distributions than when comparing the frequency distributions.

Figures 40, 41, and 42 show comparisons between lineal energy spectra for each ionization cavity plastic at primary proton energies of 87 MeV, 162 MeV, and 222 MeV, respectively. The spectra measured using different ionization cavity materials are largely coincident for all three proton energies. There are, however, slight differences between the spectra.

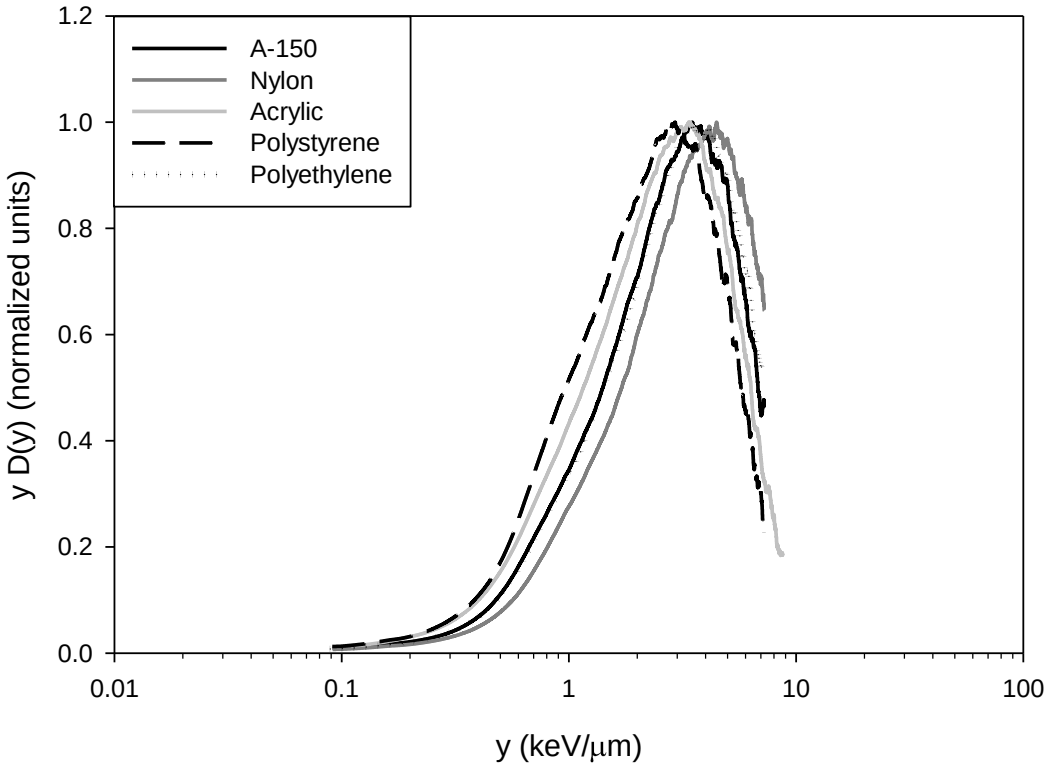


**Figure 40.** Lineal energy spectra taken with all five TEPCs for 87 MeV protons.

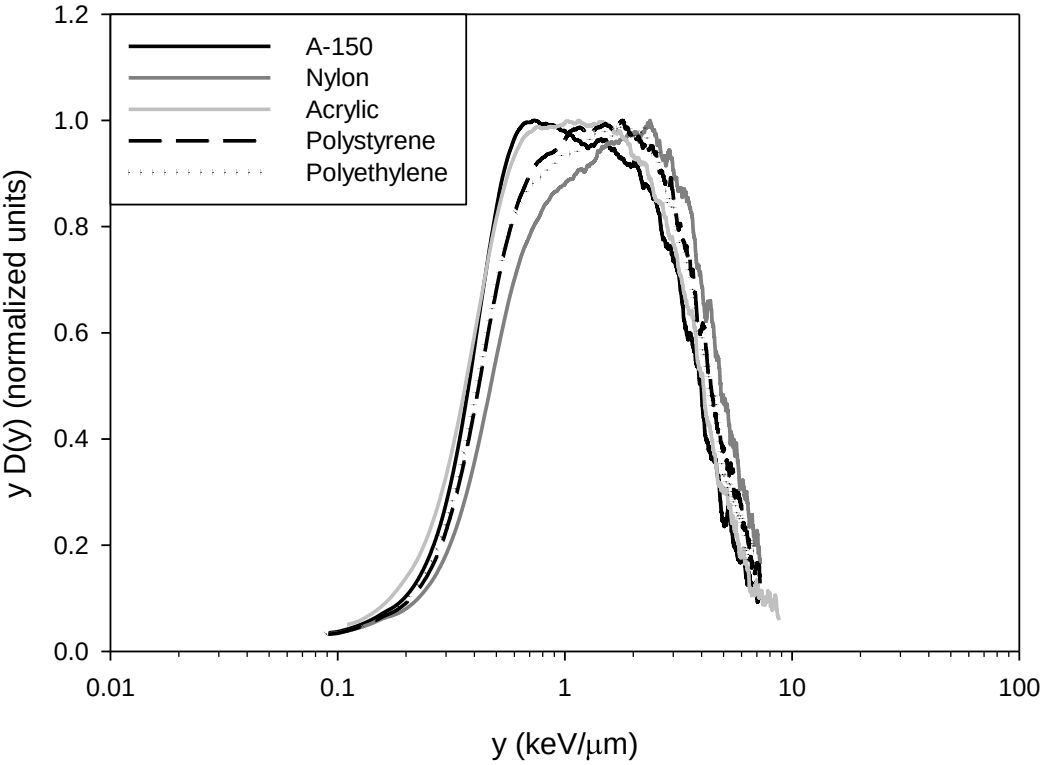


**Figure 41.** Lineal energy spectra taken with all five TEPCs for 162 MeV protons.

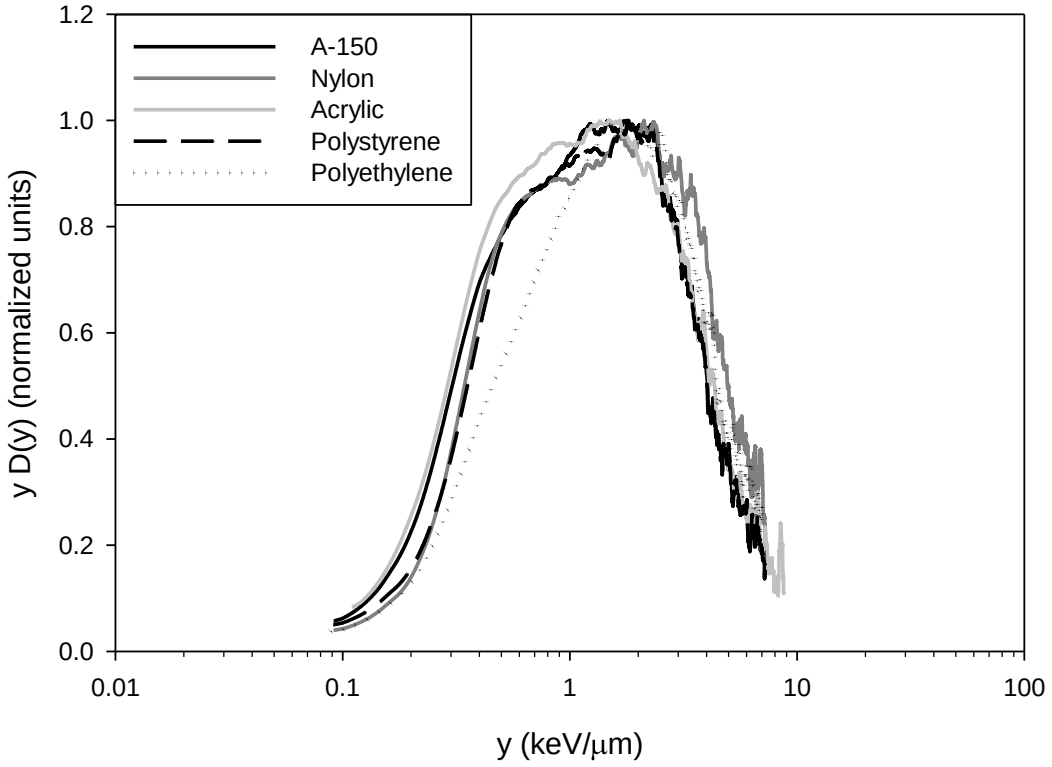


**Figure 42.** Lineal energy spectra taken with all five TEPCs for 222 MeV protons.

## 7.1. Protons – Simulation

The FLUKA simulated lineal energy spectra obtained for each of the five ionization wall materials for the 87, 162, and 222 MeV proton beams are shown in Figures 43, 45, and 47, respectively. Figures 44, 46, and 48 show the same spectra except that the plots have been offset by increments of 0.2 in order to show all five spectra clearly in a single plot. The simulated spectra are so similar that they cannot be distinguished from one another when plotted normally. The spectra for each plastic are entirely overlapping. The only difference that can be seen is between the ICRU muscle spectra and the other five spectra

at higher lineal energy. The ICRU muscle spectra have a slightly lower dose distribution in the 2-6 keV/μm region which is always to the right of the primary ionization peak.

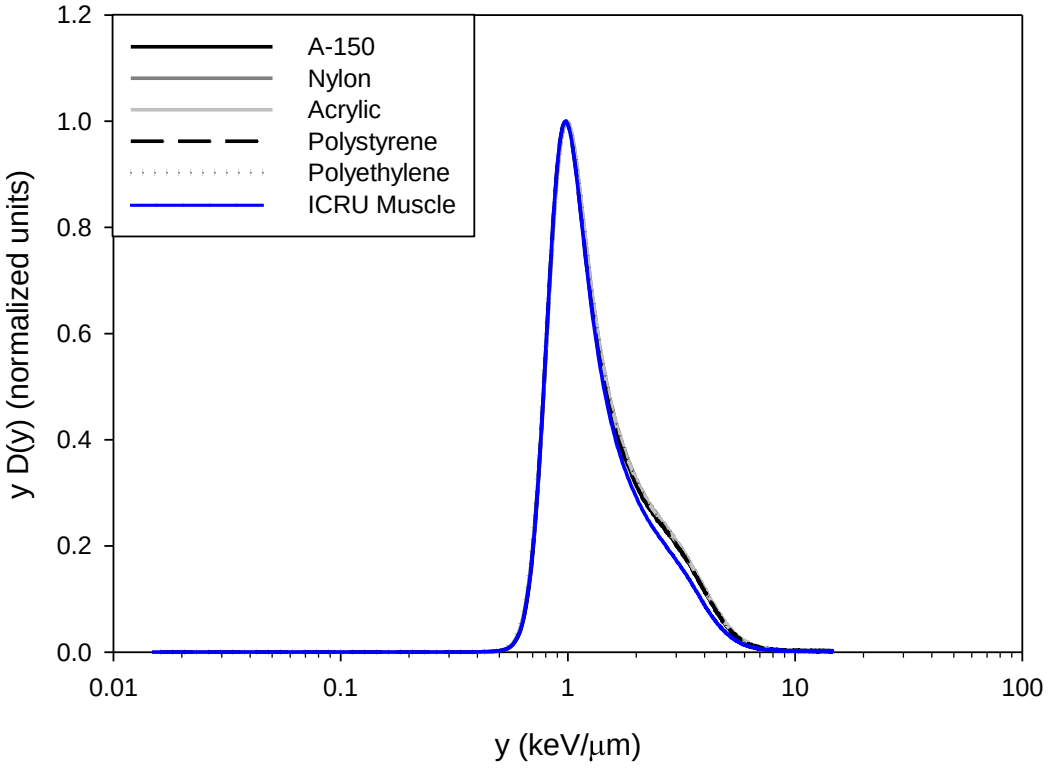


**Figure 43.** The FLUKA simulated spectra for all five ionization cavity materials as well as ICRU muscle for 87 MeV protons.

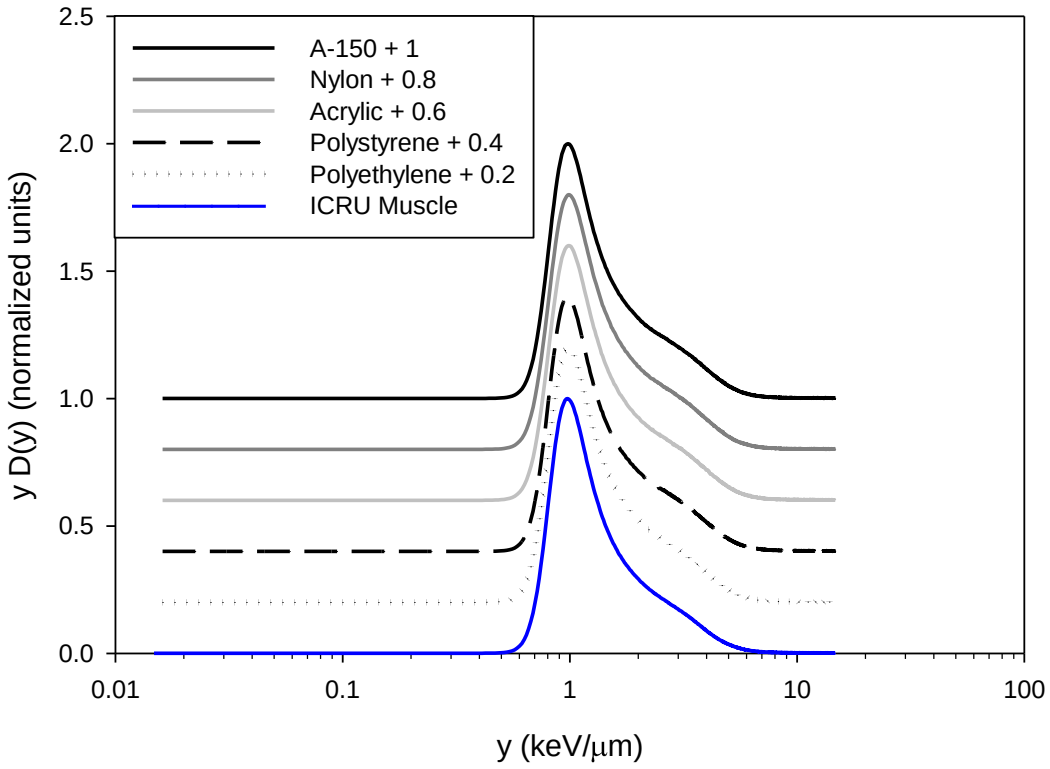


**Figure 44.** The FLUKA simulated spectra for all five ionization cavity materials as well as ICRU muscle for 87 MeV protons. The plots have shifted by increments of 0.2 for clarity.

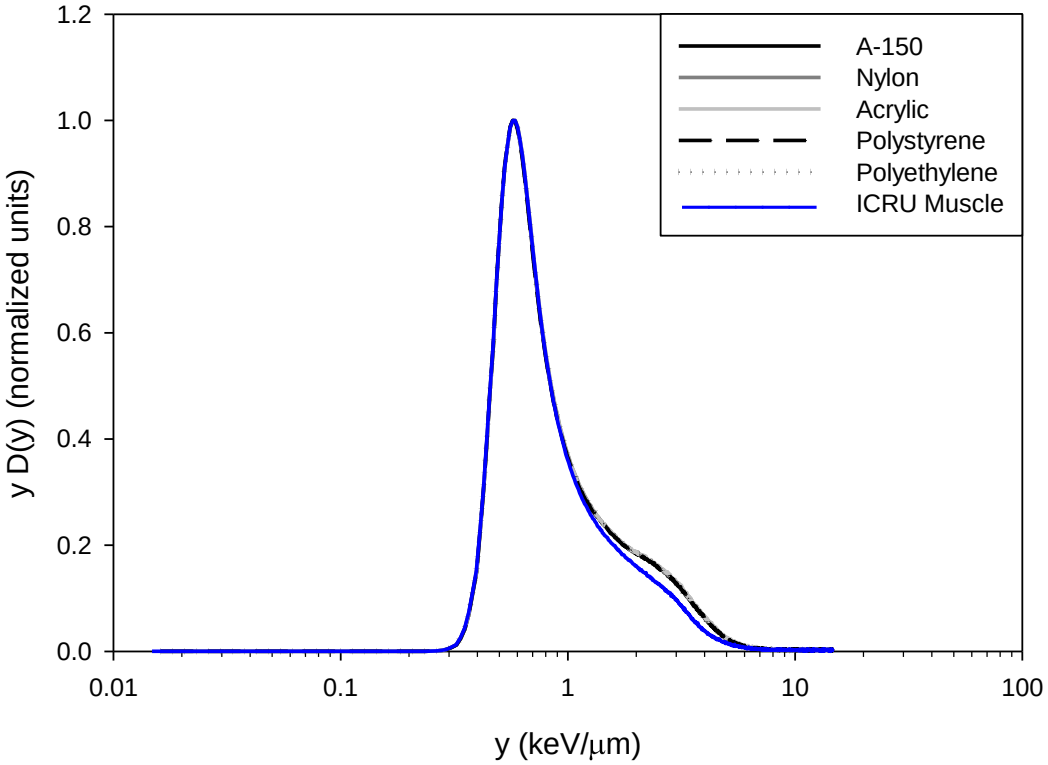


**Figure 45.** The FLUKA simulated spectra for all five ionization cavity materials as well as ICRU muscle for 162 MeV protons.

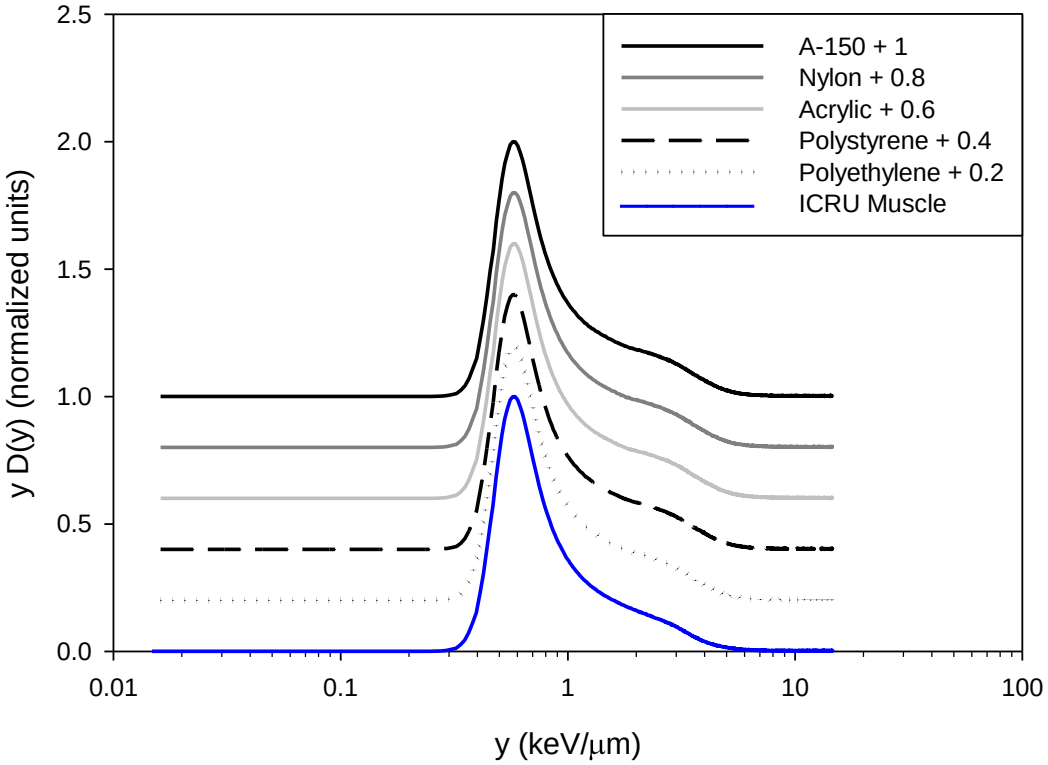


**Figure 46.** The FLUKA simulated spectra for all five ionization cavity materials as well as ICRU muscle for 162 MeV protons. The plots have shifted by increments of 0.2 for clarity.

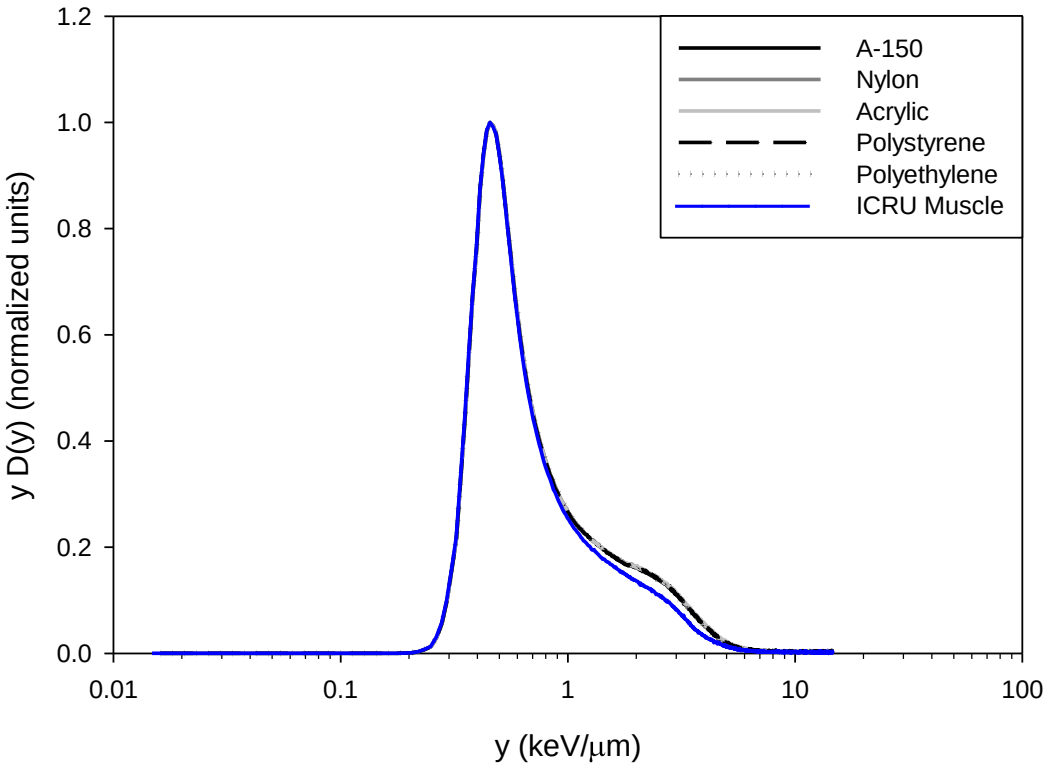


**Figure 47.** The FLUKA simulated spectra for all five ionization cavity materials as well as ICRU muscle for 222 MeV protons.

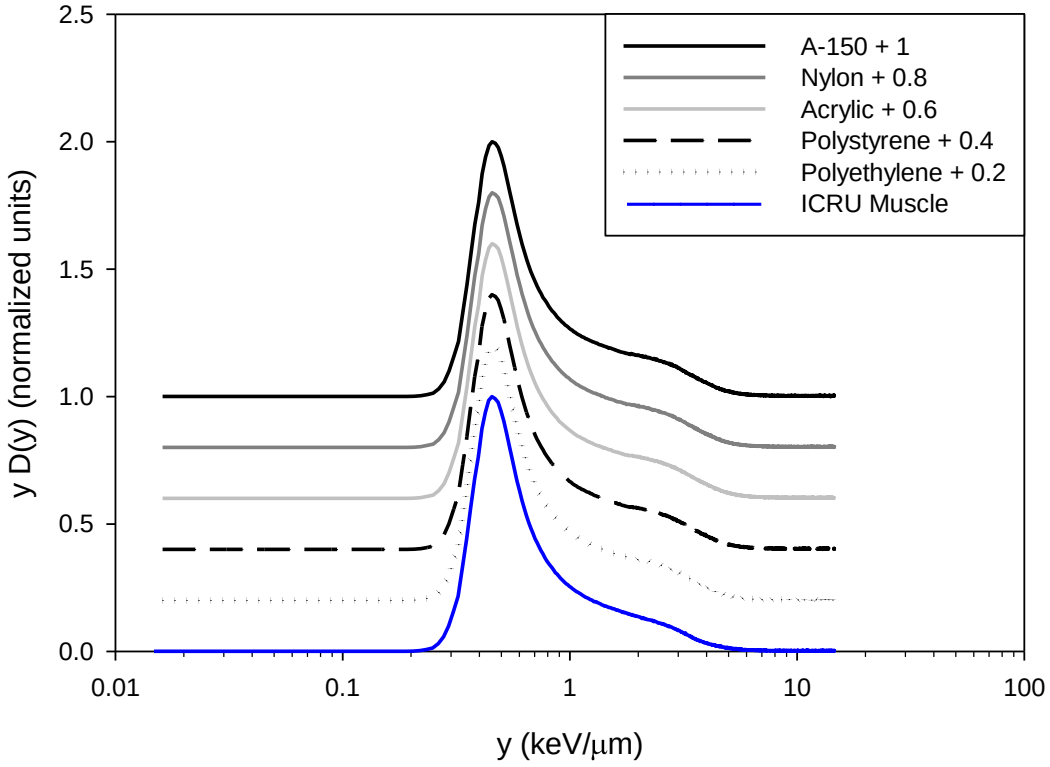


**Figure 48.** The FLUKA simulated spectra for all five ionization cavity materials as well as ICRU muscle for 222 MeV protons. The plots have shifted by increments of 0.2 for clarity.

7.2. Heavy Ions – Experiment

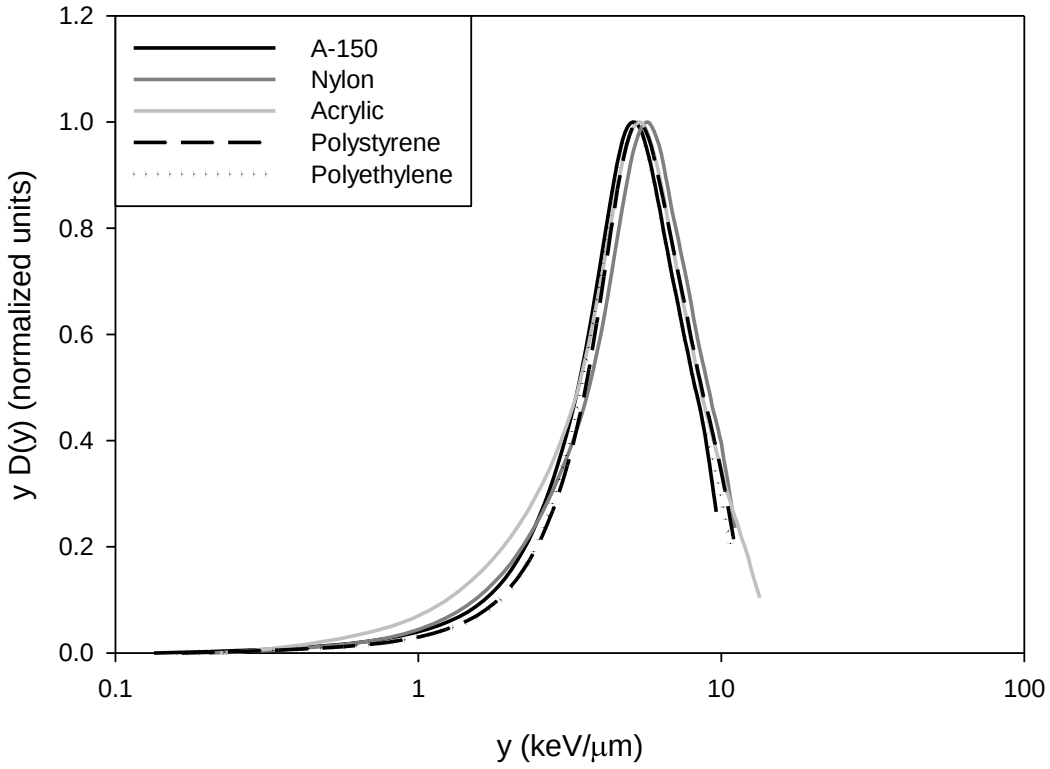


**Figure 49.** Lineal energy spectra taken with all five TEPCs for 143 MeV/amu helium ions.

The results of the heavy ion experiment are shown in Figures 49, 50, 51, 52, and 53 for the helium, carbon, silicon, argon, and iron beams, respectively. The spectra are very similar between the plastics for the lower LET beams. There is slightly more difference between the spectra for the higher LET beams such as silicon, argon, and iron. The differences are primarily seen on the rising edge of the lineal energy peak. The differences are mostly consistent for each heavy ion beam. Acrylic always has the highest rising edge followed closely by A-150 and polystyrene while the lowest rising

edges are typically seen in nylon and polyethylene. There are smaller differences seen between the peak positions of each spectra.

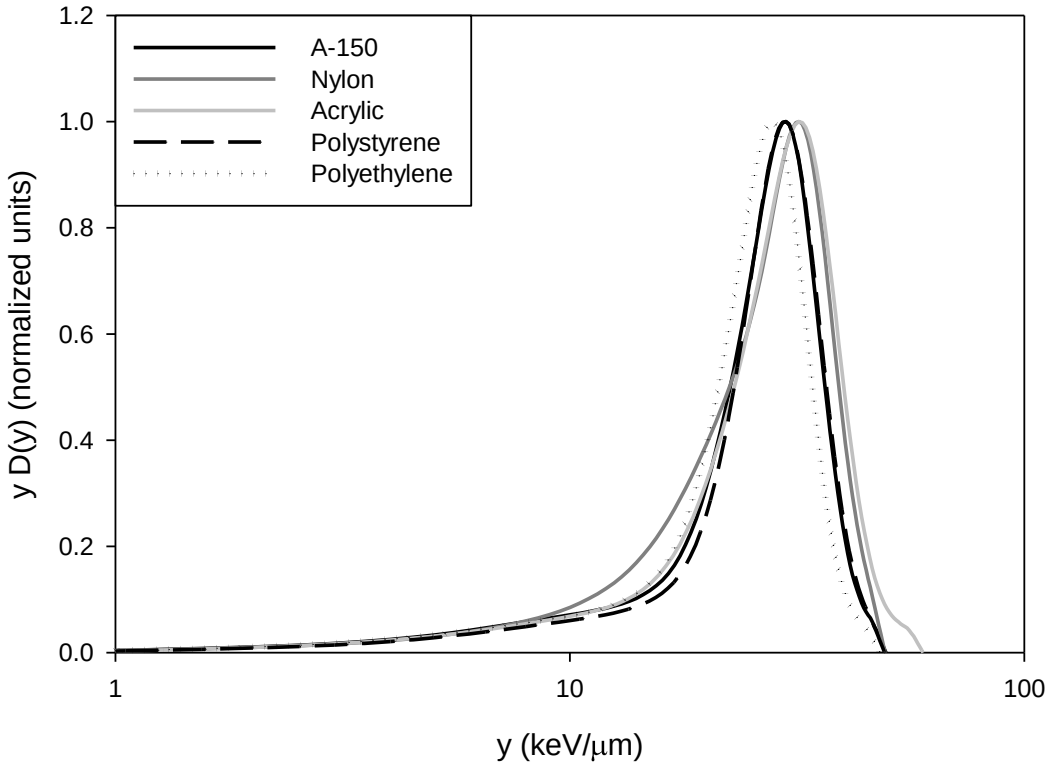


**Figure 50.** Lineal energy spectra taken with all five TEPCs for 265 MeV/amu carbon ions.

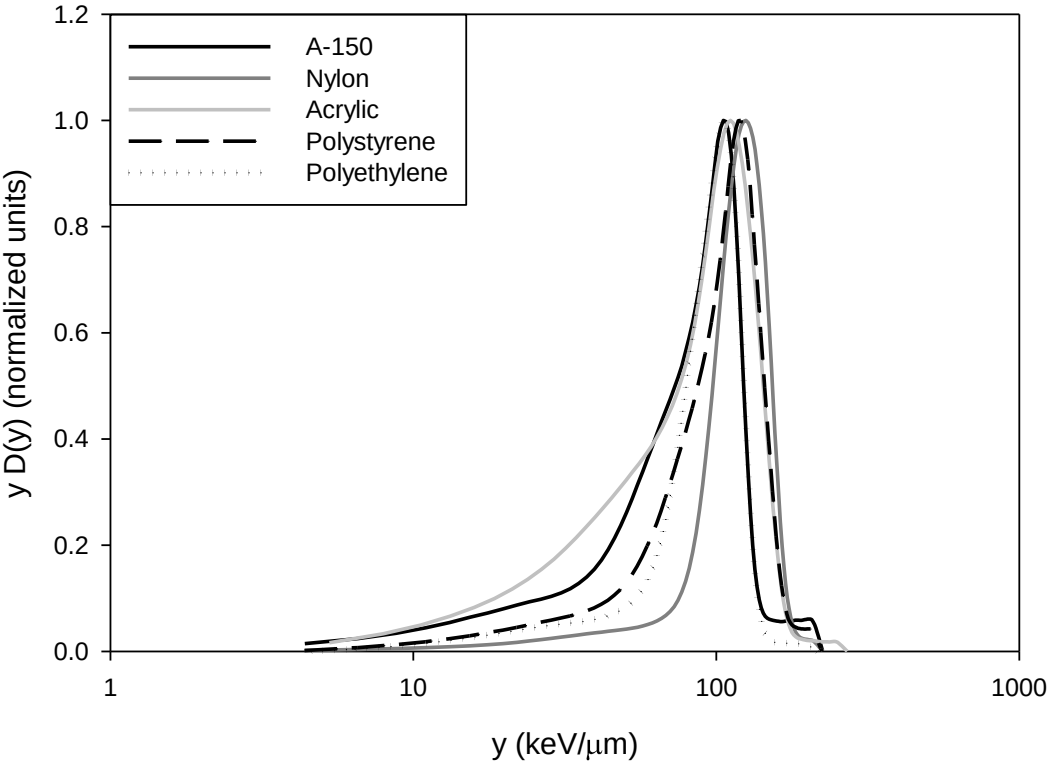


**Figure 51.** Lineal energy spectra taken with all five TEPCs for 440 MeV/amu silicon ions.

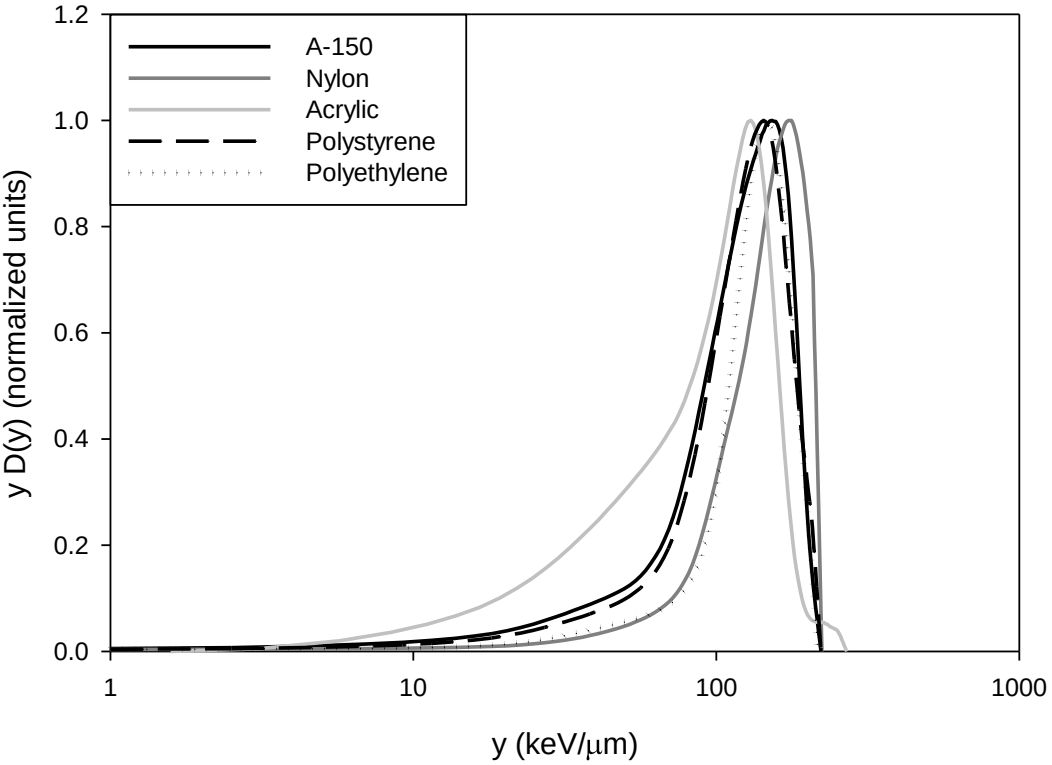


**Figure 52.** Lineal energy spectra taken with all five TEPCs for 430 MeV/amu argon ions.

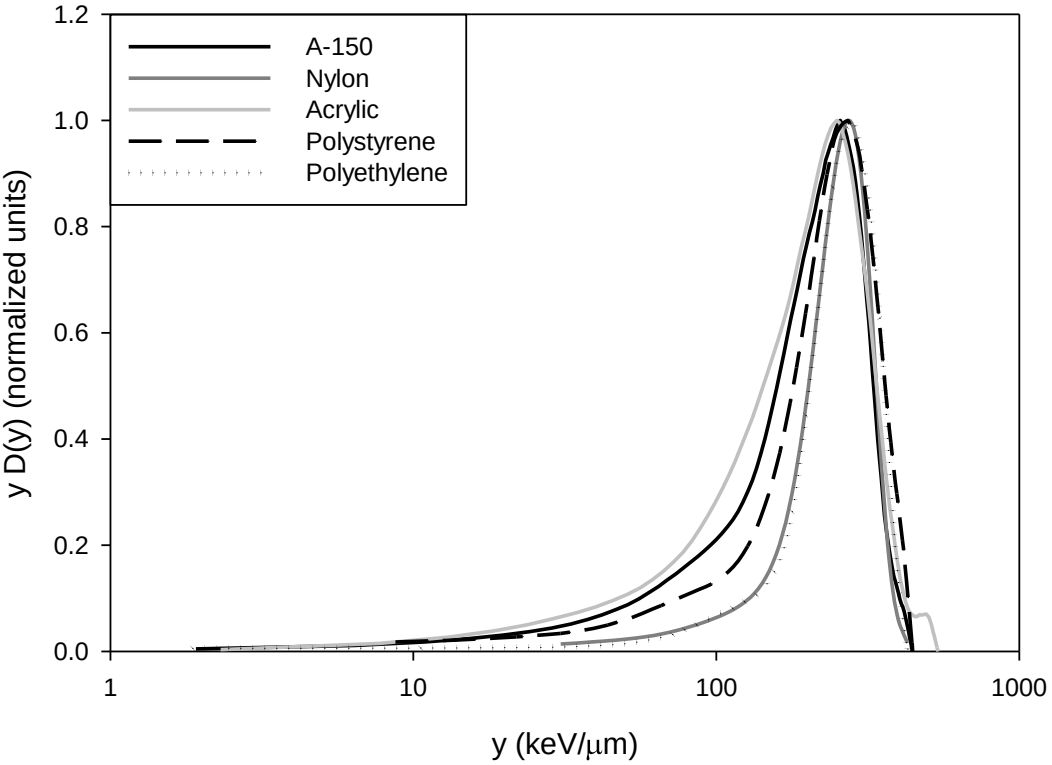


**Figure 53.** Lineal energy spectra taken with all five TEPCs for 421 MeV/amu iron ions.

7.3. Heavy Ions – Simulation

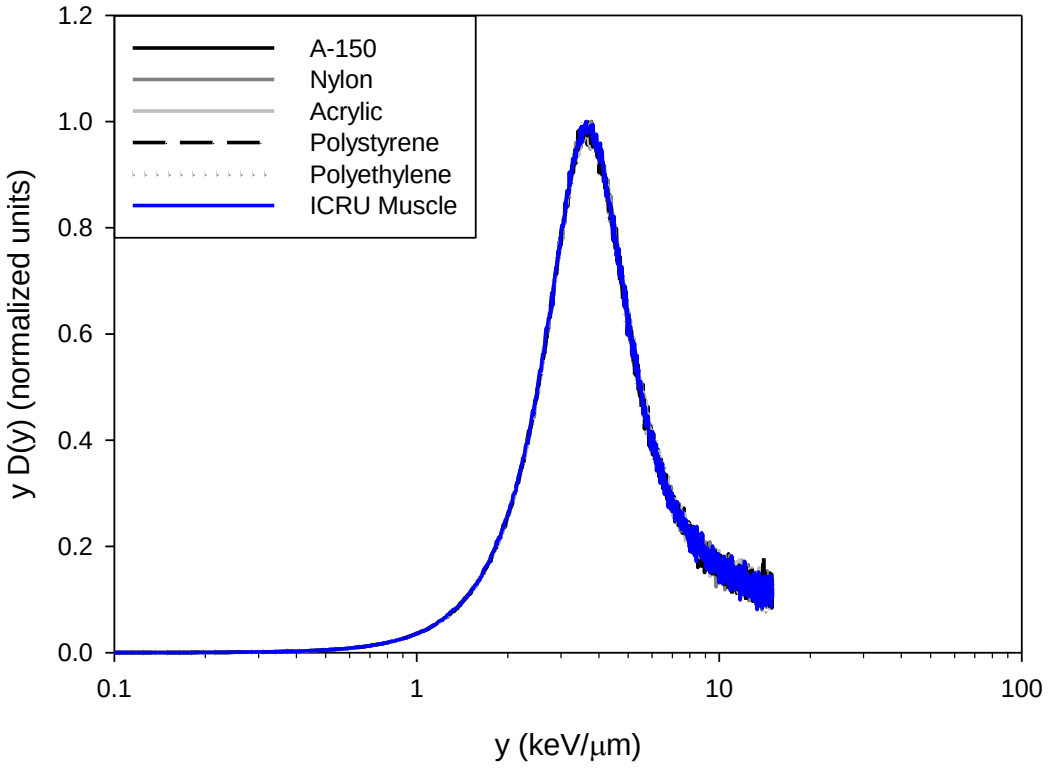


**Figure 54.** FLUKA simulated lineal energy spectra for all five ionization wall materials and ICRU muscle for 143 MeV/amu He.

The results of the FLUKA Monte Carlo code simulations are shown in Figures 54-58 for the helium, carbon, silicon, argon and iron beams, respectively. The simulated spectra for each material are nearly identical to the spectra of the other materials including ICRU muscle. The spectra are almost entirely overlapping and show no dependence on the type of material simulated.

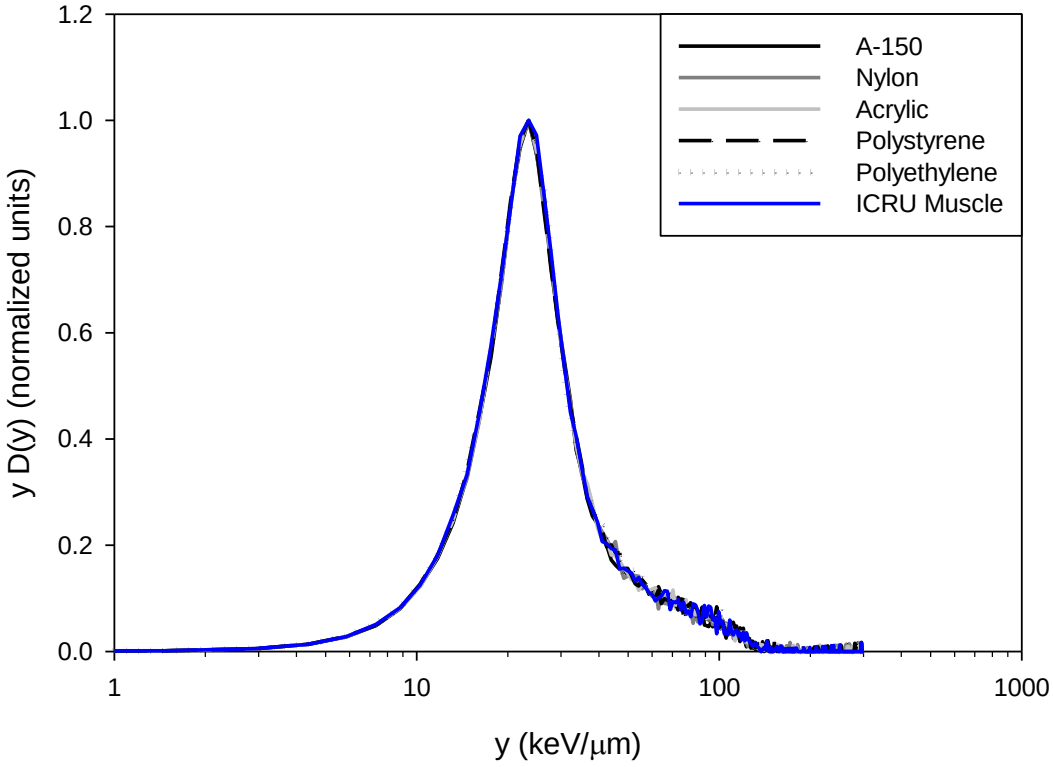


**Figure 55.** FLUKA simulated lineal energy spectra for all five ionization wall materials and ICRU muscle for 265 MeV/amu C.

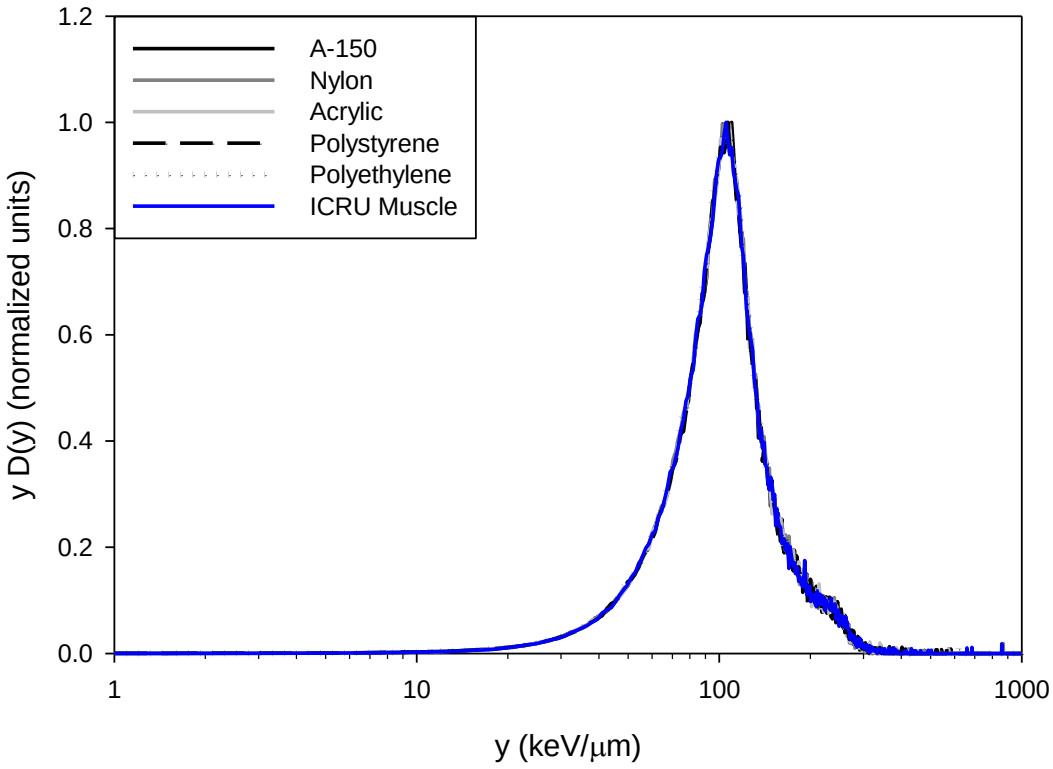


**Figure 56.** FLUKA simulated lineal energy spectra for all five ionization wall materials and ICRU muscle for 440 MeV/amu Si.

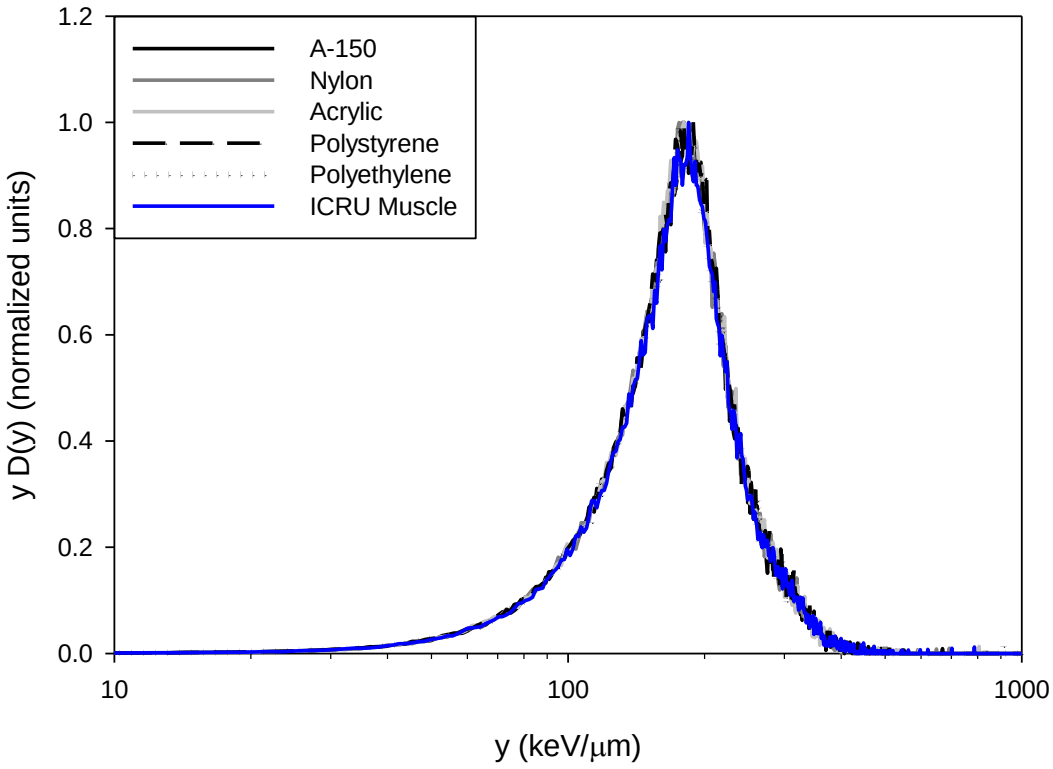


**Figure 57.** FLUKA simulated lineal energy spectra for all five ionization wall materials and ICRU muscle for 430 MeV/amu Ar.

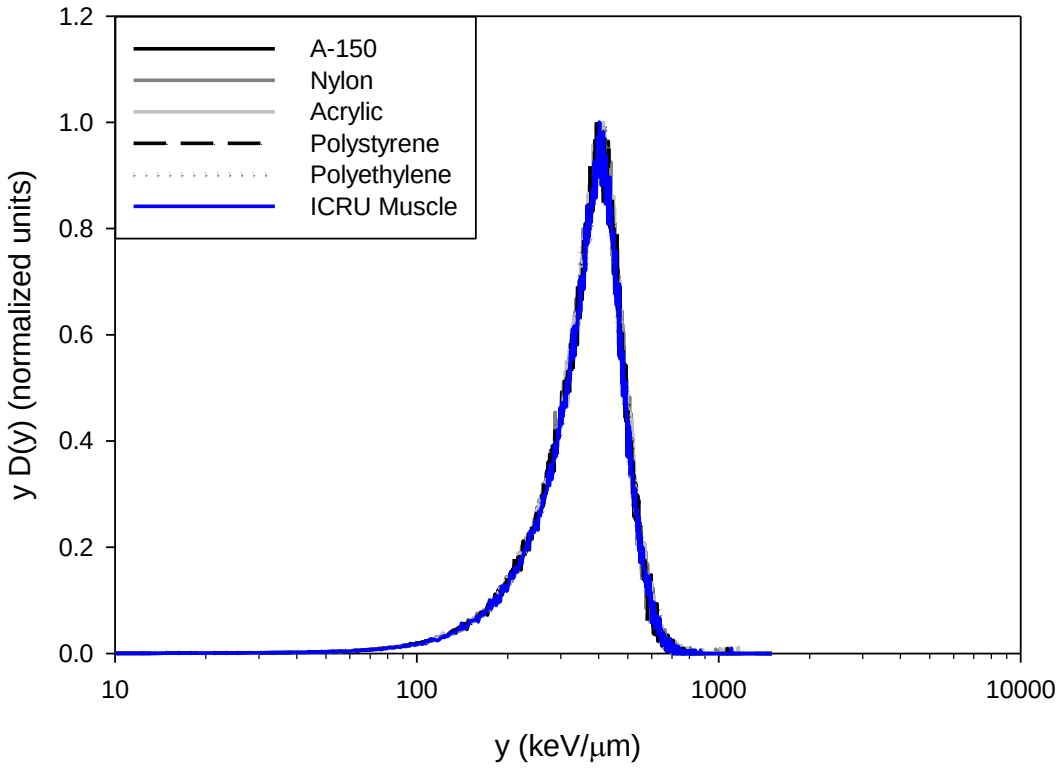


**Figure 58.** FLUKA simulated lineal energy spectra for all five ionization wall materials and ICRU muscle for 421 MeV/amu Fe.

## 7.4. Comparison Between Experiment and Simulation

Comparisons between the simulated and measured spectra for the A-150 TEPC for proton energies of 87 MeV, 162 MeV, and 222 MeV are shown are Figures 59, 60, and 61, respectively. The comparisons between the simulated and measured spectra for the heavy ion beams are shown in Figures 62-66. The figures also show the theoretical spectra determined for a sphere of gas with no wall material using the continuous slowing down approximation and based on the chord length distribution of the sphere (Rossi, 1968). The theoretical spectra have sharp peaks corresponding to events where the

protons cross the full diameter of the sphere. The theoretical spectra as discussed in Chapter IV are simply a triangular distribution but appear as a sharp peak when plottted as a dose distribution in log scale. Any events above that peak in the experimental or simulated spectra come from secondaries generated in the wall of the detector (Gersey et al., 2002) or primary particles of higher LET in the beam.

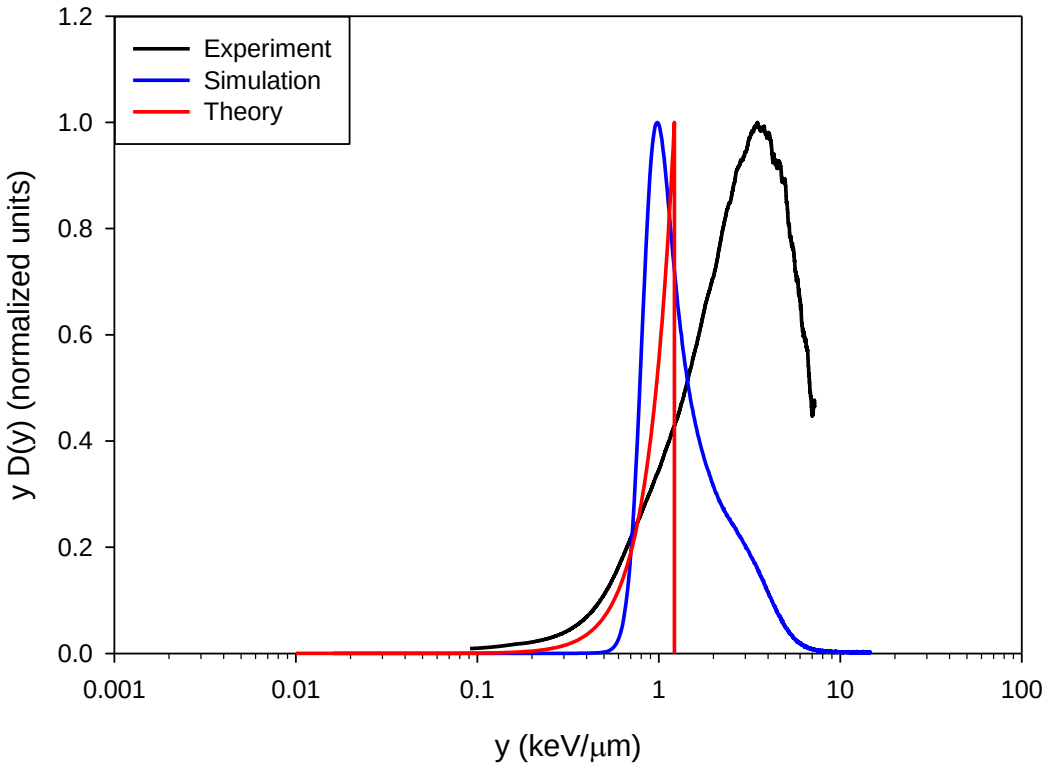


**Figure 59.** The experimental, FLUKA simulated, and theoretical spectra for the A-150 TEPC for 87 MeV protons.

The experimental spectra are generally broader with respect to the FLUKA simulated spectra especially for the lower lineal energy spectra. There are several reasons contributing to this fact. One reason for this is that the simulations are done assuming an ideal monoenergetic beam while the actual proton beam has some natural energy spread.

This energy spread in the primary beam also affects the energy spread in secondary particles generated in the wall of the detector. The overall result is that the spectrum becomes much broader when compared to the ideal case.

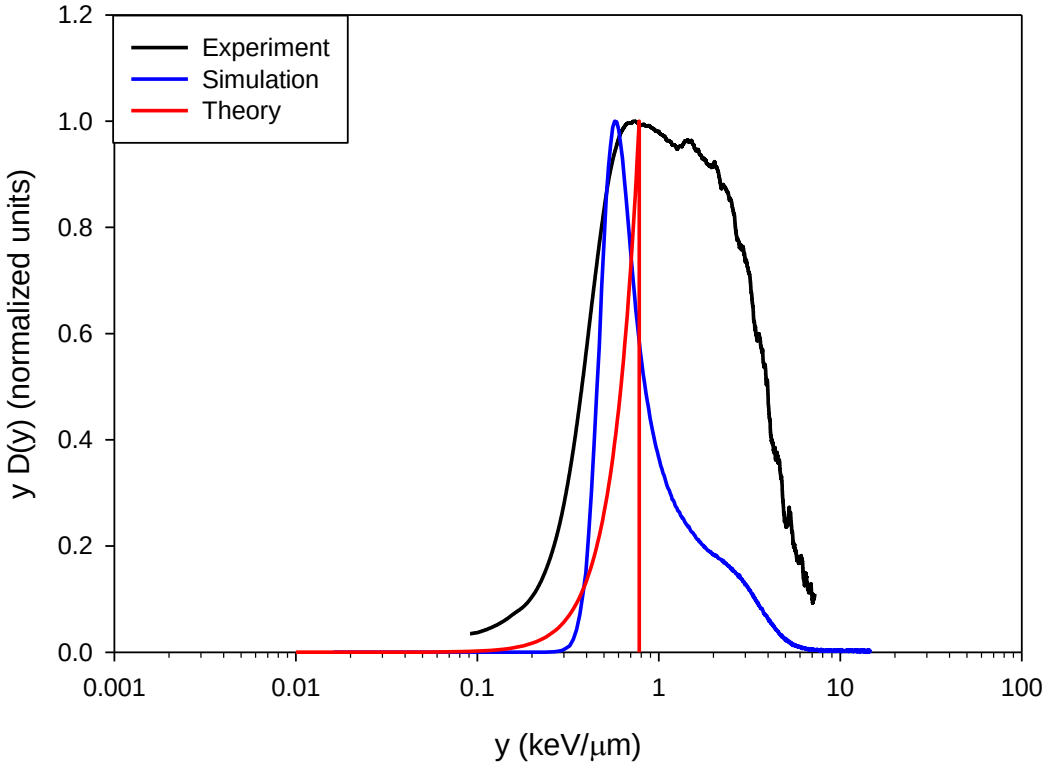


**Figure 60.** The experimental, FLUKA simulated, and theoretical spectra for the A-150 TEPC for 162 MeV protons.

Another reason that simulation and experiment do not match more closely is that the simulation assumes perfect efficiency in the detector so that every ion pair created in the sensitive volume of the detector is counted. In reality the efficiency of the detector is not 100%. Recombination can still occur especially due to nonuniformity in the electric field of the detector. This may cause some particles with different impact parameters to be counted with different efficiencies. In this simulation the snout and other upstream

elements that may be in the beam were also not simulated. Any secondary particles such as neutrons created in these elements would not contribute to the simulation spectra but would be seen in the experimental spectra.

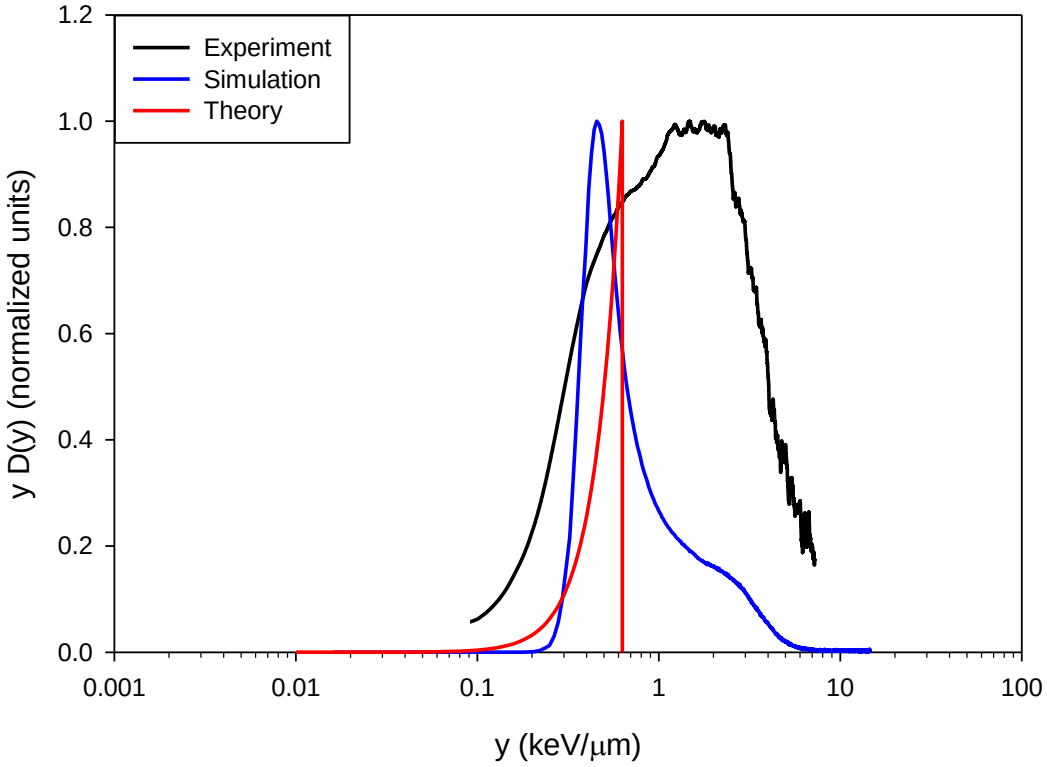


**Figure 61.** The experimental, FLUKA simulated, and theoretical spectra for the A-150 TEPC for 222 MeV protons.

The purpose of simulation for this study was not to reproduce the exact radiation environment as the experiment but to create a simplified ideal case where only one variable, the ionization chamber wall material, was changed between simulations. The comparison between experimental, simulated, and theoretical spectra is shown here to illustrate the similarities between the peak positions of the spectra and show the overall differences between the shapes of the spectra.

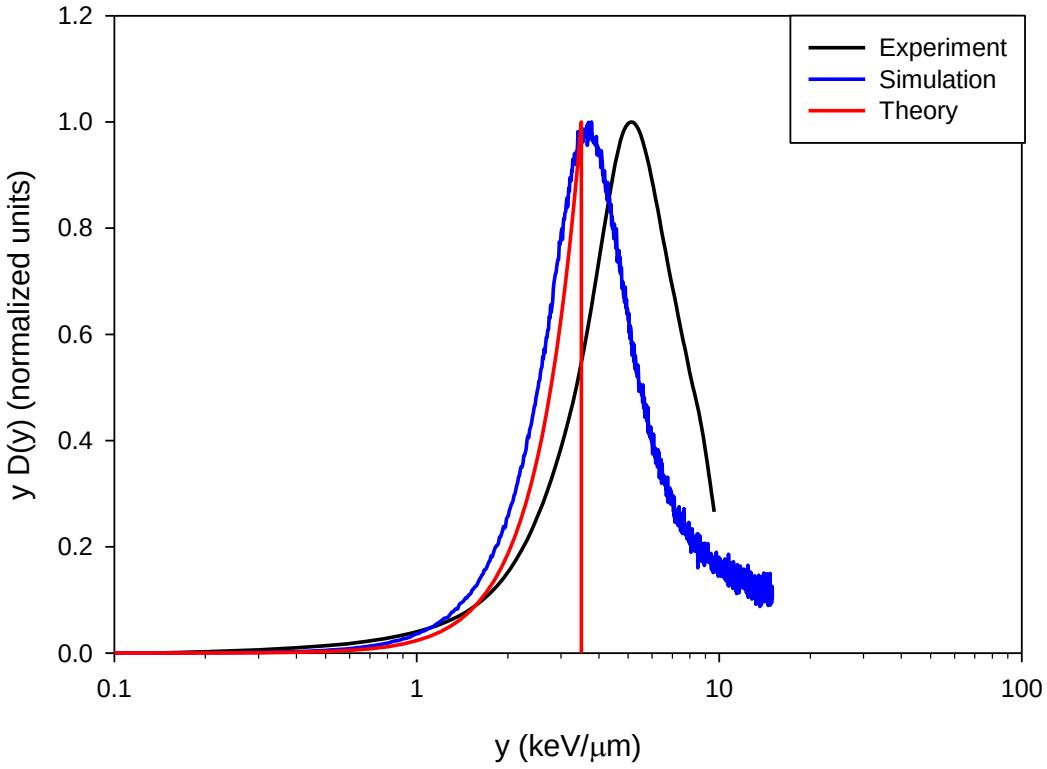


**Figure 62.** The experimental, FLUKA simulated, and theoretical spectra for the A-150 TEPC for 143 MeV/amu He.

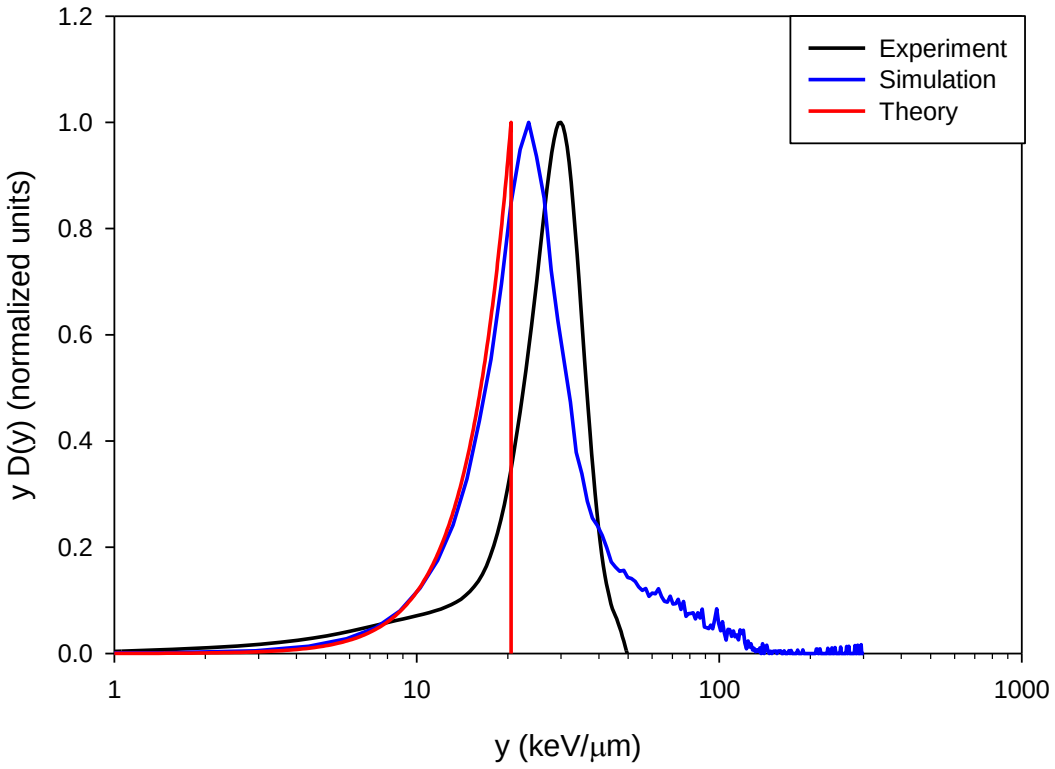


**Figure 63.** The experimental, FLUKA simulated, and theoretical spectra for the A-150 TEPC for 265 MeV/amu C.

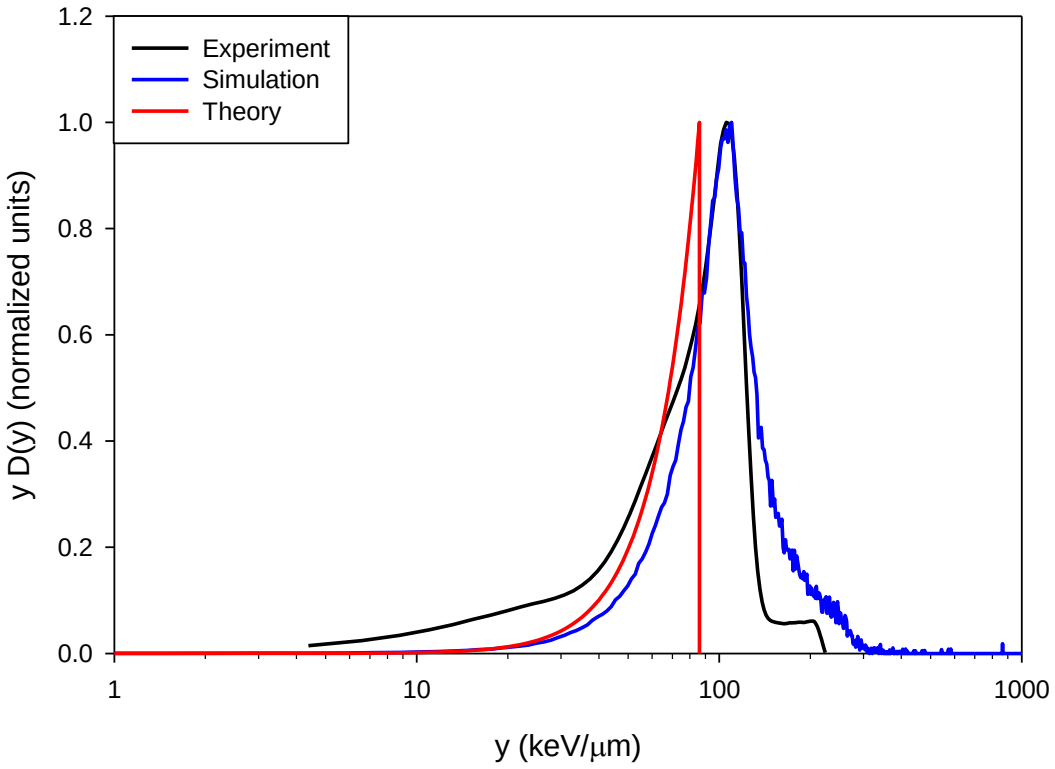


**Figure 64.** The experimental, FLUKA simulated, and theoretical spectra for the A-150 TEPC for 440 MeV/amu Si.

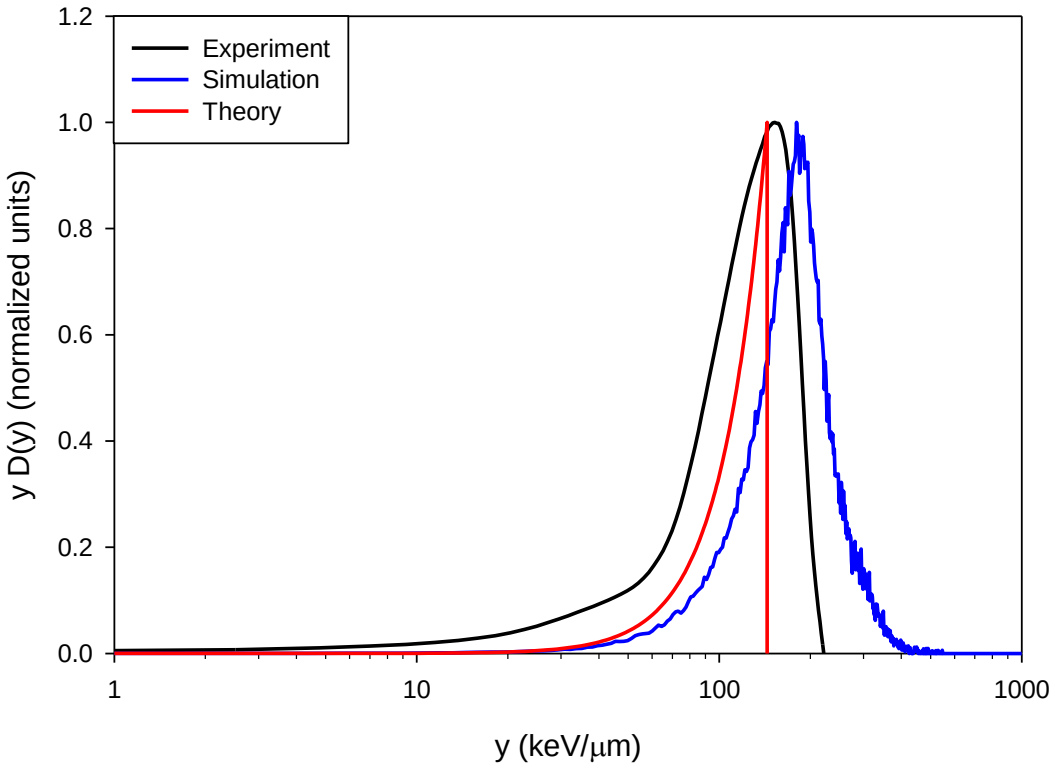


**Figure 65.** The experimental, FLUKA simulated, and theoretical spectra for the A-150 TEPC for 430 MeV/amu Ar.

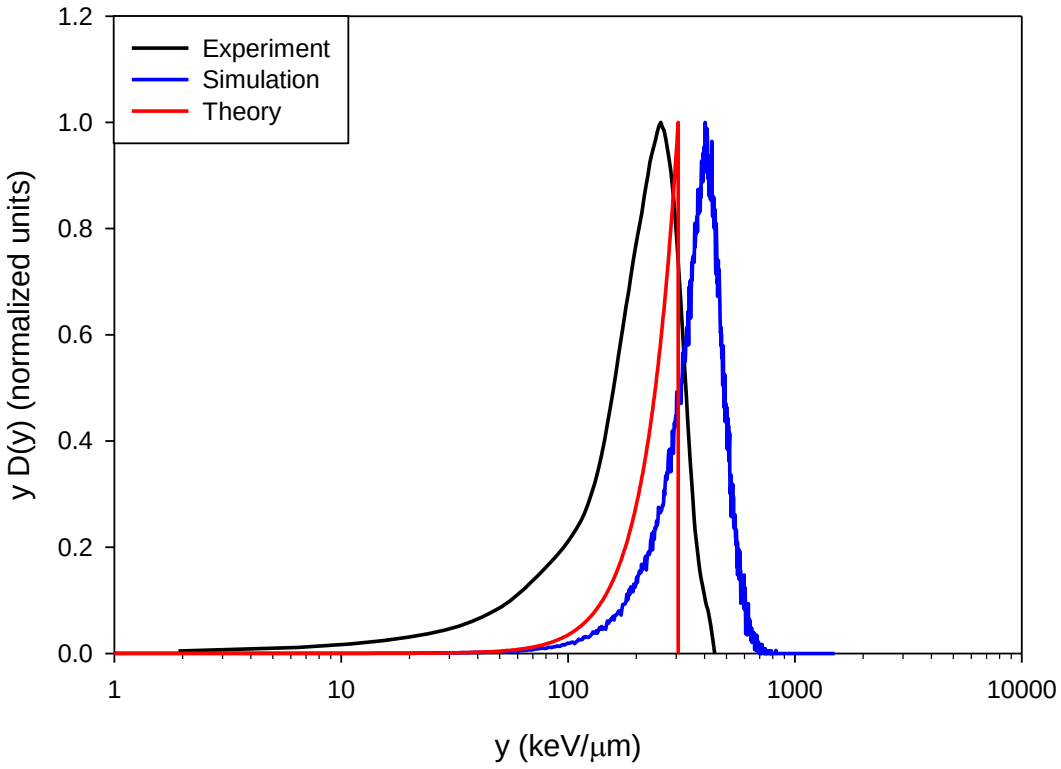


**Figure 66.** The experimental, FLUKA simulated, and theoretical spectra for the A-150 TEPC for 421 MeV/amu Fe.

7.5. Average Lineal Energy Comparison

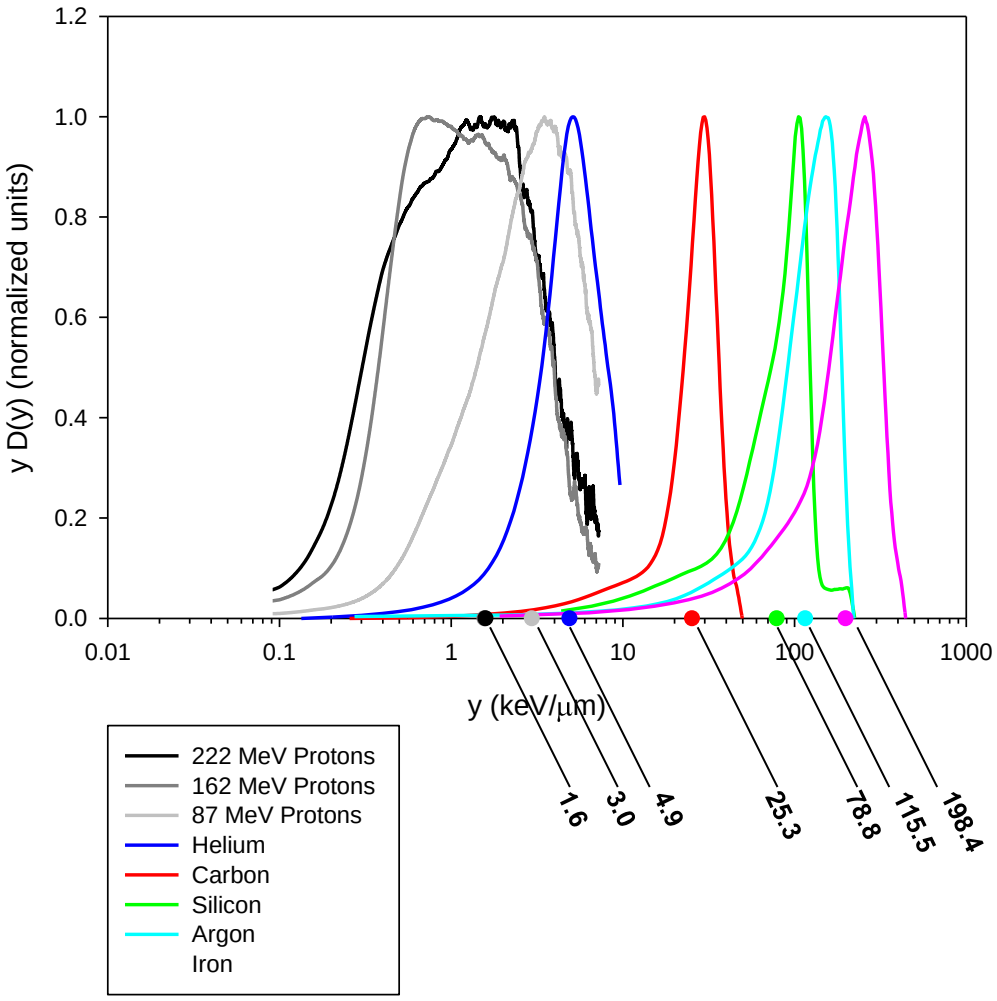


**Figure 67.** All of the lineal energy spectra measured with the A-150 TEPC and their corresponding dose-averaged lineal energies

To further quantify the response of each ionization cavity wall material, the average lineal energy values of each spectrum were measured as shown in Figure 67. As shown in equation ( 51 ) and ( 52 ), the frequency-averaged and dose-averaged lineal energies are integrals over the entire lineal energy range from zero to infinity. In actuality, the detector has a finite lineal energy range.

**Table 5.** The frequency-averaged and dose-averaged lineal energies for experiment, simulation, and theory for every beam used in this study (keV/μm).

Experiment

| | 222 MeV H | | 162 MeV H | | 87 MeV H | | He | | C | | Si | | Ar | | Fe | |
|---|---|---|---|---|---|---|---|---|---|---|---|---|---|---|---|---|
| | $y_f$ | $y_D$ | $y_f$ | $y_D$ | $y_f$ | $y_D$ | $y_f$ | $y_D$ | $y_f$ | $y_D$ | $y_f$ | $y_D$ | $y_f$ | $y_D$ | $y_f$ | $y_D$ |
| A-150 | 0.69 | 1.59 | 0.77 | 1.57 | 1.60 | 2.95 | 3.48 | 4.89 | 14.9 | 25.3 | 49.5 | 78.8 | 59.8 | 115.5 | 123.7 | 198.4 |
| Nylon | 0.78 | 1.81 | 0.89 | 1.92 | 1.80 | 3.26 | 3.79 | 5.34 | 15.3 | 25.8 | 88.5 | 113.1 | 84.4 | 141.8 | 195.6 | 239.8 |
| Acrylic | 0.71 | 1.65 | 0.78 | 1.63 | 1.50 | 2.85 | 3.38 | 5.21 | 16.1 | 27.4 | 50.7 | 81.9 | 43.7 | 91.0 | 117.0 | 195.7 |
| Polystyrene | 0.72 | 1.63 | 0.84 | 1.75 | 1.33 | 2.54 | 3.94 | 5.36 | 15.4 | 26.1 | 67.5 | 96.9 | 63.9 | 118.4 | 139.4 | 222.2 |
| Polyethylene | 0.82 | 1.83 | 0.82 | 1.72 | 1.62 | 2.97 | 3.84 | 5.20 | 14.2 | 24.0 | 65.1 | 88.1 | 73.1 | 129.1 | 192.8 | 249.1 |

Simulation

| | 222 MeV H | | 162 MeV H | | 87 MeV H | | He | | C | | Si | | Ar | | Fe | |
|---|---|---|---|---|---|---|---|---|---|---|---|---|---|---|---|---|
| | $y_f$ | $y_D$ | $y_f$ | $y_D$ | $y_f$ | $y_D$ | $y_f$ | $y_D$ | $y_f$ | $y_D$ | $y_f$ | $y_D$ | $y_f$ | $y_D$ | $y_f$ | $y_D$ |
| A-150 | 0.61 | 0.94 | 0.76 | 1.09 | 1.24 | 1.58 | 3.32 | 4.46 | 19.8 | 28.6 | 81.3 | 105.8 | 135.6 | 172.5 | 286.6 | 362.0 |
| Nylon | 0.61 | 0.94 | 0.76 | 1.09 | 1.25 | 1.58 | 3.31 | 4.46 | 19.8 | 28.2 | 81.3 | 105.7 | 135.4 | 172.5 | 286.8 | 361.8 |
| Acrylic | 0.61 | 0.94 | 0.76 | 1.09 | 1.24 | 1.59 | 3.32 | 4.47 | 19.9 | 28.7 | 81.3 | 105.7 | 136.0 | 172.9 | 286.8 | 362.0 |
| Polystyrene | 0.61 | 0.94 | 0.76 | 1.09 | 1.24 | 1.58 | 3.31 | 4.46 | 19.9 | 28.7 | 81.2 | 105.6 | 135.8 | 172.9 | 286.9 | 361.6 |
| Polyethylene | 0.61 | 0.93 | 0.75 | 1.08 | 1.24 | 1.57 | 3.31 | 4.45 | 19.8 | 28.3 | 81.5 | 105.9 | 136.0 | 172.9 | 287.9 | 361.7 |
| ICRU Muscle | 0.59 | 0.87 | 0.73 | 1.01 | 1.21 | 1.51 | 3.31 | 4.45 | 19.8 | 28.6 | 81.6 | 105.8 | 136.1 | 172.7 | 288.2 | 361.9 |

Theory

| 222 MeV H | | 162 MeV H | | 87 MeV H | | He | | C | | Si | | Ar | | Fe | |
|---|---|---|---|---|---|---|---|---|---|---|---|---|---|---|---|
| $y_f$ | $y_D$ | $y_f$ | $y_D$ | $y_f$ | $y_D$ | $y_f$ | $y_D$ | $y_f$ | $y_D$ | $y_f$ | $y_D$ | $y_f$ | $y_D$ | $y_f$ | $y_D$ |
| 0.42 | 0.47 | 0.52 | 0.59 | 0.81 | 0.91 | 2.30 | 2.59 | 13.7 | 15.4 | 57.4 | 64.6 | 96.0 | 108.0 | 203.9 | 229.4 |

The upper lineal energy limit is determined by the gas gain of the detector and electronic gain of the amplifier. The lower limit is determined by the noise threshold of the detector. Electronic noise is present primarily at the lowest lineal energy channels. An appropriate minimum cutoff threshold must be chosen above which no noise is measured in the detector. The cutoff for these detectors, for an amplifier gain of 300, was ~0.07 keV/μm. Any actual energy depositions in the detector of lower lineal energy will not be included in the frequency-averaged lineal energy and this will lead to the measured value of frequency-averaged lineal energy being higher than the actual average LET.

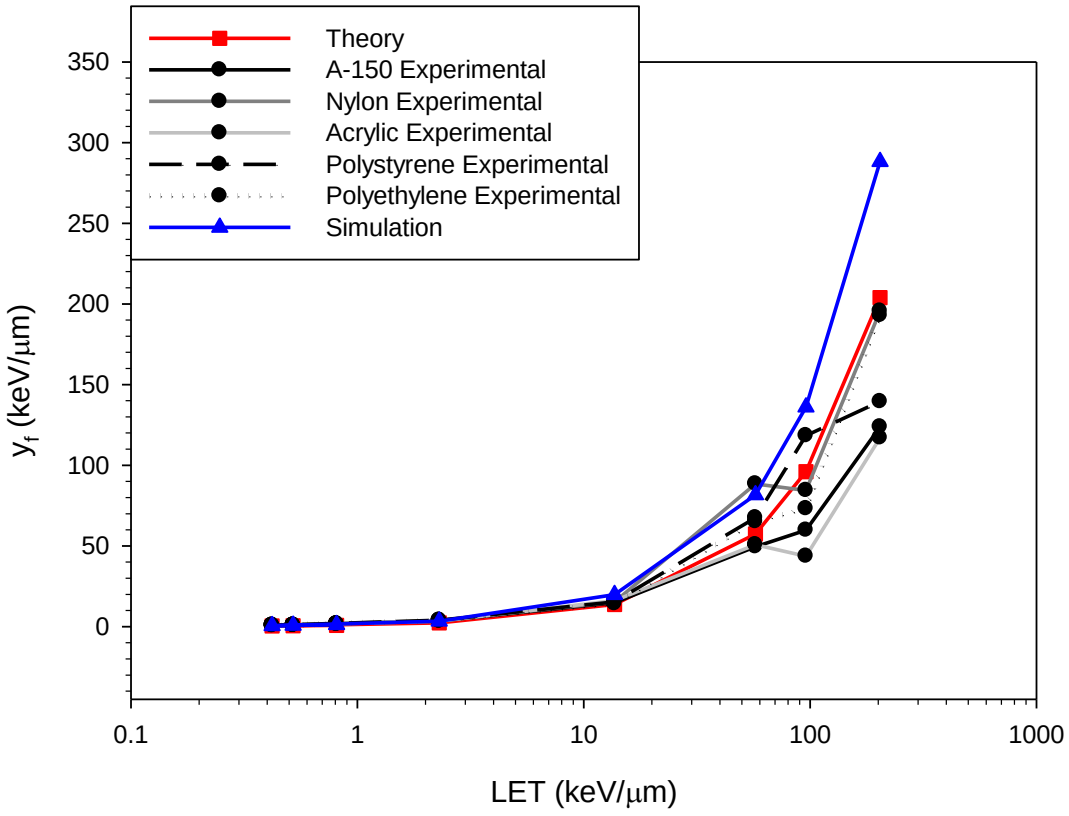


**Figure 68.** The frequency-averaged lineal energies for experiment, simulation, and theory for every beam used in this study shown with the ordinate in a linear scale.

This effect can be compensated for by various methods of extrapolation to extend the data to zero. Different extrapolation methods may lower $\bar{y}_F$ by as much as 30% (Varma, 1982). However, any method used on this data should have a similar effect across all the measured spectra. Since the purpose of this study is to compare the responses of the different plastics, no extrapolation method has been used for the data in Table 5. The frequency-averaged lineal energies are plotted in a linear scale and a log scale in Figure 68 and Figure 69, respectively. The dose-averaged lineal energies are plotted in a linear scale and a log scale in Figure 70 and Figure 71, respectively.

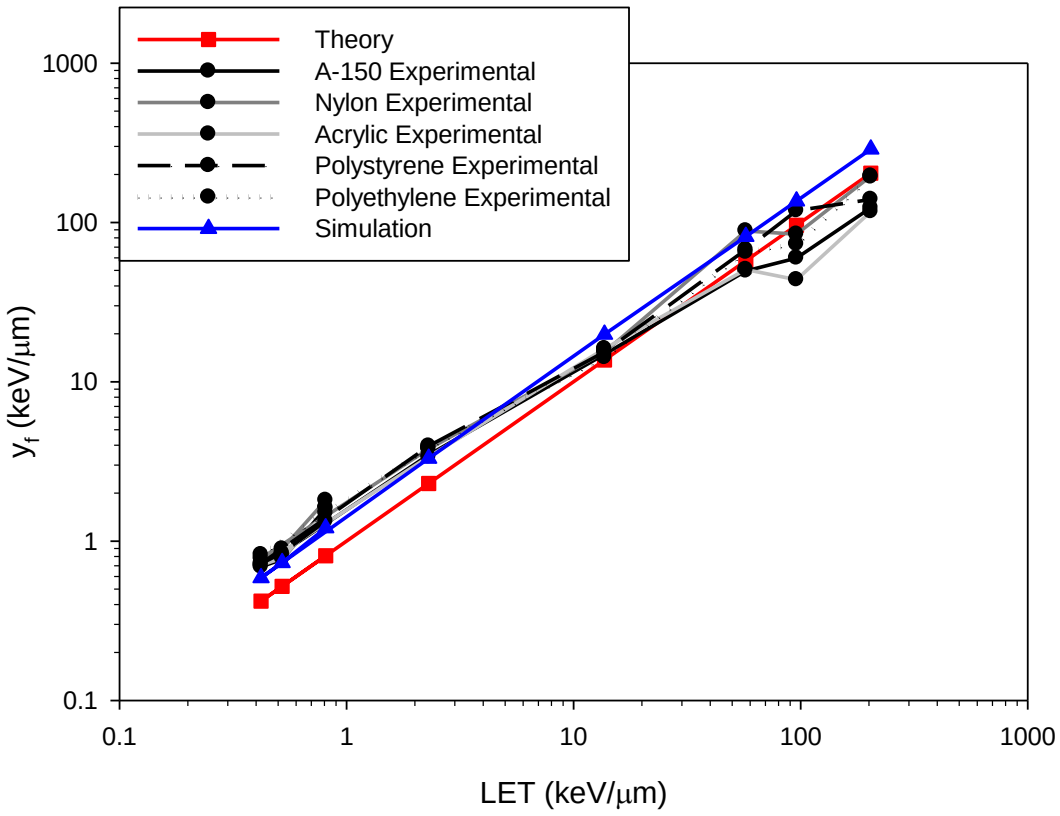


**Figure 69.** The frequency-averaged lineal energies for experiment, simulation, and theory for every beam used in this study shown with the ordinate in a log scale.

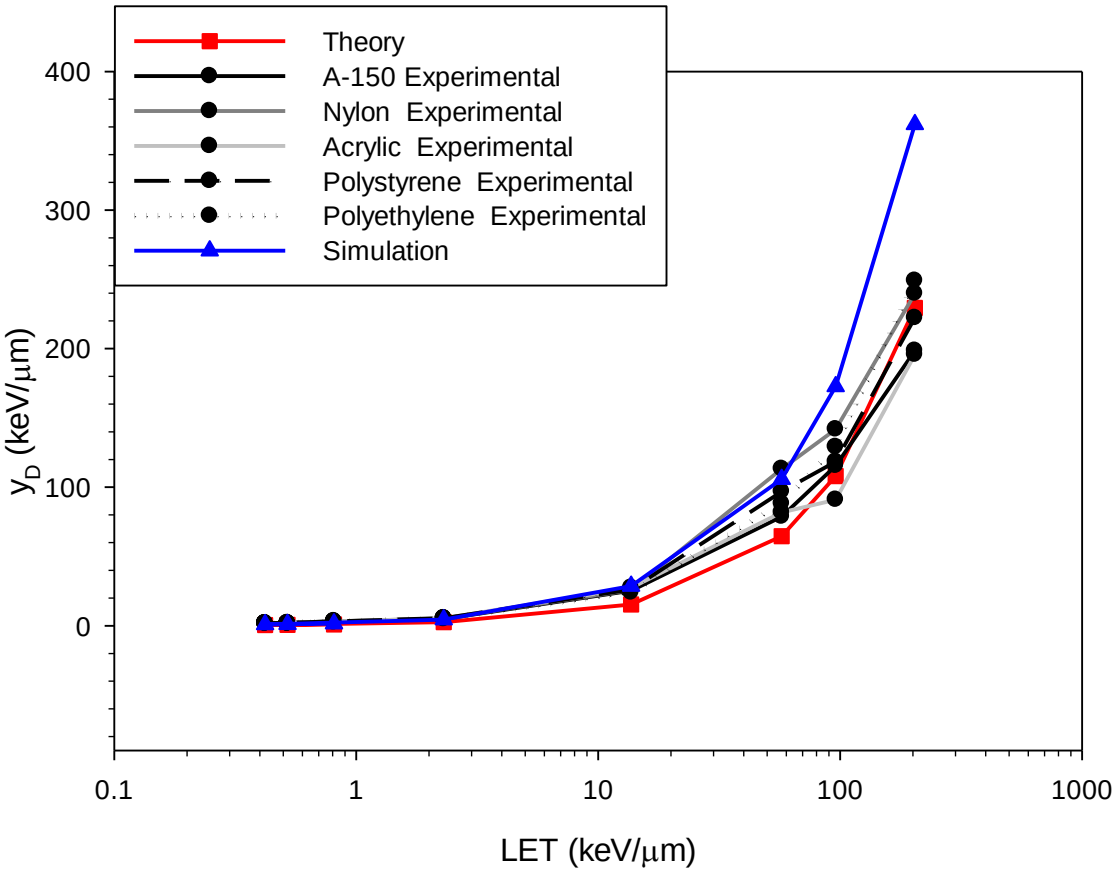


**Figure 70.** The dose-averaged lineal energies for experiment, simulation, and theory for every beam used in this study shown with the ordinate in a linear scale.

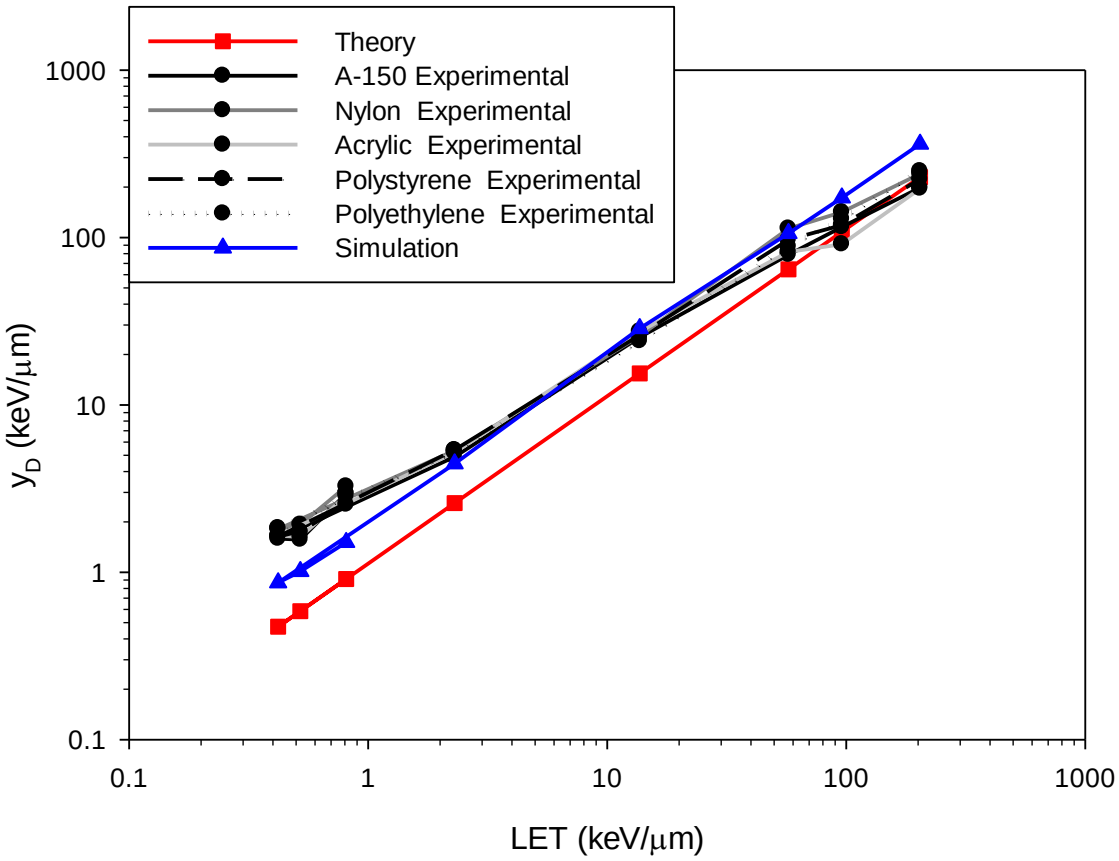


**Figure 71.** The dose-averaged lineal energies for experiment, simulation, and theory for every beam used in this study shown with the ordinate in a log scale.

# CHAPTER VIII

# FLIGHT VERSION DEVELOPMENT

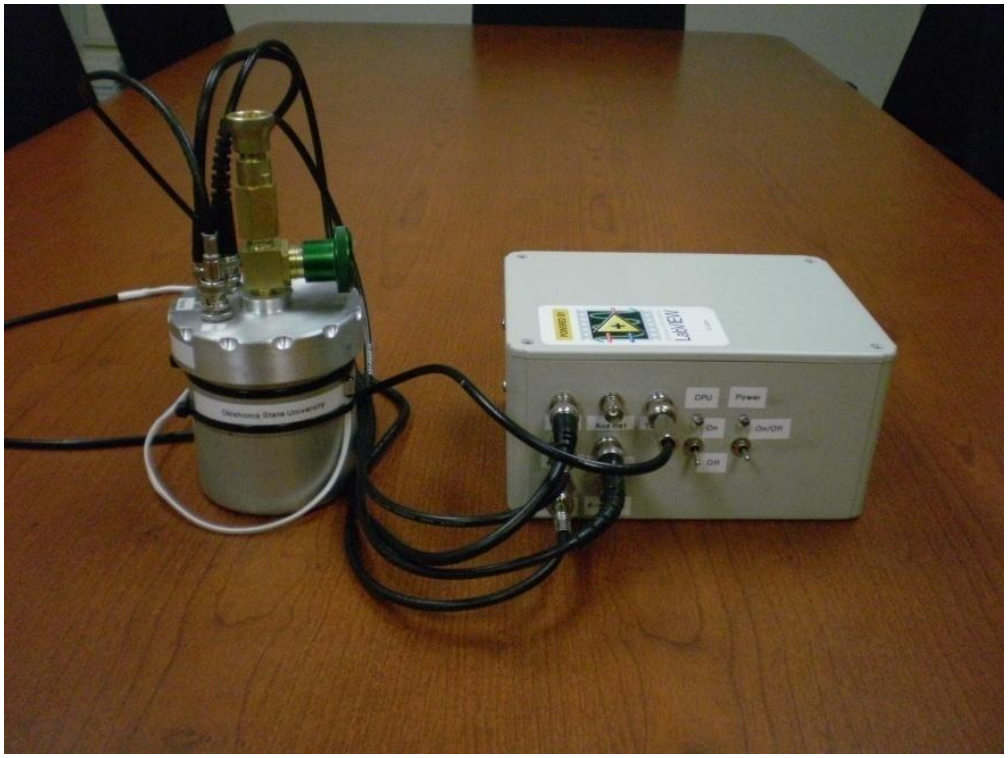


**Figure 72.** The flight version TEPC connected to the computer box. The box contains the CPU, power supply, battery, high voltage power supply, linear amplifier, and multichannel analyzer.

A flight version of the TEPC has been developed for a balloon flight or other high altitude flight. The flight version, shown in Figure 72 is completely self-dependent and includes the following components:

- CPU (Diamond Systems – Athena II)
- Battery (Tri-M Engineering – BAT104-NiMh)
- Regulated power supply (Tri-M Engineering – HESC-SER)
- Preamplifier (Cremat – CR-110)
- Linear amplifer circuit (custom built, includes Cremat – CR-200)
- High voltage power supply (Emco – Q15-12)
- Multichannel analyzer (Bridgeport Instruments – eMorpho)
- Thermistor (Measurement Specialties - 100K6D83)
- MCA and temperature software (custom made, written in LabVIEW and C)

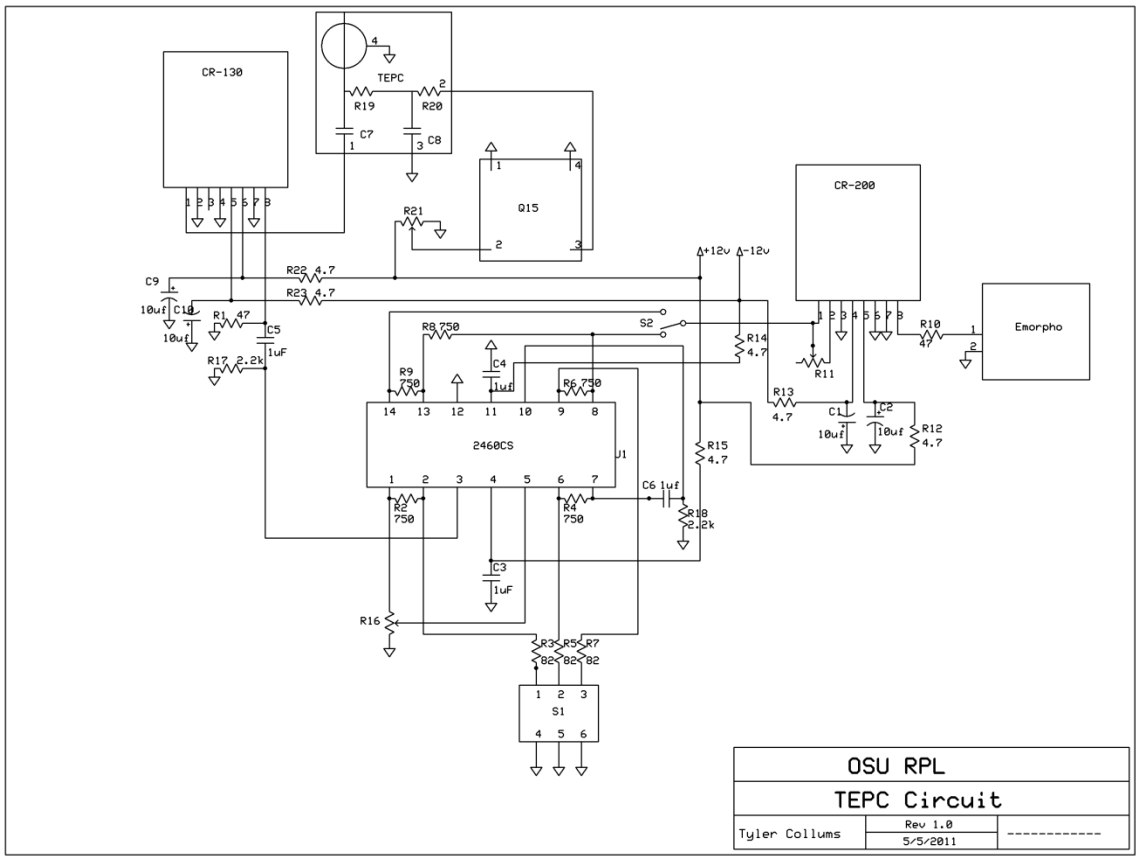


**Figure 73.** The circuit diagram for the flight version TEPC which includes the preamplifier, high voltage power supply, and linear amplifier.

The flight version was designed with the intention of running independently of any other system or power source. The HESC-SER regulated power supply provides +5V to power the onboard computer and +12V to power the preamplifier, linear amplifier circuit, and high voltage power supply. The Cremat CR-110 preamplifier is built into the TEPC canister as was done with the TEPCs used for the plastic comparison study. The signal from the preamplifier is fed into the linear amplifier circuit shown in Figure 73. The linear amplifier circuit was designed and fabricated on printed circuit board in the Radiation Physics Laboratory at OSU. The circuit board printout is shown in Figure 74 that shows the layout of components on the circuit board.

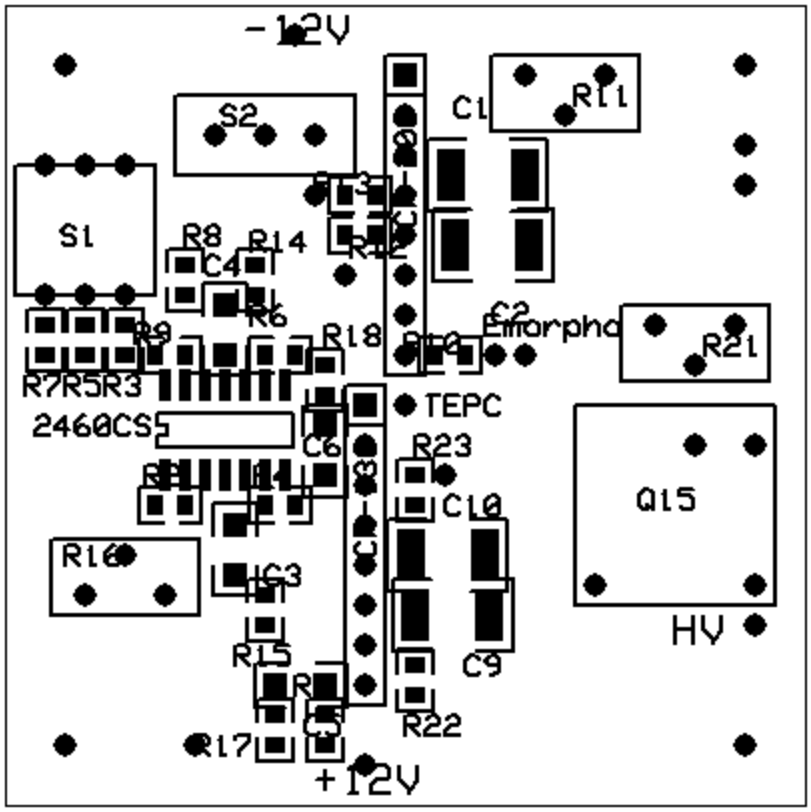


**Figure 74.** The circuit board printout of the TEPC circuit. The actual circuit was fabricated in the Oklahoma State University Radiation Physics Laboratory

The circuit board originally included both the high voltage power supply and the preamplifier. However, it was found that the strong magnetic field created by the high voltage power supply was interfering with the input signal to the preamplier. Both components were later removed from the circuit board to increase the distance between the two components and reduce signal noise. The Emco Q-15 high voltage power supply has an adjustable potentiometer built into the circuit board that allows the high voltage applied to the anode wire to be varied from 0-1500 V. The linear amplifier has an adjustable gain from 10-10,000 and includes the Cremat CR-200 shaping amplifier. In the current version of the flight TEPC the gain must be set before flight. In this case an

appropriate gain must be chosen in order to measure the most relevant lineal energy range. Future versions will incorporate a method for measuring a larger lineal energy range by using different gains in flight. This could be accomplished by switching gain though hardwired circuitry or by simply using two linear amplifiers and two MCAs or a single MCA that programmatically changes input throughout flight.

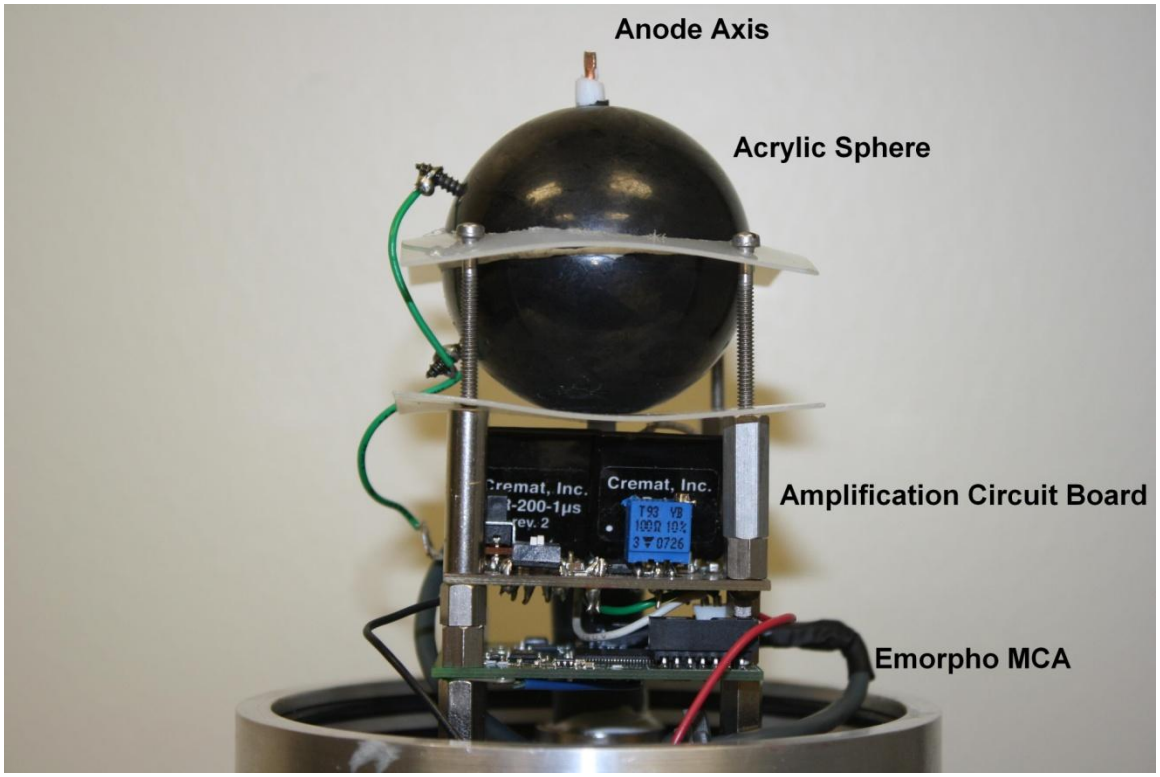


**Figure 75.** A prototype flight version TEPC. The amplifier circuit, high voltage source, and multichannel analyzer were originally contained within the TEPC canister itself. They were later moved into the CPU box.

The signal from output linear amplifier is directly fed into the eMorpho multichannel analyzer. The linear amplifier circuit and MCA were both originally mounted inside the TEPC canister as shown in Figure 75. It was found, however, that the heat generated from the circuit boards caused the temperature of the tissue equivalent gas used in the

detector to rise dramatically in a short period of time. It was decided to remove the components from the gas environment to avoid unnecessary temperature fluctuations in the detector by placing the circuit boards in the CPU box as shown in Figure 76.

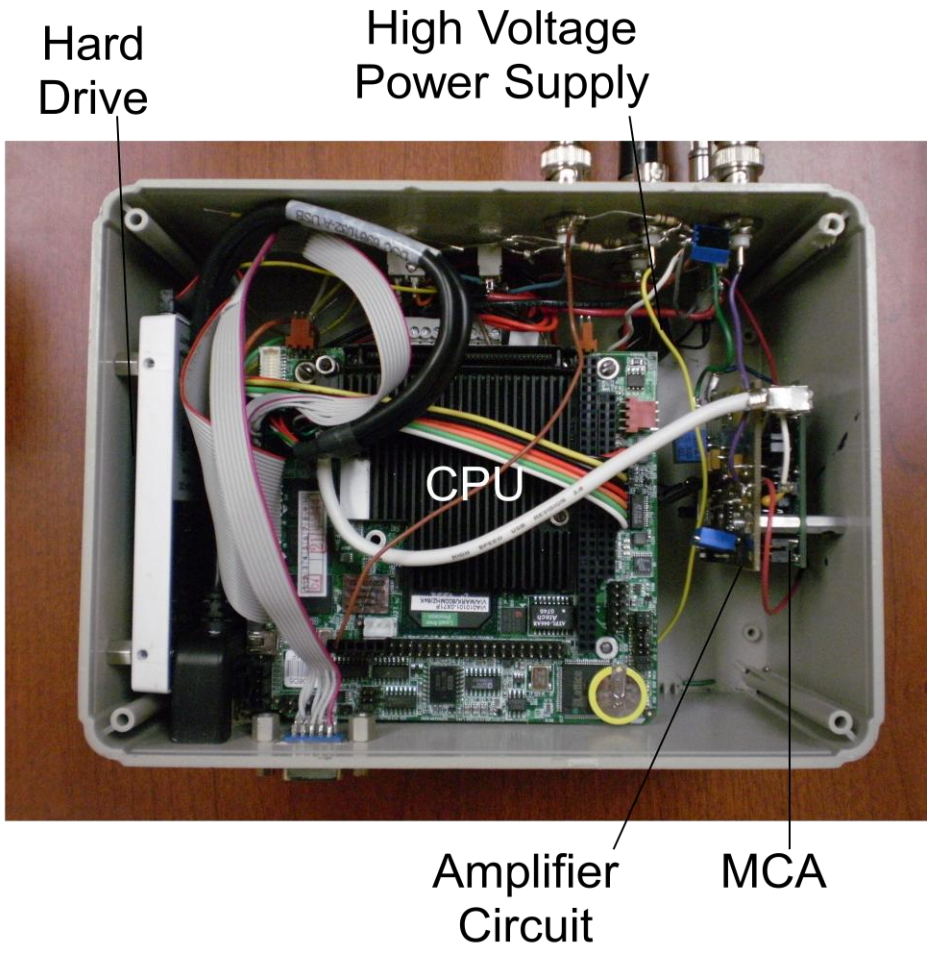


**Figure 76.** The flight box which contains the CPU, hard drive, power supply, battery, linear amplifier, high voltage source, and multichannel analyzer.

The CPU box includes all components of the flight version system except for the preamplifier and ionization chamber which are both located in the TEPC canister. Power and high voltage are ported out of the CPU box and into the TEPC canister through BNC and SHV connectors. The onboard computer communicates with the MCA through USB

using custom software written in LabVIEW. The front panel for the software is shown in Figure 77. The program includes a plot of the current lineal energy spectrum being measured as well a plot of triggered traces from real time measured pulses.

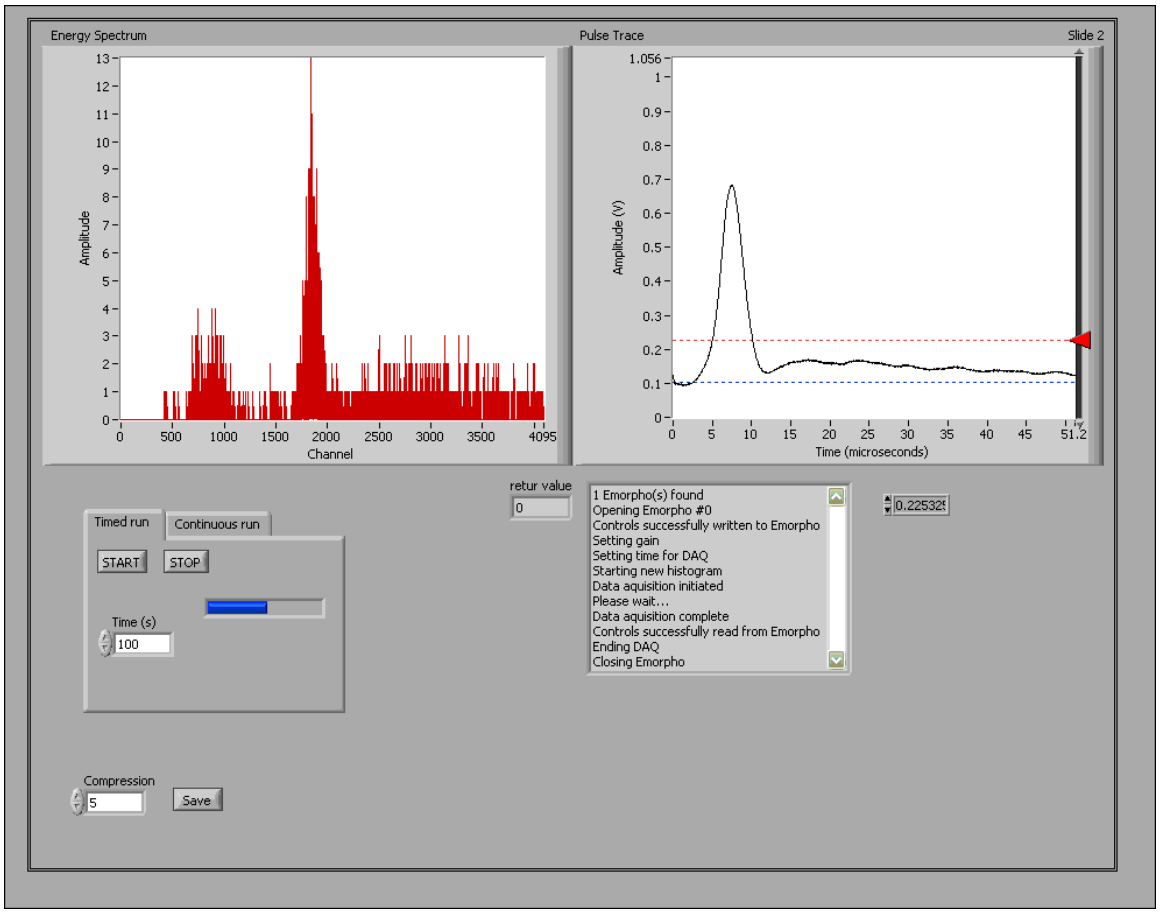


**Figure 77.** The front panel for the TEPC LabVIEW program. The software includes the lineal energy spectrum display as well as a trace display of the measured pulses.

The discriminator level for triggered traces can be adjusted through the software to change the voltage threshold for measured pulses. The software can be configured to perform a timed run and then save the measured spectrum, or the program can run indefinitely and save the current measured spectrum every minute as would be desirable for a balloon flight. The data is stored on the hard drive of the computer. The computer

has a built-in DAQ board from which many input signals may be read. A thermistor is connected to the exterior of the TEPC canister to monitor the temperature of the detector. The voltage drop across the thermistor is monitored on the DAQ board and is saved in a file every second using a custom program written in C.

# CHAPTER IX

# DISCUSSION AND CONCLUSIONS

The experimental results of this study showed slight differences between the responses of the five ionization cavity materials. To better quantify the differences between the plastics, the frequency averaged and dose averaged lineal energies were compared. The average experimental percent differences between the average lineal energies of A-150 and the other four plastics are shown in Table 6.

**Table 6.** Average percent differences between the experimental average lineal energy values of A-150 tissue equivalent plastic verses the other four plastics (%).

| | Experiment | |
|---|---|---|
| | $y_f$ | $y_D$ |
| Nylon | 28.9 | 18.2 |
| Acrylic | 7.0 | 6.6 |
| Polystyrene | 12.9 | 9.9 |
| Polyethylene | 19.0 | 10.8 |

When the four alternative materials are experimentally compared with A-150 tissue equivalent plastic, acrylic is found to be the best match based on the average lineal energies for both protons and heavy ions. The differences in the dose averaged lineal energies are lower than the differences in the frequency averaged lineal for every plastic. This would indicate that there are more differences at the lower lineal energy channels of

the spectra because the dose-averaged lineal energy is less dependent on lower lineal energy events than the frequency-averaged lineal energy is.

The simulated average lineal energies of the five plastics are directly compared to the lineal energies of ICRU muscle. The average percent differences for simulation are shown in Table 7.

**Table 7.** Average percent differences between the simulated average lineal energy values of ICRU muscle verses the five plastics (%).

| | Simulation | |
|---|---|---|
| | $y_f$ | $y_D$ |
| A-150 | 1.3 | 2.6 |
| Nylon | 1.4 | 2.8 |
| Acrylic | 1.4 | 2.8 |
| Polystyrene | 1.3 | 2.6 |
| Polyethylene | 1.1 | 2.4 |

The percent differences for the simulated data are nearly identical for every type of plastic. No one plastic is superior in simulating ICRU muscle given the FLUKA simulated data. This would seem to indicated that the larger differences seen in experiment are most likely not due to the differences in the response of the plastics. It is more likely that the experimental differences seen are present due to differences in the the geometry of the detector that are created in the fabrication process. Each detector follows the same design, but small differences in the position of internal electronics such as the wires, capacitors, and the preamp may create various amount of scatter or secondary particles that could account for the differences seen between the experimental spectra. Differences in the geometry of the detector, specifically the position and angle of the

anode wire, could also affect the ion pair collection efficiency inside the sensitive volume of the detector and change the shape of the measured spectra. In hindsight, it would have been beneficial to fabricate two detectors of the same ionization cavity wall material, so that a comparison between those two detectors could have given a sort of margin of error for the fabrication process.

The differences that were seen in the FLUKA simulated data were primarily found in the proton spectra and not in the heavy ion data. This is most likely because the lineal energy events of the proton beams were much smaller than that of the heavy ion beams. The lower lineal energy events of the primary protons are closer to the lineal energies of secondaries created in the wall of the detector where most of the differences are expected. When measuring the lineal energy spectra of heavy ion beams, the dose contribution of secondaries is less significant when compared to the primaries due to the high LET of the primary beam.

The average lineal energies for experiment and simulation increase almost linearly with the LET of the primary beam as shown in Figures 69 and 71 and follow the trend of the theoretical average lineal energies which are directly proportional to LET and assume the gas has no wall. This is because the primary peaks of the lineal energy spectra are almost exclusively caused by primaries depositing energy directly into the gas of the detector and not from secondaries generated in the wall (Gersey et al., 2002). For this reason, the ionization wall materials have very little effect on the lineal energy spectra or the measurement of dosimetric quantities for charged particle radiation.

It is the conclusion of this study that any of the four alternate plastics used in these experiments could be used as an acceptable substitute for human tissue in a gas filled detector for the measurement of ionizing charged particle radiation. To further investigate the radiation response of the alternative materials used in this study, it would be useful to test and compare these materials with A-150 tissue equivalent plastic in energetic neutron fields. However, due the similarities between the neutron cross sections of the five plastics as well the similarity to ICRU muscle caused primarily by the hydrogen content of the materials, no significant difference in neutron response should be expected.

# REFERENCES


Amptek ADMCA Display and Acquisition Software. Mar. 2012. <http://www.amptek.com/admca.html>.

Benjamin, P., C. Kemshall, and J. Redfearn. "A high resolution spherical proportional counter." Nuclear Instruments and Methods 59 (1968): 77-85.

Borak, T. B., T. Doke, T. Fuse, S. Guetersloh, L. Heilbronn, K. Hara, M. Moyers, S. Suzuki, P. Taddei, K. Terasawa, and C. J. Zeitlin. "Comparisons of LET Distributions for Protons with Energies between 50 and 200 MeV Determined Using a Spherical Tissue-Equivalent Proportional Counter (TEPC) and a Position-Sensitive Silicon Spectrometer (RRMD-III)." Radiation Research 162 (2004): 687-92.

Braby, L. A., and G. D. Badhwar. "Proportional counter as neutron detector." Radiation Measurements 33 (2001): 265-67.

Braby, L. A., G. W. Johnson, and J. Barthe. "Practical Consideration in the Design and Construction of Tissue-Equivalent Proportional Counters." Radiation Protection Dosimetry 61 (1995): 351-79.

De Nardo, L. "Mini-TEPCs for radiation therapy." Radiation Protection Dosimetry 108 (2004): 345-52.

Dietze, G., H. G. Menzel, and G. Buhler. "Calibration of Tissue-Equivalent Proportional Counters used as Radiation Protection Dosemeters." Radiation Protection Dosimetry 9 (1984): 245-49.

Fasso, A., A. Ferrari, and S. Roesler. FLUKA code: Present applications and future developments. Proc. of Conference for Computing in High-Energy and Nuclear Physics, La Jolla, CA.

Fasso, A., A. Ferrari, S. Roesler, P. R. Sala, Battistoni G, F. Cerutti, E. Gadioli, M. V. Garzelli, F. Ballarini, A. Ottolenghi, A. Empl, and J. Ranft. The physics models of FLUKA: Status and recent developments. Proc. of Conference for Computing in High Energy and Nuclear Physics, La Jolla, CA.

Gerdung, S., P. Pihet, J. E. Grindborg, H. Roos, U. J. Schrewe, and H. Schuhmacher. "Operation and Applications of Tissue-Equivalent Proportional Counters." Radiation Protection Dosimetry 61 (1995): 381-404.

Gersey, B. B., T. B. Borak, S. B. Guetersloh, C. Zeitlin, J. Miller, L. Heilbronn, T. Murakami, and Y. Iwata. "The Response of a Spherical Tissue-Equivalent Proportional Counter to Iron Particles from 200–1000 MeV/nucleon." Radiation Research 157 (2002): 350-60.

Goodhead, Dudley T., Peter O'Neill, and Hans G. Menzel. Microdosimetry: An interdisciplinary approach. Cambridge: Royal Society of Chemistry, 1997.

ICRU. "Microdosimetry." Report of the International Commision on Radiation Units and Measurements 36 (1983).

ICRU. Report of the International Commission on Radiological Units and Measurements NBS 62 (1956).

ICRU. "Physical Aspects of Irradiation." Recommendations of the International Commision on Radiological Units and Measurements (ICRU) Report 10b (1962).

Kliauga, P., T. Schmitz, A. J. Waker, and H. (eds. ). Zoetelief. Design, construction and use of tissue equivalent proportionalcounters. EURADOS report. 1995.

Knoll, Glenn F. Radiation detection and measurement. New York: Wiley, 1979.

Korff, S. A. "The Operation of Proportional Counters." Reviews of Modern Physics 14 (1942): 1-11.

Korff, S. A. "The Operation of Proportional Counters." Reviews of Modern Physics 14 (1942): 1-11.

Kyllonen, J. E., L. Lindborg, and G. Samuelson. "Cosmic Radiation Measurements On-board Aircraft with the Variance Method." Radiation Protection Dosimetry 93 (2001): 197-205.

NIST. Stopping-Power and Range Tables for Electrons, Protons, and Helium Ions. <http://www.nist.gov/pml/data/star/index.cfm>.

NIST. XCOM: Photon cross sections database. <http://www.nist.gov/pml/data/xcom/index.cfm>.

NNDC. "Evaluated nuclear data file (ENDF)." Evaluated nuclear data file (ENDF). <http://www.nndc.bnl.gov/exfor/endf00.jsp>.

Rollet, S., P. Beck, A. Ferrari, M. Pelliccioni, and M. Autischer. "Dosimetric considerations on TEPC fluka-simulation and measurements." Radiation Protection Dosimetry 110 (2004): 833-37.

Rollet, S., P. Colautti, B. Grosswendt, J. Herault, E. Gargioni, P. Beck, M. Latocha, and D. Moro. "Microdosimetric Assessment of the Radiation Quality of a Therapeutic Proton Beam: Comparison between Numerical Simulations and Experimental Measurements." Radiation Protection Dosimetry 143 (2010): 445-49.

Rossi, H. H., and G. Failla. "Tissue-Equivalent Ionization Chambers." Nucleonics 14 (1956): 32-37.

Rossi, H. H., and M. Zaider. Microdosimetry and its applications. Berlin: Springer, 1996.

Rossi, Harald H. "Microscopic Energy Distribution in Irradiated Matter." Radiation Dosimetry. 2nd ed. Vol. 1. New York: Academic P, 1968. 43-92.

Schrewe, U. J., H. J. Brede, P. Pihet, and H. G. Menzel. "On the Calibration of Tissue-Equivalent Proportional Counters with Built-In α Particle Sources." Radiation Protection Dosimetry 23 (1988): 249-52.

Shinn, J. L., G. D. Badhwar, M. A. Xapsos, F. A. Cucinotta, and J. W. Wilson. "An Analysis of Energy Deposition in a Tissue Equivalent Proportional Counter Onboard the Space Shuttle." Radiation Measurements 00 (1998): 1-9.

Shonka, Francis R., John E. Rose, and G. Failla. "Conduction Plastic Equivalent to Tissue, Air and Polystyrene." Second United Nations International Conference on Peaceful Uses of Atomic Energy 21 (1958): 184-87.

Smathers, James B., Victor A. Otte, Alfred R. Smith, Peter R. Almond, Frank H. Attix, John J. Spokas, William M. Quam, and Leon J. Goodman. "Composition of A-150 tissue-equivalent plastic." Medical Physics 4 (1977): 74-77.

Varma, Matesh N. "Calibration of Proportional Counters in Microdosimetry." Proceedings of the Eighth Symposium on Microdosimetry (1982).

Zheng, Yuanshui, Eric Ramirez, Anthony Mascia, Xiaoning Ding, Benny Okoth, Omar Zeidan, Wen Hsi, Ben Harris, Andries N. Schreuder, and Sameer Keole. "Commissioning of output factors for uniform scanning proton beams." Medical Physics 38 (2011).

VITA

Tyler Lance Collums

Candidate for the Degree of

Doctor of Philosophy

Thesis: COMPARISON OF PLASTICS USED IN TISSUE EQUIVALENT PROPORTIONAL COUNTERS (TEPC) AND DEVELOPMENT OF A BALLOON BORNE TEPC

Major Field: Physics

Biographical:

Education:

Completed the requirements for the Doctor of Philosophy in physics at Oklahoma State University, Stillwater, Oklahoma in December, 2012.

Completed the requirements for the Master of Science in physics at Pittsburg State University, Pittsburg, Kansas in 2008.

Completed the requirements for the Bachelor of Science in physics at Pittsburg State University, Pittsburg, Kansas in 2006.